ABSTRACT

Title of Dissertation:	IMPROVING FORECASTS OF VOLCANIC CLOUDS: AN ANALYSIS OF OBSERVATIONS AND EMISSION SOURCE TERM METHODS
	Eric Joseph Hughes Doctor of Philosophy 2018
Dissertation directed by:	Professor Russell R. Dickerson Dr. Nickolay A. Krotkov Department of Atmospheric and Oceanic Science

Volcanic eruptions can occur with little or no warning and explosively inject dense ash and sulfur dioxide (SO_2) clouds high into the atmosphere. I investigated different types of observations and analysis methods used to monitor and quantify volcanic ash and SO_2 clouds. I begin with an analysis of the 2010 eruption of Eyjafjallajökull, employing ash cloud transport modeling capabilities I developed for the Goddard Earth Observing System, Version 5 (GEOS-5). The emission source terms describing the initial state of the Eyjafjallajökull ash clouds were estimated using radar observations of the ash cloud's initial injection altitude. Results of the initial simulations agreed with operational ash forecasts from the time of the eruption and with many other published studies, but showed notable disagreement with

satellite observations. The emission source term was estimated using an alternative approach, yielding simulations that better matched satellite observations. I used the result to highlight limitations of radar observations not accounted for in previous studies of the Eyjafjallajökull ash clouds.

UV satellite observations are often used to monitor and quantify volcanic clouds of ash and SO_2. I tested the limitations of the OMPS SO_2 satellite observations using an Observing System Simulation Experiment (OSSE). The framework used GEOS-5 simulations of the atmospheric composition in the wake of a Pinatubo-like volcanic eruption to generate synthetic top-of-the-atmosphere (TOA) radiances. The TOA radiances served as input to the OMPS SO_2 retrieval. In comparing the OMPS retrieval SO_2 to the original GEOS-5 SO_2, I found that the sulfate aerosols and ash can cause the OMPS SO_2 retrieval to underestimate the total SO_2 burden. These effects were amplified at increased satellite viewing angles.

I finish my analysis by looking at observations from the satellite-based Cloud-Aerosol Transport System (CATS), where I show that even under the time constraints of an operational forecast, the available CATS observations were able to improve forecasts of volcanic SO_2 clouds.

IMPROVING FORECASTS OF VOLCANIC CLOUDS: AN ANALYSIS OF OBSERVATIONS AND EMISSION SOURCE TERM METHODS

by

Eric Joseph Hughes

Dissertation submitted to the Faculty of the Graduate School of the
University of Maryland, College Park, in partial fulfillment
of the requirements for the degree of
Doctor of Philosophy
2018

Advisory Committee:
Professor Russell R. Dickerson, Chair/Advisor
Dr. Nickolay A. Krotkov, Advisor
Dr. Peter R. Colarco
Professor Zhanqing Li
Professor Paul M. Schonfeld

Dedication

To my fiancé, my family and my friends for their infinite patience and support.

Acknowledgements

I would like to gratefully acknowledge my research advisor Dr. Nickolay Krotkov for his guidance and patience. Dr. Krotkov showed me the importance of cooperation in research and science, a lesson I'll keep with me wherever I may find my future self. I thank my academic advisor Dr. Russell Dickerson for guiding me through my studies at UMD. He offered ample advice that helped me forge the path to completing my dissertation.

Much of the research presented in this dissertation would not have been possible without many of the researchers at NASA. I'm particularly grateful to Dr. Arlindo Da Silva and Dr. Peter Colarco for giving me countless hours of guidance to help me understand the models and analysis used throughout this work. They both frequently offered up their time as a kindness to help me further my research. I would also like to thank Brad Fisher and Dr. Can Li, whose advice and guidance helped me better understand the OMPS retrieval.

I'd like to thank the members of my dissertation committee who have not yet been acknowledged, Dr. Zhanqing Li And Dr. Paul Schonfeld, for offering their time to serve on my committee.

I owe a lot of my success to the family and friends that have supported me through the many years of my academic studies. I thank my mom, who worked harder then anyone I have ever known so that I could have the opportunity to go to college and achieve academic success, and my sister Jill for her constant support and advice. They both inspire me every day. To my fiancé, Jaime, I owe the greatest

thanks. His continued patience and support gave me the strength to accomplish more than I ever thought possible.

Table of Contents

List of Tables

List of Figures

Chapter 1: Introduction

1.1 Background

With little or no warning, volcanoes can explosively erupt towering plumes of ash and sulfur dioxide (SO_2) high into the atmosphere. Walls of hot ash, rocks, and lava cause destruction near volcanic eruptions, but erupted volcanic plumes can be entrained into upper atmospheric winds and transported long distances. As a result, volcanic eruptions are not merely a regional danger, but a global hazard.

Volcanic ash clouds pose an immediate threat to aviation. One of the first major aviation incidents involving volcanic ash occurred over Indonesia in 1982. While en route in Auckland, New Zealand, British Airways Flight 9, a 747 aircraft, experienced a sudden surging and flame out its jet engines, and within minutes all four engines had failed [*Job, 1994*]. The captain and crew had unknowingly flown directly into a volcanic ash cloud that erupted from Mount Galunggung. Volcanic ash built up in the jet engines, causing extinction of the flame in the engine's combustion chamber [*BBC, 2010*]. The 747 glided for 12 minutes, descending nearly 7 km, before one of the engines was successfully restarted [*Job, 1994*]. Fortunately, while the airplane was descending, volcanic ash embedded in the engines re-solidified and chipped away, allowing the airflow needed to restart the engines [*BBC, 2010*]. Shortly after, the remaining engines could also be restarted allowing for an emergency landing at the Jakarta Airport [*Job, 1994*]. Years later, in 1989, an ash cloud from Alaska's Mount Redoubt volcano would cause a remarkably similar incident to occur with KML Flight 867.

Both the 1982 and 1989 airplane ash incidents highlight the dangers that volcanic ash poses on aviation safety. When ash is entrained into jet engines, the internal engine heat can cause the ash to melt and re-solidify and block airflow. In particular, deposition of molten volcanic ash on the high-pressure turbine nozzle guide vanes alters internal pressures that can lead to a disruption of air flow to the compressor, or surging, and extinction of the flame in the compression chamber, flameout [*Dunn and Wade, 1994*]. Beyond engine damage, volcanic ash has the effect of sandblasting forward facing parts of the plane, reducing visibility in the cockpit windshield, and causes widespread damage to the airplanes sensors [*Campbell, 1994; Casadevall et al., 1996*].

The roles of detecting, tracking and forecasting volcanic ash clouds are the responsibility of the international collection of Volcanic Ash Advisory Centers (VAACs). By 1997, the International Civil Aviation Organization (ICAO) had established nine VAACs, designating geographic areas of responsibility for each VAAC, collectively providing near-global coverage. The current VAAC "area of responsibility" map is shown in Figure 1.1. The VAACs produce Volcanic Ash Advisories (VAAs) that note details about volcanic eruptions and make estimates of the extent of volcanic ash in the atmosphere. A sample VAA is shown in Figure 1.2. VAAs provide estimates of air mass regions contaminated by volcanic ash at present, and show regions where ash contamination is forecasted, at 6-hour intervals for up to 24 hours.

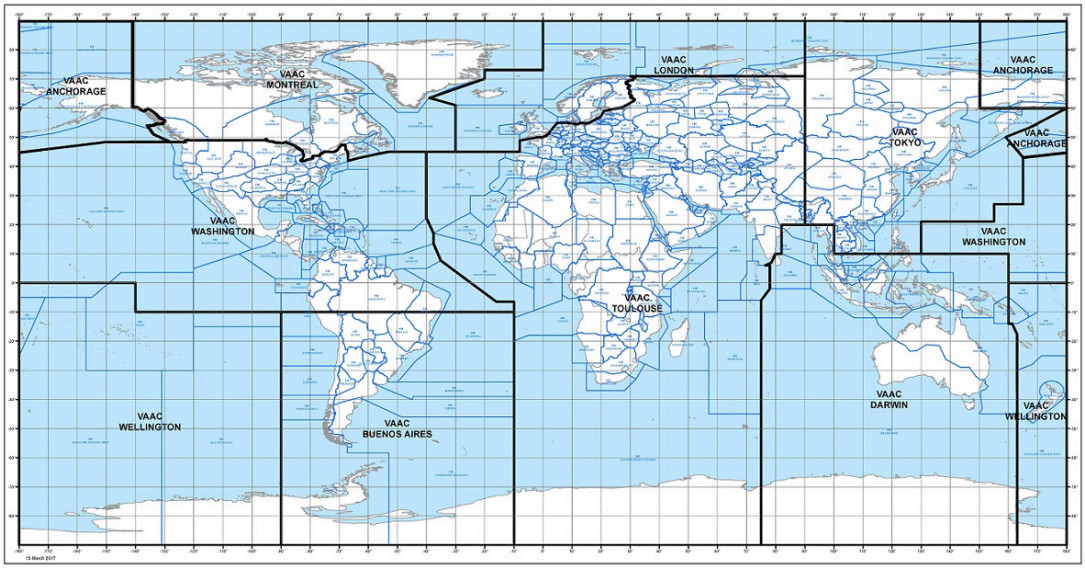

Figure 1.1 The current Volcanic Ash Advisory Centers areas of responsibility. The black outlines contour the 9 VAAC areas: Anchorage, Montreal, London, Tokyo, Toulouse, Washington, Darwin, Wellington and Buenos Aires. The smaller blue contours outline flight information regions (FIRs).

From 1953 to 2009, there were a total 94 confirmed incidents of airplanes flying through ash clouds [*Guffanti et al. 2010*]. Of the 94 incidents, 74 were classified as having, at minimum, airframe and/or engine damage, with 9 incidents reporting engine failure [*Guffanti et al. 2010*]. Fortunately, all of these documented incidents were resolved safely, without any airplane crashes.

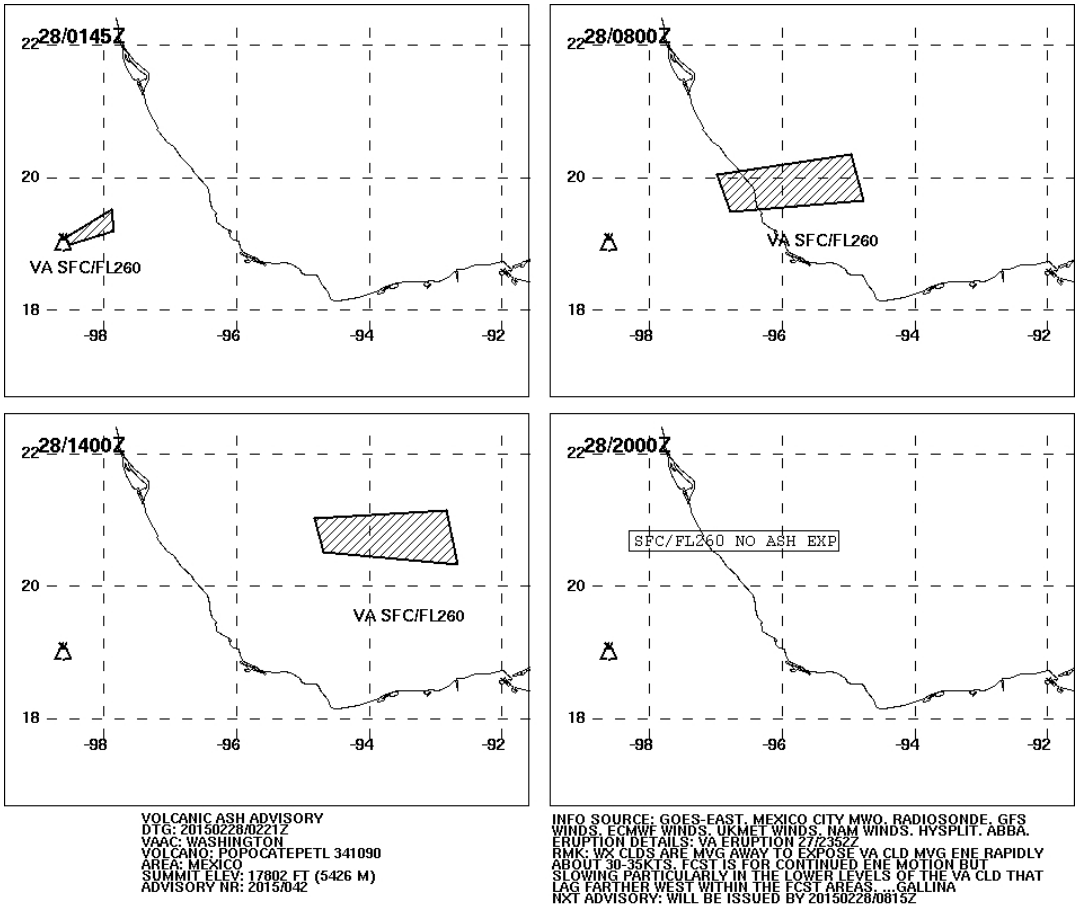

Figure 1.2 VAAC Volcanic Ash Advisory (VAA) for Mexico's Popocatepetl Volcano. The top left panel represents the current estimate of ash-contaminated air. Forecasts for 08:00Z, 14:00Z, and 20:00Z are shown in the upper right, lower left and lower right panels, respectively. The text below the panels details notes on the volcanic eruption and data used to construct the VAA.

On April 14th 2010, the Icelandic volcano Eyjafjallajökull began a nearly month-long eruption that intermittently erupted ash clouds that spread across Europe. The Eyjafjallajökull ash clouds led to prolonged flight cancellations and widespread disruptions to the airline industry's economy and personal travel. The ash clouds Eyjafjallajökull spewed into the atmosphere halted flights across Europe and left travelers stranded worldwide. Within just the first week of the eruption the aviation travel industry suffered an estimated $1.7 billion in revenue loss [*IATA, 2010*] as

airports scrambled to reroute planes around the ash clouds. A total of 108,000 flights were cancelled during the first week of the eruption [*Alexander, 2013*]. The mass flight cancellations received strong criticism from the public and airline companies over the no-fly ash avoidance standard used by the VAAC [*EU Business, 2010*]. By May 10th, the ICAO had revised the ash avoidance policy towards an ash tolerance policy based on regions of "low", "medium" and "high" ash contamination [*ICAO, 2010*. The ash tolerances were defined as regions with volcanic ash air mass concentrations of: < 2 mg (low), > 2 mg < 4 mg (medium), and > 4 mg (high) and allowed different flight restrictions depending on the hazard level [*Prata and Rose, 2015*]. The FAA still operates under the ash avoidance guideline.

Volcanically erupted ash clouds typically settle out of the atmosphere within several days, however the injection of volcanic SO_2 into the upper troposphere and lower stratosphere (UTLS) leads to the oxidation of SO_2 to sulfate aerosols. Sulfate aerosols persist in the stratosphere for months to years, producing a net global surface cooling effect and altering atmospheric circulations [*Robock, 2000; Aquila et al. 2012*]. However, the magnitude of global surface cooling due to large volcanic eruptions is in question [*Canty, et al. 2013*]. Quantifying the influence of volcanic sulfate aerosol clouds on global climate requires an understanding of both the total amount of SO_2 emitted and the altitude of injection. Inaccurate estimates of either of these parameters can lead to under or over estimation of the effects of volcanic eruptions on climate.

In order to produce accurate simulations and forecasts of volcanic ash and SO_2, accurate models are needed. Perhaps most important to the forecasts are the initial

conditions, or source terms, used to initialize the volcanic clouds within the transport model. Volcanic ash and SO_2 source terms can vary depending on the type of model used, but generally include: volcanic ash/SO_2 mass flux, eruption duration, ash/SO_2 plume maximum altitude, and ash/SO_2 plume thickness. Source terms are rarely observed directly, and frequently estimated based on indirect observations. Changing Europe's aviation guidance from ash avoidance to ash tolerance requires the VAAC to produce more quantitative ash forecasts. Similarly, better source terms would better quantify the role of volcanic eruption of SO_2 in climate. These needs place greater demand on the scientific community to build more accurate volcanic ash and SO_2 models, develop more accurate and robust observational capabilities, and better fuse observations with models.

1.2 Outline of Research

For both aviation and climate concerns, modeling the SO_2 and ash clouds from explosive volcanic eruptions requires knowledge of the emission source terms. Inaccuracies in any of these parameters can result in simulations that drastically deviate from observations. This dissertation focuses on the simulation of volcanic ash and SO_2 clouds, with emphasis on steps needed to construct accurate simulations. This works will address the following questions:

1. How well can we forecast the transport of volcanic ash and SO_2 clouds?
2. What are the biases and limitations of volcanic cloud observations? What assumptions are being made?
3. How do we relate observations of volcanic clouds to transport models?

This research begins by modeling a volcanic eruption that is perhaps the most consequential in recent history, the 2010 eruption of Eyjafjallajökull. The Eyjafjallajökull eruption has been thoroughly described by a wide number of modeling and observational studies, and was initially chosen to serve as a test-bed for our ash modeling development. After an initial analysis this eruption, I found that different observations seemed to tell conflicting stories. A more critical analysis of the observations revealed the specific assumptions responsible for producing errors in both our ash simulations and simulations published in numerous other studies. The methods and results of this study are presented in Chapter 3.

The next chapter focuses more directly on the uncertainty and limitations of the volcanic cloud observations and source term analysis. Using the framework of an Observing System Simulation Experiment (OSSE), chemical transport and radiative transfer models are used simulate a fictional volcanic eruption and then construct synthetic inputs to satellite retrievals. By controlling the inputs to the satellite retrieval, I quantify how the retrieval responds to aerosols in the volcanic plume. The synthetic satellite observations are also used to estimate the volcanic eruption source terms, which I compare to the actual source terms used to construct the model simulations.

In the final analysis chapter, focus shifts towards newer satellite instruments that can provide direct observations of the altitude and thickness of volcanic clouds of ash and sulfate aerosols. The volcanic cloud aerosol profiles are compared to model simulations, and I demonstrate how information from these instruments can

greatly improve forecasts of volcanic clouds. I explore the operational capacity of these instruments, with an eye toward the importance of the observation timing and production latency when used to construct near-realtime forecasts. The results of this study are published in Hughes et al. [2016].

References, Chapter 1

Alexander, D. (2013), Volcanic ash in the atmosphere and risks for civil aviation: a study in European crisis management, International Journal of Disaster Risk Science, 4(1), 9-19.

Aquila, V., L. D. Oman, R. S. Stolarski, P. R. Colarco, and P. A. Newman (2012), Dispersion of the volcanic sulfate cloud from a Mount Pinatubo–like eruption, Journal of Geophysical Research: Atmospheres, 117(D6).

BBC (2010), When volcanic ash stopped a Jumbo at 37,000ft. http://news.bbc.co.uk/2/hi/uk_news/magazine/8622099.stm Accessed on May 16, 2018

EU Business (2010), EU disagrees with airlines' criticism over airspace closure. < *https://www.eubusiness.com/news-eu/iceland-volcano.478* > Accessed on May 16, 2018

Campbell, E. E. (1994), Recommended flight-crew procedures if volcanic ash is encountered, paper presented at Volcanic Ash and Aviation Safety: Proceedings on the First International Symposium of Volcanic Ash and Aviation Safety, US Geological Survey Bull.

Canty, T., N. Mascioli, M. Smarte, and R. Salawitch (2013), An empirical model of global climate-Part 1: A critical evaluation of volcanic cooling, Atmospheric Chemistry and Physics, 13(8), 3997.

Casadevall, T. J., P. Delos Reyes, and D. J. Schneider (1996), The 1991 Pinatubo eruptions and their effects on aircraft operations, Fire and Mud: eruptions and lahars of Mount Pinatubo, Philippines, 625-636.

Dunn, M. G., and D. P. Wade (1994), Influence of volcanic ash clouds on gas turbine engines, US Geological Survey Bulletin, 2047, 107-118.

Guffanti, M., T. J. Casadevall, and K. E. Budding (2010), Encounters of aircraft with volcanic ash clouds: a compilation of known incidents, 1953-2009, US Department of Interior, US Geological Survey.

Hughes, E. J., J. Yorks, N. A. Krotkov, A. M. Silva, and M. McGill. "Using CATS near-real-time lidar observations to monitor and constrain volcanic sulfur dioxide (SO_2) forecasts." Geophysical Research Letters 43, no. 20 (2016).

IATA (2010), IATA Economics Briefing: The Impact of Eyjafjallajokull's Volcanic Ash Plume, edited, International Air Transport Association.
< *http://www.iata.org/whatwedo/Documents/economics/Volcanic- Ash-Plume-May2010.pdf* >

ICAO (2010), Volcanic Ash Contingency Plan, European and North Atlantic Regions. EUR Doc. 019, NAT Doc. 006, Part II edited, International Civil Aviation Organization Paris, France.

Job, Macarthur. Air disaster. Vol. 2. Kogan Page Publishers, 1996.

Prata, F., and B. Rose (2015), Volcanic ash hazards to aviation, in The Encyclopedia of Volcanoes (Second Edition), edited, pp. 911-934, Elsevier.

Robock, A. (2000), Volcanic eruptions and climate, Reviews of Geophysics, 38(2), 191-219.

Chapter 2: Volcanic Plumes and Clouds: Observations, Models and Analysis

This chapter serves to establish the scope of my investigation of volcanic eruptions. The chapter begins with a description of volcanic plumes and clouds in general, to establish exactly what is being studied and note importation definitions. This is followed by a description of the models used to simulate and forecast the transport of volcanic ash and SO_2 clouds. Next, the various satellite instruments and data products that help monitor ash and SO_2 clouds are presented. The chapter ends with a summary of analysis methods that jointly use both observations and models to produce more accurate simulations of volcanic ash and SO_2 clouds.

This chapter does not cover all instruments and models used in this dissertation, but presents a basic overview of the models and instruments that occur frequently throughout this work. Other instruments and models less prominently used are presented within each accompanying case study.

2.1 Volcanic Plumes and Volcanic Clouds

The structure of a volcanic plume is driven by the dynamics of the volcano and the ambient atmosphere. A volcanic plume from the 2015 eruption of Calbuco is shown in Figure 2.1, where the explosive eruption propelled the plume upwards of 20 km into the atmosphere.

Figure 2.1 A volcanic plume from the 2015 eruption of the Chilean volcano, Calbuco. The photograph was taken on April 22nd 2015 from Puerto Varas, Chile. Photo taken by Wikimedia Commons user Aeveraal, republished here under a Creative Commons license.

Explosive pressures from volcanic eruptions are the initial driving force of volcanic plumes, composed of a mixture of rocks, ash and gases. As these plumes are expelled into the atmosphere, ambient air is entrained into the plume with the effect of reducing its density. If the plume remains denser then air (although hot, it may contain high concentrations of relatively dense CO_2), it will collapse, falling back down to the Earth's surface and flowing radially away from the volcano [*Sparks, 1986*]. This scenario results in the rapid spread of pyroclastic flows, highly destructive walls of hot ash that travel along terrain and away from the volcano. Alternatively, the hot volcanic plume may entrain enough ambient air to make it less

dense then the surrounding atmosphere, where buoyant forces then propel the plume high into the atmosphere. The plume ascends until reaching the level of neutral buoyancy, where the plume's density equals that of surrounding air, though momentum can cause the part of the plume to overshoot this level. The plume will begin to spread radially at the neutral buoyancy level, forming an umbrella cloud.

The composition of a volcanic plume varies from volcano to volcano, but generally consists of tephra, aerosols, and various gases. Tephra is an umbrella term, used to describe all fragmented material ejected from volcanic eruptions, consisting of everything from boulders to dust-like aerosols. Tephra particles smaller than 2 mm are classified as volcanic ash. The composition of volcanic ash varies across different eruptions, but is typically composed of: pumice fragments, volcanic glass shards, crystals, mineral, and/or other rock fragments, with densities that range from 700-3,200 kg/m^3 [*Shipley and Sarna-Wojcicki, 1982*]. Sulfur dioxide, SO_2, is considered the most important gas from volcanic eruptions due to its climate impacts [*Robock, 2000*]. Although greater masses of H_2O(v), N_2, and CO_2 are present in a volcanic plume, the ratio of emitted volume with respect to the atmospheric background is greatest for SO_2 [*Robock, 2000*].

After the initial eruption and subsequent lofting into the atmosphere, volcanic plumes become entrained into the atmosphere's general circulation by upper level winds. When no longer attached to the volcano, *volcanic plumes* are referred to as *volcanic clouds*. Volcanic clouds typically consist of SO_2, sulfate aerosols, and fine ash, as coarser ash is quickly removed via gravitational settling. Typically, fine ash is considered ash particles with a diameter less than 62 μm [*Prata and Tupper,*

2009]. While modeling coarse ash is important when trying to estimate regional ash fallout around a volcano, the focus in this work is primarily on ash clouds that have the potential to be transported far (> 1,000 km) away from their volcanic source.

As noted previously, volcanic ash typically settles out of volcanic clouds within days to weeks [*Niemeier et al. 2009*]. The primarily pathway for the removal of volcanic SO_2 is through oxidation to sulfate aerosols, with a typical lifetime of about 3 days in the troposphere [*Stevenson et al. 2003*]. Volcanic SO_2 is oxidized to sulfate aerosols through either in-air reaction with hydroxyl radicals (*E 1.1*) or in-cloud reaction with (*E 1.2*) with hydrogen peroxide. Dry deposition of SO_2 to the earth's surface is another removal mechanism that typically accounts for nearly half of SO_2 removal from the atmosphere [*Chin et al. 2000*]. However, volcanoes typically inject SO_2 into much higher altitudes than anthropogenic SO_2 sources, making SO_2 removal through oxidation to sulfate aerosols more likely [*Stevenson et al. 2003*]. The lifetime of sulfate aerosols ultimately depends on their placement in the atmosphere. In the troposphere, sulfate aerosols from volcanic clouds are removed by wet and dry deposition, lending them to a relatively short lifetime (days to weeks) [*Robock, 2000*]. In the stratosphere, the relative stability and dryness of the air limit sulfate aerosol removal to slower sedimentation and downward transport. Volcanic eruptions that inject volcanic gases into the stratosphere produce sulfate aerosols with lifetimes on the order of months to years [*Robock, 2000*].

$$SO_2 + OH(g)\ (+ O_2 + H_2O) = H_2SO_4 + HO_2 \qquad \text{(E 2.1)}$$

$$SO_2 + H_2O_2(aq) = H_2SO_4 \qquad \text{(E 2.2)}$$

The long-term fate of sulfate aerosols and their impact on the climate is acknowledged as an area of study that could benefit from the work presented here, but is not directly considered in this dissertation. In this body of work, my primary focus is directed at modeling and observing volcanic clouds composed of ash, sulfate aerosols and SO_2 on time scales of days to weeks following an eruption.

2.2 Volcanic Plumes and Volcanic Clouds: Modeling

How we choose to model volcanic plumes and clouds ultimately depends on the goal of the experiment. Fluid dynamics models have been developed to simulate the complex 3-D structure of volcanic plumes to better understand the effects of ambient air entrainment on volcanic plume structures [e.g. *Suzuki et al. 2005*]. These models yield detailed simulations of the vertical structure of volcanic plumes, and the umbrella clouds that they form. Earlier studies developed simpler 1-D models of volcanic plumes [*Bursik 2001*], to study the role atmospheric winds on the rise of volcanic plumes and their vertical distribution. When modeling volcanic clouds and their downwind transport, detailed volcanic plume models are often replaced by assumptions of the plume's initial vertical distribution, as done in Folch et al. [*2011*], Matthias et al. [2011], Aquila et al. [2012], Webley et al. [*2012*] and Webster et al. [*2012*]. In this work, I follow the convention of either assuming an initial vertical distribution of volcanic ash and SO_2 or estimating it from observations, as done in Hughes et al. [*2012*].

Numerous dispersion and chemical transport models have been developed to simulate the dispersion of volcanic clouds, using Lagrangian, Eulerian, or Hybrid

model frameworks. A report by Bonadonna et al. [*2012*] presents a full list of the various ash dispersion models currently in use, highlighting the variety of models and model types available. For example, the Washington D.C. VAAC primarily uses the Hybrid model HYSPLIT, while the Anchorage and London VAACs use the Lagrangian models PUFF and NAMES, respectively. This work uses NASA's state of the art global Goddard Earth Observing System, version 5 (GEOS-5) [*Suarez et al., 2008*] Eulerian Earth System model, which includes atmospheric circulation and composition, as well as land and ocean characterization. The structure of the GEOS-5 model is shown in Figure 2..

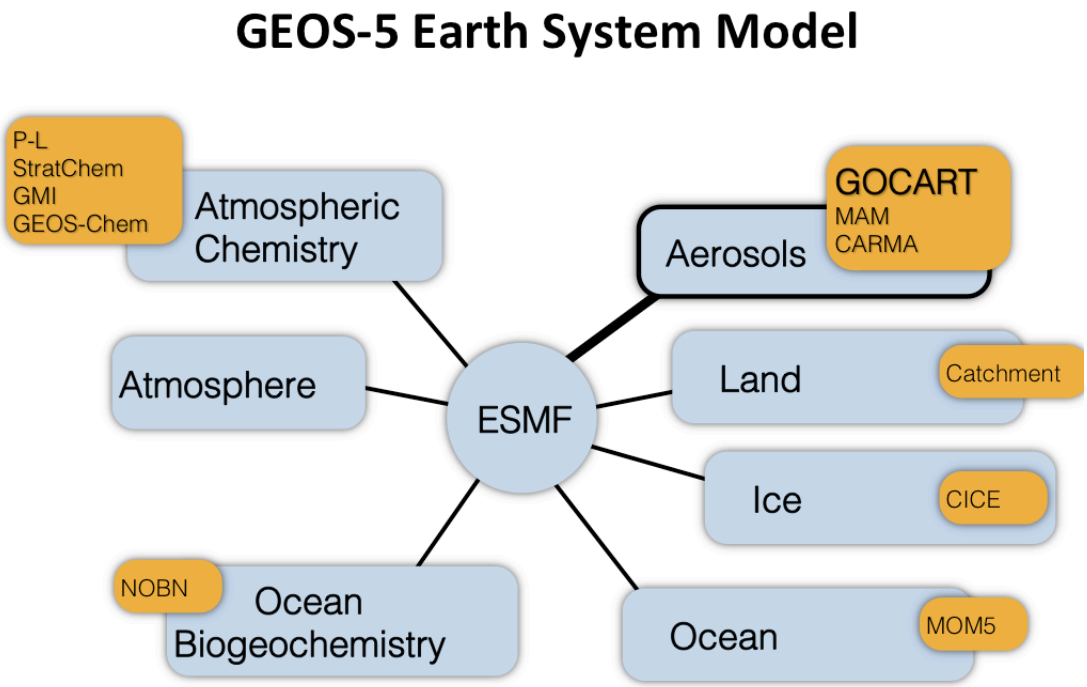

Figure 2.2 The GEOS-5 Model. The various components of the GEOS-5 model are represented in blue, with the specific modules for each component listed in orange. The components of GEOS-5 are integrated using the Earth System Modeling Framework (ESMF). The GOCART module within the Aerosol component is highlighted. *Figure adapted from a slide by Dr. Peter Colarco*

GEOS-5 has 72 vertical layers between the surface and roughly 80 km, and can be run at various horizontal resolutions. The hybrid-sigma vertical coordinate system is used in GEOS-5, where the near-surface vertical layers conform to terrain until eventually blending into pressure coordinates at 180 hPa. GEOS-5 can be setup in the following modes: *forecast* mode, *data assimilation* mode, or *replay* mode. In forecast mode, the model is initialized with meteorological fields and further dynamics are computed, or forecast, from the initial conditions. Data assimilation is similar to the forecast mode, but includes a data assimilation analysis step to evaluate and correct the state of the model meteorology. In replay mode, the model meteorology is updated at temporal intervals using archived meteorology, typically from the Modern Era Retrospective analysis for Research and Applications (MERRA) [*Rienecker et al., 2011*] reanalysis or its successor MERRA-2 [Gelaro et al., 2017].

The GEOS-5 model is capable of adjusting the meteorological fields based on the radiative properties of simulated aerosols, referred to as running "online". When GEOS-5 is run online the optical properties of aerosols are used to compute the effects of radiative heating, which are then applied to the simulation meteorology during the model run. In "offline" mode, the aerosols act like passive tracers that do not affect the meteorological fields. Running GEOS-5 online should yield the advantage of a more realistic representation of aerosol transport.

Aerosols are modeled in GEOS-5 using the internal online Goddard Chemistry, Aerosol, Radiation, and Transport (GOCART) module [*Chin et al., 2000;*

Colarco et al., 2010], shown in Figure 2.. GOCART is equipped to model dust, black carbon, organic carbon, sea salt, and sulfate aerosols. GOCART transports aerosol and chemical species by advection, convection, and turbulent mixing processes. Advection is computed by a flux-form semi-Lagrangian method [*Lin and Rood, 1996*] and archived cloud mass flux fields are used to parameterize the moist convection. Turbulent mixing due to buoyancy and mechanical shear is approximated by eddy diffusion.

To study volcanic SO_2 and ash clouds, the sulfate aerosol and dust modeling capabilities are used. The GOCART sulfate species include dimethyl sulfate (DMS), methanesulfonic acid (MSA), sulfur dioxide (SO_2), and sulfate aerosols. DMS is a naturally occurring byproduct of marine phytoplankton. MSA is a product of DMS oxidation and is lost through deposition. The flux of DMS into the atmosphere is modeled through ocean-air interactions, using a parameterization based on sea-surface wind speeds [*Liss and Merlivat, 1986*]. The DMS parameterization utilizes a climatology of monthly oceanic DMS concentrations [*Kettle et al. 1999*]. Only a small fraction of SO_2 is produced from the oxidation of DMS, with most SO_2 produced from anthropogenic sources like fossil fuel combustion [*US EPA, 2018*]. All non-volcanic SO_2 sources are removed when modeling volcanic eruptions, leaving only the prescribed volcanic SO_2 emissions. SO_2 removal is modeled through wet and dry deposition, and by aqueous and gas phase oxidation into sulfate aerosols. GOCART sulfur species are oxidized using monthly climatological fields of hydrogen peroxide (H_2O_2), hydroxyl (OH), and nitrite (NO_3). These oxidant fields were produced from NASA Global Modeling Initiative (GMI) model simulations

[*Strahan and Douglas, 2004; Duncan et al., 2007*]. When modeling volcanic eruptions, sulfate production is primarily driven by aqueous and gas phase oxidation of SO_2, by H_2O_2 and OH respectively [*Chin et al. 2000*].

GOCART models dust through a sectional approach, allowing for different density and size distributions to be simulated. Dust is removed from the model through gravitational settling and wet and dry deposition. The application of the GOCART dust module for modeling volcanic ash is further detailed in Chapter 3.

The GOCART module requires the following volcanic eruption source terms in order to simulate the transport of a volcanic SO_2 and ash: eruption timing/duration, the SO_2 and ash flux (emission) rates, and the injection altitude profile. Note that modeling ash also requires estimates of the size distributions, density distributions and other optical properties. Using this information, an SO_2 or ash emission flux is imposed in vertical model grid boxes above the volcano, at altitudes that correspond to the injection altitude profile. The GOCART module then simulates the subsequent transport of the ash and SO_2 masses.

2.3 Volcanic Plumes and Volcanic Clouds: Observations

Satellite-based instruments provide various types of observations that give different perspectives of volcanic ash and SO_2 clouds. Satellites can measure a volcanic cloud's horizontal extent, total mass loading (SO_2 and ash), cloud top altitude, profiles of the cloud thickness, and in some cases derive the ash effective particle size [*Bonadonna et al. 2012*]. With the variety of satellite observations also come a variety of advantages and disadvantages. Differences in the satellite's orbit,

whether geostationary or polar-orbiting, can provide more or less frequent observations and different areas of observational coverage. Furthermore, instruments designed to measure in the UV, visible, or IR spectrum carry different benefits and drawbacks. For example, UV and visible instruments only make observations during the daylight part of the satellite orbit, unlike IR instruments. IR instruments have trouble observing into the mid-to-lower troposphere due to interference with water vapor [*Prata and Kerkmann, 2007b*]. These advantages and disadvantages for volcanic ash observations are further outlined in Table 2.1, with most listed issues also extending to SO_2 observations.

Table 2.1 Ash Satellite Observations: Advantages and Disadvantages. This table considers both UV and IR observations from both polar orbiting (Polar) satellites and geostationary (Geo) satellites. *Adapted from a slide by Dr. Arlin Krueger.*

	UV Sensors – *Polar*	IR Sensors - *Polar/Geo*
Measurement Technique (Ash)	*320- 380 nm difference from Rayleigh spectrum*	*10 – 12 nm BTD - Split Window*
Advantages	+ Effective over land or sea + Can be calculated in the presence of clouds	+ Day and Night Times + Operational Satellites + Geo: High spatial and temporal res.
Disadvantages	- Daytime only - Smoke and dust have same signature - Longer latency time	- Misses detections due to water vapor interference and cold clouds – false alarms. - Geo: Poor observations at high latitudes

Collectively, satellite observations can help provide a detailed understanding of volcanic clouds, vital to monitoring their transport. This section contains an overview of instruments and observations that are frequently used in this dissertation.

Details of other observations used in individual studies are provided in the case study's respective chapter.

2.3.1 Satellite UV Observations

Backscatter ultraviolet (BUV) satellite observations have been used to monitor volcanic eruptions since 1979, starting with the Total Ozone Monitoring System (TOMS) [*McPeters et al. 1998*]. TOMS went through several generations before the Ozone Monitoring Instrument (OMI), launched in 2004, ultimately replaced it. OMI is a downward looking push-broom UV spectrometer [*Levelt et al., 2006*] onboard the polar-orbit Aura satellite. OMI images a swath comprised of scan-lines 2,600 km in width (perpendicular to the satellite travelling direction) and 13 km in length (parallel to the satellite travelling directions). An example of an OMI swath is shown Figure 2.3a. Each scan line is broken up into 60 "cross-track" pixels, with nadir having a higher spatial resolution than those closer the edge of the swath. For example, at nadir an OMI pixel has a resolution of 24 km x 13 km, while at the swath edge the resolution is 128 km x 13 km. The daylight part of OMI's polar orbit creates 14 swaths, that collectively provide near global coverage daily.

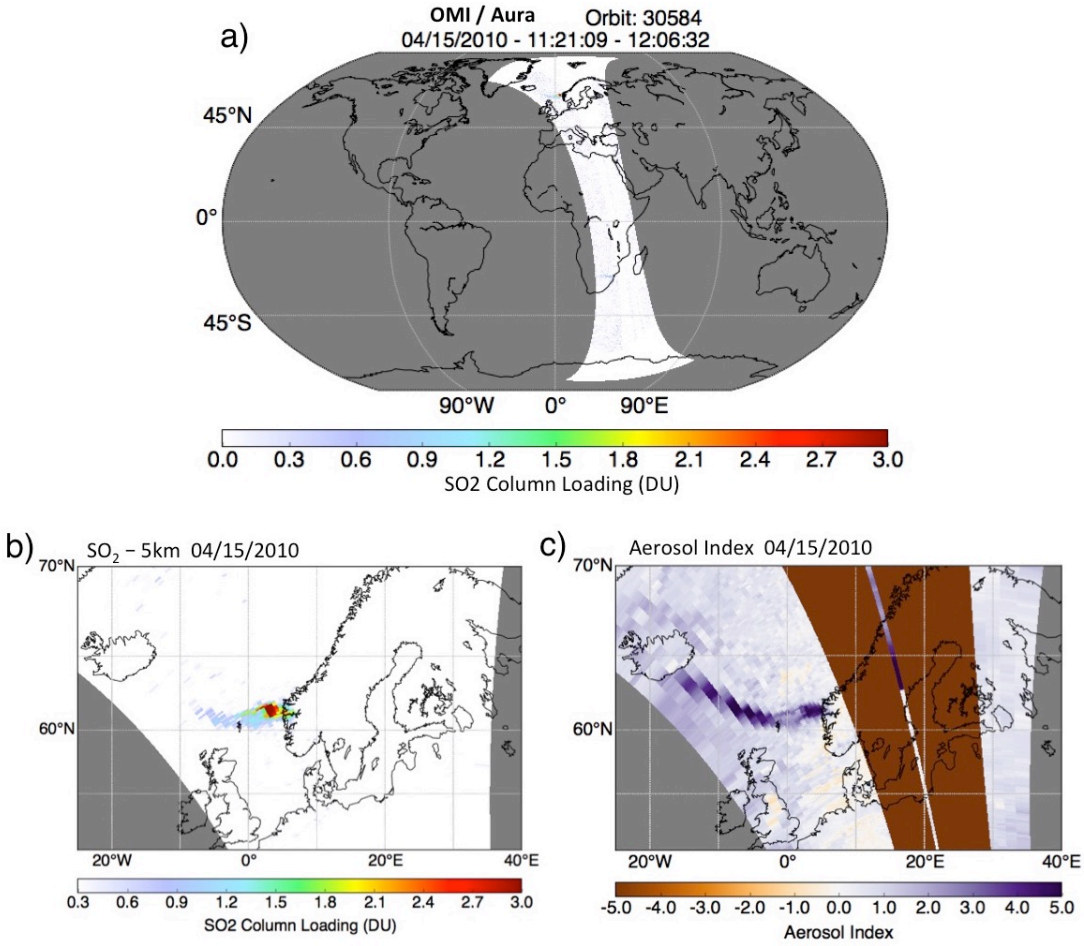

Figure 2.3 OMI Observations of the 2010 Eyjafjallajökull Eruption. A full OMI swath of SO_2 observations is shown in (a). A zoomed in view of the OMI swath is shown in (b) and (c), for SO_2 and Aerosol Index (see E 2.4) respectively. The dark brown vertical strips through the Aerosol Index in (c) represents the row anomaly that is filtered out of the OMI swath. The anomalous observations are similarly filtered out of the SO_2 observations (b), but not shown.

OMI measures the BUV radiance from reflected sunlight in the 270 nm - 500 nm wavelength range. OMI observations are used to derive SO_2 vertical column density maps in Dobson Units (1 DU= $2.69*10^{16}$ molecules SO_2 cm^{-2}) and Aerosol Index (AI). An example of these observations is shown in Figure 2.3b and c, for the 2010 eruption of Eyjafjallajökull.

BUV SO_2 retrieval algorithms generally take advantage of the particular SO_2 absorption sensitivity in the 310 to 340 nm region, shown in Figure 2.4. Atmospheric SO_2 is retrieved from satellite BUV observations by relating the magnitude of the SO_2 absorption observed at the top of the atmosphere (TOA) to the density of SO_2 in the column of the atmosphere being observed. A radiative transfer model (RTM) simulates the BUV radiance at the top of the atmosphere, or simply BUV TOA radiance, by modeling the transfer of electromagnetic radiation through the atmosphere. An RTM can simulate many possible BUV TOA radiances by varying the assumed SO_2 column densities. The actual SO_2 column density is then estimated by finding the particular SO_2 column density that minimizes the difference between the simulated versus observed BUV TOA radiance, i.e., the residual.

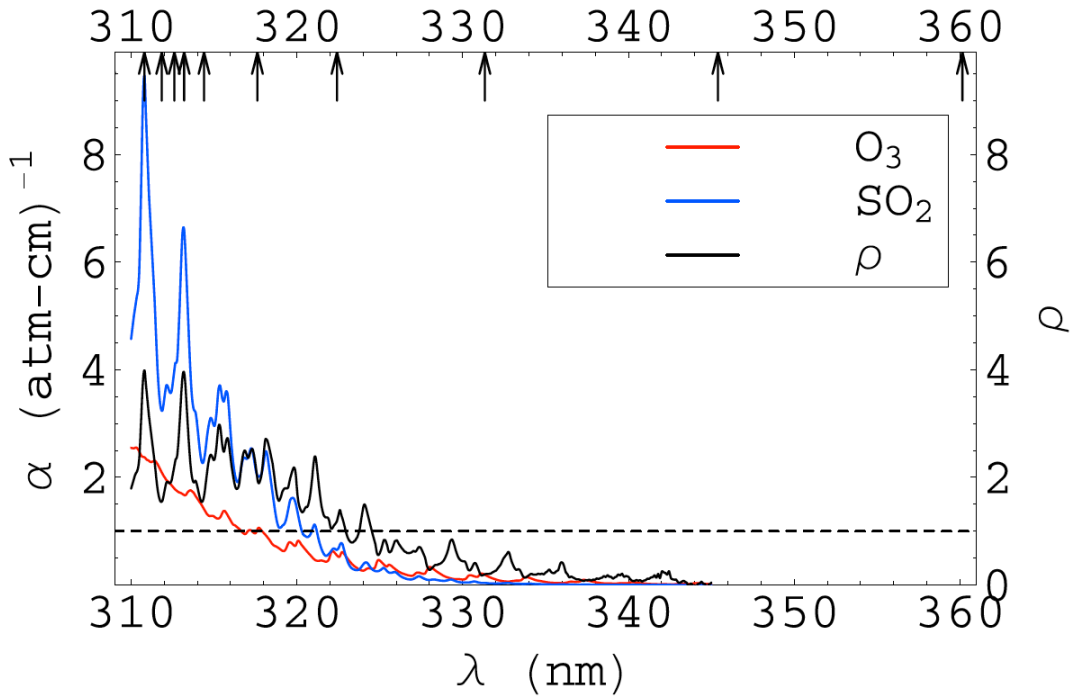

Figure 2.4 SO_2 and O_3 absorption in the UV. The absorption coefficients (α) for SO_2 and O_3 are shown, as well as the ratio of SO_2 to O_3 (ρ). The arrows indicate the wavelength channels used in the OMI O_3 retrieval, OMTO3. Source [*Yang et al. 2007*]

OMI SO_2 products have been generated using different retrieval algorithms across the instrument's lifetime. Initially, the SO_2 products were derived using the Band-Residual Difference (BRD) algorithm [*Krotkov et al. 2006*]. The BRD algorithm uses wavelength band pairs to measure the magnitude of the SO_2 absorption at wavelengths sensitive to the SO_2 column. The band pairs consist of a wavelength band centered on a SO_2 absorption maximum and another centered-on a nearby SO_2 absorption minimum, with their difference yielding the SO_2 absorption magnitude. The algorithm solves the RTM finding an input SO_2 column density that minimizes the residual. At larger SO_2 column masses, the BRD algorithm becomes uncertain as SO_2 band pair residual differences no longer have linear and monotonic

responses to increases in SO_2 [*Yang et al. 2007*]. The OMI SO_2 algorithm was updated to use the Linear Fit algorithm of Yang et al. [*2007*]. The Linear Fit (LF) algorithm provided better estimates of large SO_2 columns since it could use longer wavelengths (> 320nm), where the SO_2 absorption was weaker, but yields a more linear response to changes in the SO_2 column density [*Yang et al., 2007*]. The LF algorithm differs from the BRD algorithm by using the measured TOA radiance, at various wavelengths, to simultaneously estimate the vertical columns of O_3, SO_2 and the surface reflectivity. The algorithm works by trying to minimize the residuals using a RTM conditioned on vertical column O_3, SO_2, and reflectivity. Namely:

$$I_m = I(\Omega, \Xi, R) + \varepsilon \qquad \text{(E 2.3)}$$

where I_m represents the measured TOA radiance and I is the modeled TOA radiance given the vertical columns of ozone (Ω), SO_2 (Ξ), and reflectivity (R). The error is represented as ε. The radiances are computed in terms of the N-value, $N = -100 \log_{10} I$, with the modeled TOA radiance N-value defined as the sum of the TOA radiance from the individual variables: Ω, Ξ, and R. The algorithm then becomes a minimization problem, where residuals are minimized to yield the best fit between the residuals across all variables and for all wavelength bands used in the algorithm.

The current OMI SO_2 data archive has been reprocessed to use the principal component analysis (PCA) algorithm by Li et al. [*2013*] to derive column SO_2 observations. The PCA is, in general, a method of reducing the dimensionality of a data set by converting possibly correlated observations into a set of linearly uncorrelated observations, or Principle Components (PCs). Li et al [*2013*] applied this method to decompose the measured BUV radiance spectrum into the different

effects and processes that the radiance spectrum describes. When applied to a radiance spectrum measuring an SO_2 free atmosphere, the main PCs describe geophysical effects, like O_3 absorption and rotational Raman Scattering, and instrument effects like dark current variations [*Li et al., 2013*]. The PCA algorithm works by assuming that the observed BUV radiance spectrum can then be described as a combination of the SO_2-free PCs and the pre-calculated SO_2 residuals. The PCs and the SO_2 residuals are fit to the observed BUV irradiance spectrum, where the SO_2 residual that provides the best fit describes the total column SO_2 density.

All of the previously mentioned SO_2 retrieval algorithms exploit the sensitivity of the SO_2 vertical column density on the SO_2 absorption observed at the TOA radiance, however, the TOA radiance is also sensitive to the altitude of SO_2. The atmosphere attenuates the measured SO_2 signal, so an SO_2 cloud near the earth's surface will have a much weaker measured absorption then an identical SO_2 clouds much higher in the atmosphere, closer the satellite. Since the vertical structure of the SO_2 cloud is unknown, it must be assumed in order to derive the total column SO_2 density. Both current and past algorithms have generated SO_2 products for different assumed vertical SO_2 profiles. There are currently four SO_2 products being generated: SO_2 PBL (Pressure Boundary Layer), SO_2 TRL (Tropospheric, Lower), SO_2 TRM (Tropospheric, Middle), and SO_2 STL (Stratospheric, Lower). The SO_2 PBL was chosen to represent the vertical profile of air pollution and assumes a center of mass altitude (CMA) of about 1 km. The TRL, TRM, STL SO_2 products were chosen to represent passively degassing volcanic eruptions (CMA = 3km), moderate

volcanic eruptions (CMA = 8km) and large volcanic eruptions (CMA=18km), respectively [*Li et al., 2017*].

The Aerosol Index (AI), or Absorbing Aerosol Index, describes the ratio of the measured radiance to the radiance expected from molecular (Rayleigh-only) scattering atmosphere [*Torres et al., 1998*]. The AI is defined as:

$$AI = 100\ log_{10}\left(\frac{I_{340}^{Meas}}{I_{340}^{Calc}}\right) \qquad \text{(E 2.4)}$$

where I_{340}^{Meas} represents the measured radiance at 340nm and I_{340}^{Calc} is the radiance at 340nm calculated for a Rayleigh-only atmosphere (and spectrally flat lambertian effective reflectivity derived by matching calculated and measured radiances at 380nm). A positive AI indicates the presence of absorbing aerosols, such as dust and volcanic ash (above ~1500 m altitude), whereas near-zero AI indicates large non-absorbing aerosol particles or no aerosols at all [*Torres et al. 2007*]. The AI has proven itself a useful tool to aid in monitoring volcanic ash clouds [*Krotkov et al., 1997, 1999ab, Krueger et al., 2008*] and is currently used operationally to track volcanic ash clouds [*Brenot et al., 2014*].

In June 2007, OMI observations began detecting anomalous observations along the central (near nadir) positions of the OMI swath (see http://projects.knmi.nl/omi/research/product/rowanomaly-background.php). As a result, portions of the OMI's central swath must be filtered out. This is shown in Figure 2.3c.

The Ozone Mapping Profiler Suite (OMPS), on board the NASA-NOAA Suomi National Polar-orbiting Partnership (S-NPP) [*Flynn et al., 2014*] launched in

2011, continues the legacy of BUV SO_2 and AI observations. Similar to OMI, OMPS contains a downward-looking push-broom UV spectrometer (nadir mapper) that measures radiance from 300 to 380 nm. Unlike other UV instruments, OMPS on S-NPP also contains a UV backward-looking limb profiler (OMPS LP) used to derive extinction profiles [*Gorkavyi et al., 2013*], and capable of measuring the vertical structure of aerosols in the atmosphere.

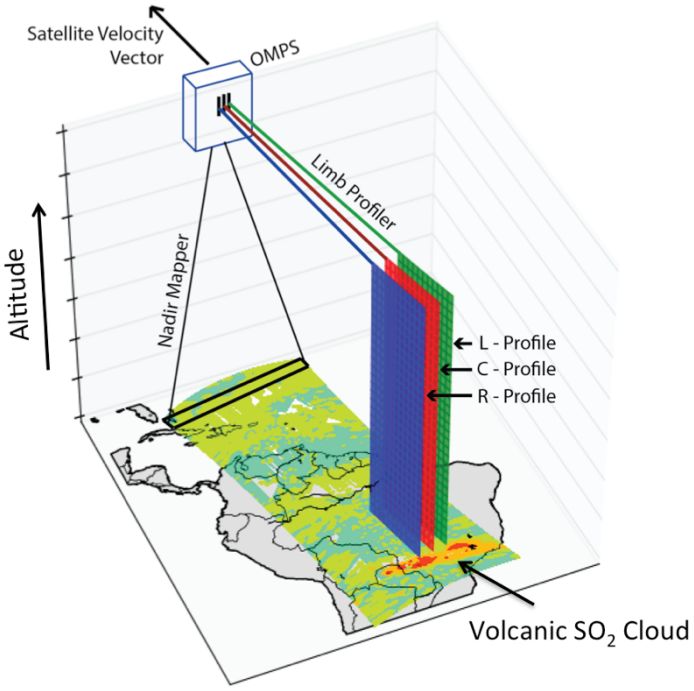

Figure 2.5 Illustration of OMPS observations. Observations from the nadir mapper are shown, over South America. The backward looking limb profiler observes three different atmospheric profiles, labeled the right (R) profile, center (C) profile, and left (L) profile. The profiles shown illustrate the sampling region, but actual observational data is not shown.

OMPS LP observations were initially used to retrieve profiles of the aerosol scattering index (ASI). The ASI is similar to the AI, in that it describes the difference between the measured radiances and radiances computed assuming a "clean" atmosphere:

$$ASI(\lambda, z) = \frac{I_{meas}(\lambda,z) - I_{Ray}(\lambda,z)}{I_{Ray}(\lambda,z)} \qquad \text{(E 2.5)}$$

where $I_{meas}(\lambda, z)$ is the measured radiance and $I_{Ray}(\lambda, z)$ the computed Rayleigh-only radiance, at wavelength λ and altitude z. Examples of OMPS nadir and limb profiler observations are shown in Figure 2..

At nadir, the OMPS nadir pixel size of 50 km x 50 km is notably larger than that of its predecessor OMI (13 km by 24 km), but the higher signal–to-noise ratio makes OMPS suitable for both volcanic and anthropogenic SO_2 observations [*Yang et al., 2013; Carn et al., 2015; Li et al., 2017*]. Currently, OMPS column SO_2 data are derived using the PCA algorithm of Li et al. [*2013*]. OMPS SO_2 observations are produced for the same height assumptions as previously noted for OMI. OMPS observations are also used to derive the aerosol index (AI).

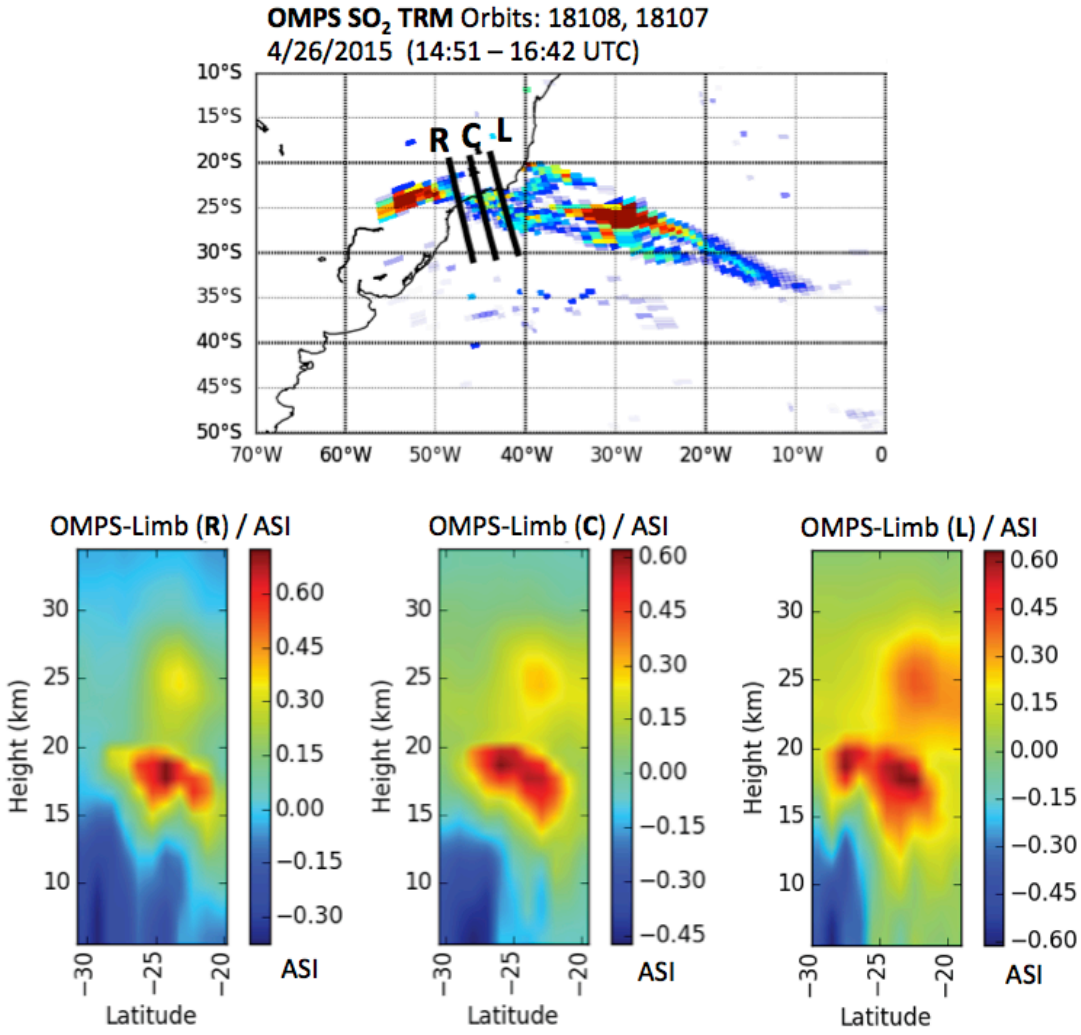

Figure 2.6 OMPS observations of the 2015 eruption of Calbuco. The top panel shows OMPS nadir mapper SO_2 observations for orbits 18107 and 18108, from April 26th 2015. The OMPS limb profiler Aerosol Scattering Index (ASI) observations are shown in the bottom three panels, for λ=675nm. The ground tracks of the limb profiles are shown in black in the top panel.

2.3.2 CALIOP and CATS Aerosol Profiles

Satellite lidar (light detection and ranging) instruments use a pulsed laser system to observe the vertical distribution of aerosols in the atmosphere by measuring attenuated light backscattering along the laser's path. The Cloud-Aerosol Lidar with

Orthogonal Polarization (CALIOP) [*Winker et al., 2009*] and Cloud-Aerosol Transport System (CATS) [*McGill et al., 2015; Yorks et al., 2016*] satellite lidar instruments provide curtain-like profiles of aerosols and clouds in the atmosphere. An example of this type of observation is shown in Figure 2.. The attenuated total backscatter (ATB or β'), with units of km^{-1} sr^{-1}, is the primary parameter of CATS and CALIOP. The ATB is the sum of the parallel and perpendicular polarization components and is derived from the calibrated, range-corrected, laser energy normalized, background subtracted raw photon count signal. It is "attenuated" because it includes the atmospheric extinction and "total" because it comprises the backscatter and extinction contributions from both molecules and particulates. The ATB profiles from CALIOP and CATS have frequently been used to study sulfate aerosols and ash within volcanic clouds, and better understand their vertical distributions [*Winker et al., 2012; Vernier et al., 2013; Hughes et al., 2016*]. The depolarization of the backscatter is also measured to assess the shape of the scattering aerosols, where low depolarization indicates spherical particles, like sulfate aerosols, and high polarization indicates aerosols with more complex and non-uniform structures, like some ice crystals and volcanic ash.

A drawback to these types of observations is their narrow FOV, limiting their height observations to describing only a part of the volcanic cloud. For example, CATS has a 350m horizontal resolution. Nonetheless, these direct observations provide crucial data that can be used to verify and correct altitudes estimated from other means.

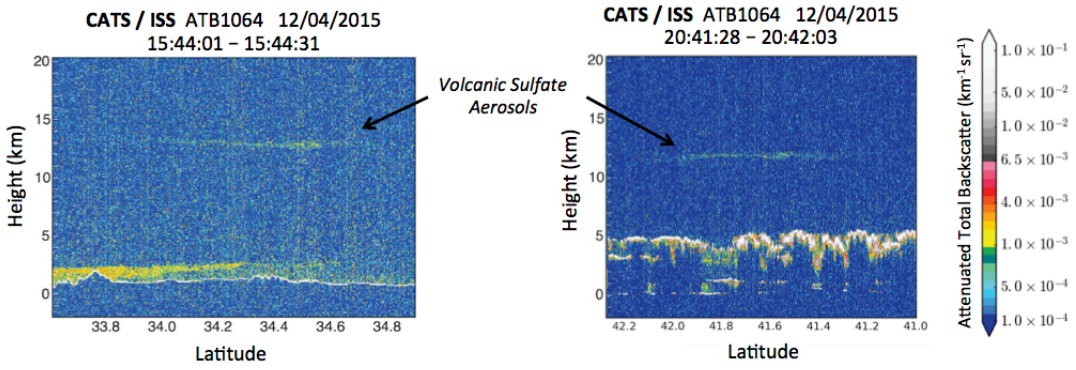

Figure 2.7 CATS observations of volcanic sulfate aerosols. Two profiles of the Attenuated Total Backscatter (ATB) show the vertical distribution of sulfate aerosols in a volcanic cloud that erupted from Mt. Etna. The left panel is a daytime observation, which tend to be noisier than nighttime observaions, shown on the right.

2.4 Volcanic Plumes and Volcanic Clouds: Source Terms

Satellite observations provide a wealth of information that helps us better understand volcanic clouds, but rarely capture information about the volcanic plume. Modeling volcanic clouds requires an estimate of the volcanic emission source terms, namely the altitude distribution of the emissions and the temporal evolution of the emission flux. The following sections describe methods that utilize both satellite observations and models to estimate and refine volcanic emission source terms, to improve volcanic cloud simulations.

2.4.1 Volcanic Plume Altitude

In the absence of direct altitude observations, the observed transport path of a volcanic cloud can be used to deduce the altitude. A common method compares

trajectories at varying altitudes with the observed transport, and deduces the correct altitude from the trajectory that best matches the observed transport path. [*Schoeberl et al. 1993; Allen et al. 1999; Prata and Bernardo, 2007a; Krotkov et al. 2010; Yang et al. 2010*]. A recent method by Hughes et al. [*2012*] built on the idea of using unique transport characteristics to derive injection altitude information by using backward trajectories.

Trajectories describe the path taken by a parcel of air in the atmosphere. Since volcanic SO_2 generally acts as a passive atmospheric tracer, trajectories can also be used to describe the path of SO_2 containing air parcels. Trajectories are initialized at a given time, location, and altitude in the atmosphere, and driven either backwards or forwards in time using meteorological wind fields. For volcanic SO_2 observations, the altitude of the SO_2 air parcel is generally unknown, yet their origin is well defined. In other words, the end point of a volcanic SO_2 trajectory driven backwards in time should be the volcano. Thus, the altitude of the SO_2 parcel can be deduced by finding the parcel initialization height that yields a trajectory that travels back to the volcano. An example of back trajectories initialized from OMPS volcanic SO_2 observations is shown in Figure 2.8, from an eruption of Mt. Etna. This example shows two different initialization altitudes, demonstrating that the 11 km altitude tracks back to the volcano better than the 14 km initialization.

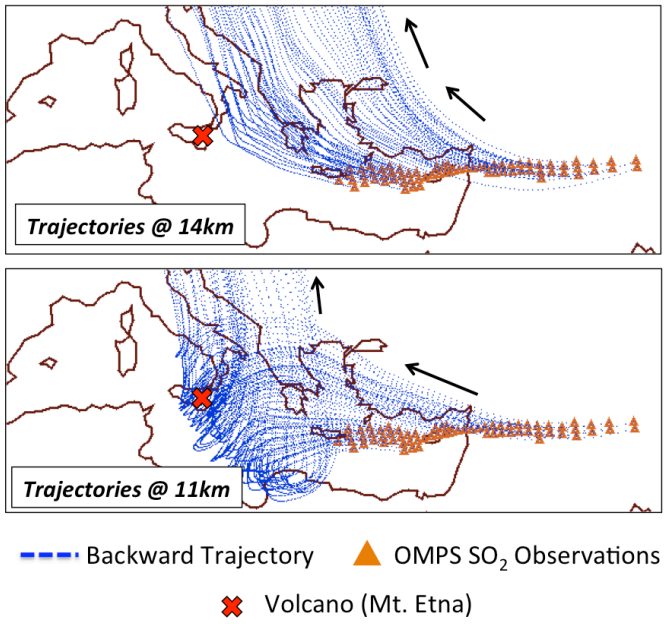

Figure 2.8 Backward trajectories from volcanic SO_2 observations. The top panel shows trajectories initialized at 14 km, and the bottom panel shows trajectories initialized at 11 km. OMPS SO_2 observations are represented as orange triangles, with the trajectory paths traced in dashed blue lines. The volcanic SO_2 was erupted from Mt. Etna, shown as a red cross.

In Hughes et al. [*2012*], vertical stacks of trajectories are initialized at successive volcanic SO_2 observations and driven backwards in time. Trajectories that travel back to the volcano are considered to have successfully described a potential transport path for an SO_2 observation and are collected in a trajectory ensemble.

Trajectory arrival at the volcano is defined as arriving within a minimum distance, R*, to the volcano. In Hughes et al. [*2012*], an R* of 700 km is used. In order to build a sound trajectory ensemble, Hughes et al. [*2012*] initialized trajectories at successive observations of the SO_2 cloud's location, having the effect of reinforcing the true transport path over the spurious noise created by trajectories that coincidently arrive within R* of the volcano. The trajectory ensemble is used to derive the probability of trajectory arrival time at the volcano, $P(t^*)$, and the joint probability of trajectory arrival time and arrival altitude, $P(h,t^*)$. Figure 2.9, shows an example of these PDFs.

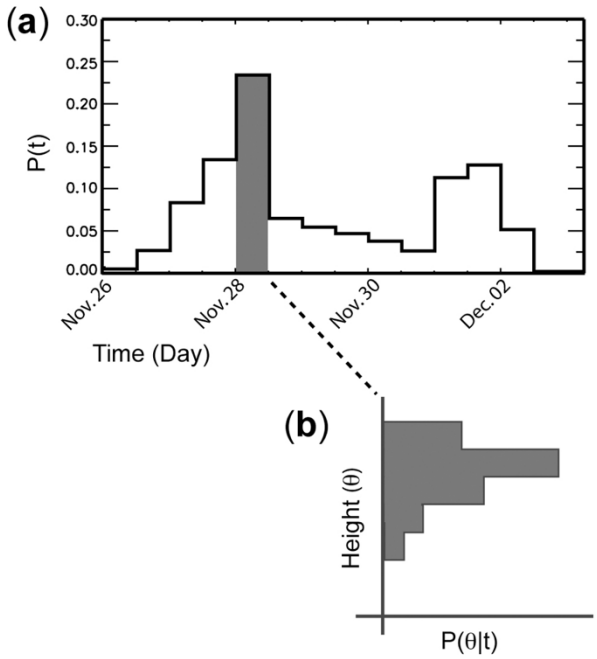

Figure 2.9 Illustration of P(t*) and P(h,t*). The probability of trajectory arrival time, $P(t^*)$, is shown in (a), and the arrival time and height probability, $P(h|t^*)$ for a specific time bin is shown in (b). In this example, height was expressed in terms of theta-levels, θ. (Source: [*Hughes et al. 2012*])

The back trajectories are advected by prescribed winds fields and do not undergo irreversible processes, such as diffusion or turbulent mixing, so the arrival time of a trajectory at the volcano can also be described as the time a trajectory would be emitted from the volcano to arrive at an SO_2 observation, or simply the SO_2 emission time. Thus, P(t*) can also be referred to as probability of emission time and P(h,t*) as the joint probability of emission altitude and emission time.

An alternative approach to source term estimation follows an inversion approach, where Eckhardt et al. [*2008*] combined satellite column SO_2 observations with a transport model to derive the initial vertical mass distribution of volcanic SO_2 emissions. This methodology derives a relationship between the initial emission column and the location of downstream observations of SO_2. This relationship is then used to drive an inversion of the SO_2 observations, yielding an estimate of the initial

vertical mass distribution for the volcanic SO_2 emissions. This method initially only assumed a fixed initial emission time, but was later updated to yield an emission height time-series for volcanic ash [*Stohl et al. 2011*], using assumed ash size and density distributions.

2.4.2 Mass Flux

Estimating the SO_2 mass flux has been achieved by utilizing the observed total SO_2 mass in freshly erupted clouds [*Hughes et al. 2016, Flemming and Inness, 2013*], and most notably in the TOMS/OMI/OMPS volcanic SO_2 inventory [*Carn et al. 2015*] (http://SO_2.gsfc.nasa.gov/measures.html) and the AEROCOM volcanic SO_2 emissions inventory [*Diehl et al. 2012*]. The total mass loading can be directly translated into mass flux if the duration of the eruption is known, and mass flux is assumed constant during this duration.

For volcanic ash, studies have outlined an empirical relationship between the volcanic plume injection height and the mass flux of volcanic ash emitted at the vent [e.g., *Wilson and Walker, 1987; Sparks et al., 1997; Mastin et al., 2009*], noted as the mass emission rate (MER)-height relationship. This dissertation uses the relationship derived by Mastin et al. [*2009*]:

$$H = 2.00\, V^{0.241} \qquad \text{(E 2.6)}$$

where H is the altitude (in meters) of the volcanic plume umbrella cloud and V is the ash volumetric flow rate (in m^3) of dense rock equivalent (DRE). It is important to note that equation (E 2.6) describes the total volume of ash emitted from a volcanic eruption. The research presented in this dissertation is mainly focused on the fraction

of volcanic ash particles small enough for long distance transport away from the volcano, as gravitational settling will cause larger ash particles to quickly fall out of the volcanic cloud. Thus, we should expect the ash flux source terms derived from this relationship to overestimate the amount of ash observed by satellites. The MER-height relationship primarily provides an initial estimate of the volcanic ash mass flux.

Volcanically erupted clouds of ash and SO_2 are monitored by satellites that map their horizontal extent, and profilers that measure the vertical distribution of the aerosols within. Transport models can help forecast the dispersion of volcanic ash and SO_2 clouds, and observations can help estimate emission source terms needed to initialize transport models. Analysis methods that help translate observations into emission source parameters were also detailed. The following chapters make use of the models, observations, and analysis methods described here to answer the key scientific questions of this dissertation.

References, Chapter 2

Allen, D. R., M. R. Schoeberl, and J. R. Herman. "Trajectory modeling of aerosol clouds observed by TOMS." Journal of Geophysical Research: Atmospheres 104, no. D22 (1999): 27461-27471.

Aquila, V., L. D. Oman, R. S. Stolarski, P. R. Colarco, and P. A. Newman (2012), Dispersion of the volcanic sulfate cloud from a Mount Pinatubo–like eruption, Journal of Geophysical Research: Atmospheres, 117(D6).

Bonadonna, Costanza, Arnau Folch, Susan Loughlin, and Herbert Puempel. "Future developments in modelling and monitoring of volcanic ash clouds: outcomes from the first IAVCEI-WMO workshop on Ash Dispersal Forecast and Civil Aviation." Bulletin of volcanology 74, no. 1 (2012): 1-10.

Brenot, Hugues, Nicolas Theys, Lieven Clarisse, J. Van Geffen, Jeroen Van Gent, Michel Van Roozendael, R. Van Der A et al. "Support to Aviation Control Service (SACS): an online service for near real-time satellite monitoring of volcanic plumes." Natural hazards and earth system sciences 14, no. 5 (2014): 1099-1123.

Bursik, M. "Effect of wind on the rise height of volcanic plumes." Geophysical Research Letters 28, no. 18 (2001): 3621-3624.

Carn, S. A., K. Yang, A. J. Prata, and N. A. Krotkov. "Extending the long-term record of volcanic SO_2 emissions with the Ozone Mapping and Profiler Suite nadir mapper." Geophysical Research Letters 42, no. 3 (2015): 925-932.

Chin, Mian, Richard B. Rood, Shian-Jiann Lin, Jean-Francois Müller, and Anne M. Thompson. "Atmospheric sulfur cycle simulated in the global model GOCART: Model description and global properties." Journal of Geophysical Research: Atmospheres 105, no. D20 (2000): 24671-24687.

Colarco, Peter, Arlindo da Silva, Mian Chin, and Thomas Diehl. "Online simulations of global aerosol distributions in the NASA GEOS-4 model and comparisons to satellite and ground-based aerosol optical depth." Journal of Geophysical Research: Atmospheres 115, no. D14 (2010).

Diehl, T., A. Heil, M. Chin, X. Pan, D. Streets, M. Schultz, and S. Kinne. "Anthropogenic, biomass burning, and volcanic emissions of black carbon, organic carbon, and SO_2 from 1980 to 2010 for hindcast model experiments." Atmospheric Chemistry and Physics Discussions 9 (2012): 24895-24954.

Duncan, B. N., Strahan, S. E., Yoshida, Y., Steenrod, S. D., and Livesey, N.: Model study of the cross-tropopause transport of
biomass burning pollution, Atmos. Chem. Phys., 7, 3713–3736, doi:10.5194/acp-7-3713-2007, 2007.

Eckhardt, S., A. J. Prata, P. Seibert, K. Stebel, and A. Stohl. "Estimation of the vertical profile of sulfur dioxide injection into the atmosphere by a volcanic eruption using satellite column measurements and inverse transport modeling." Atmospheric Chemistry and Physics 8, no. 14 (2008): 3881-3897.

Folch, Arnau, Antonio Costa, and Sara Basart. "Validation of the FALL3D ash dispersion model using observations of the 2010 Eyjafjallajökull volcanic ash clouds." Atmospheric Environment 48 (2012): 165-183.

Flemming, Johannes, and Antje Inness. "Volcanic sulfur dioxide plume forecasts based on UV satellite retrievals for the 2011 Grímsvötn and the 2010 Eyjafjallajökull eruption." Journal of Geophysical Research: Atmospheres 118, no. 17 (2013).

Flynn, L., C. Long, X. Wu, R. Evans, C. T. Beck, I. Petropavlovskikh, G. McConville et al. "Performance of the ozone mapping and profiler suite (OMPS) products." Journal of Geophysical Research: Atmospheres 119, no. 10 (2014): 6181-6195.

Gelaro, Ronald, Will McCarty, Max J. Suárez, Ricardo Todling, Andrea Molod, Lawrence Takacs, Cynthia A. Randles et al. "The modern-era retrospective analysis for research and applications, version 2 (MERRA-2)." Journal of Climate 30, no. 14 (2017): 5419-5454.

Gorkavyi, Nick, D. F. Rault, P. A. Newman, A. M. Silva, and A. E. Dudorov. "New stratospheric dust belt due to the Chelyabinsk bolide." Geophysical Research Letters 40, no. 17 (2013): 4728-4733.

Hughes, E. J., L. C. Sparling, S. A. Carn, and A. J. Krueger. "Using horizontal transport characteristics to infer an emission height time series of volcanic SO_2." Journal of Geophysical Research: Atmospheres 117, no. D18 (2012).

Hughes, E. J., J. Yorks, N. A. Krotkov, A. M. Silva, and M. McGill. "Using CATS near-real-time lidar observations to monitor and constrain volcanic sulfur dioxide (SO_2) forecasts." Geophysical Research Letters 43, no. 20 (2016).

Kettle, A. J., M. O. Andreae, D. Amouroux, T. W. Andreae, T. S. Bates, H. Berresheim, H. Bingemer et al. "A global database of sea surface dimethylsulfide (DMS) measurements and a procedure to predict sea surface DMS as a function of latitude, longitude, and month." *Global Biogeochemical Cycles* 13, no. 2 (1999): 399-444.

Krueger, Arlin, Nickolay Krotkov, and Simon Carn. "El Chichon: The genesis of volcanic sulfur dioxide monitoring from space." Journal of Volcanology and Geothermal Research 175, no. 4 (2008): 408-414.

Krotkov, Nickolay A., Simon A. Carn, Arlin J. Krueger, Pawan K. Bhartia, and Kai Yang. "Band residual difference algorithm for retrieval of SO/sub 2/from the aura ozone monitoring instrument (OMI)." IEEE transactions on geoscience and remote sensing 44, no. 5 (2006): 1259-1266.

Krotkov, N. A., M. R. Schoeberl, G. A. Morris, S. Carn, and K. Yang. "Dispersion and lifetime of the SO_2 cloud from the August 2008 Kasatochi eruption." Journal of Geophysical Research: Atmospheres 115, no. D2 (2010).

Krotkov, N. A., O. Torres, C. Seftor, A. J. Krueger, A. Kostinski, W. I. Rose, G. J. S. Bluth, D. Schneider, and S. J. Schaefer (1999), Comparison of TOMS and AVHRR volcanic ash retrievals from the August 1992 eruption of Mt. Spurr, *Geophys. Res. Lett.*, 26(4), 455–458.

Krotkov, N.A., D.E. Flittner, A.J. Krueger, A. Kostinski, C. Riley and W. Rose, O. Torres, (1999) Effect of particle non-sphericity on satellite monitoring of drifting volcanic ash clouds, JQSRT, **63**, 613-630.

Krotkov, N. A., A. J. Krueger, and P. K. Bhartia (1997), Ultraviolet optical model of volcanic clouds for remote sensing of ash and sulfur dioxide, *J. Geophys. Res.*, 102(D18), 21891-21904, 10.1029/97JD01690.

Levelt, Pieternel F., Gijsbertus HJ van den Oord, Marcel R. Dobber, Anssi Malkki, Huib Visser, Johan de Vries, Piet Stammes, Jens OV Lundell, and Heikki Saari. "The ozone monitoring instrument." IEEE Transactions on geoscience and remote sensing 44, no. 5 (2006): 1093-1101.

Li, Can, Joanna Joiner, Nickolay A. Krotkov, and Pawan K. Bhartia. "A fast and sensitive new satellite SO_2 retrieval algorithm based on principal component analysis: Application to the ozone monitoring instrument." Geophysical Research Letters 40, no. 23 (2013): 6314-6318.

Li, Can, Nickolay A. Krotkov, Simon Carn, Yan Zhang, Robert JD Spurr, and Joanna Joiner. "New-generation NASA Aura Ozone Monitoring Instrument (OMI) volcanic SO2 dataset: Algorithm description, initial results, and continuation with the Suomi-NPP Ozone Mapping and Profiler Suite (OMPS)." Atmospheric Measurement Techniques 10, no. 2 (2017): 445.

Lin, Shian-Jiann, and Richard B. Rood. "Multidimensional flux-form semi-Lagrangian transport schemes." Monthly Weather Review 124, no. 9 (1996): 2046-2070.

Liss, Peter S., and Liliane Merlivat. "Air-sea gas exchange rates: Introduction and synthesis." In *The role of air-sea exchange in geochemical cycling*, pp. 113-127. Springer, Dordrecht, 1986.

Mastin, Larry G., M. Guffanti, R. Servranckx, P. Webley, S. Barsotti, K. Dean, A. Durant et al. "A multidisciplinary effort to assign realistic source parameters to models of volcanic ash-cloud transport and dispersion during eruptions." Journal of Volcanology and Geothermal Research 186, no. 1-2 (2009): 10-21.

Matthias, V., A. Aulinger, J. Bieser, J. Cuesta, B. Geyer, B. Langmann, I. Serikov, I. Mattis, A. Minikin, and L. Mona (2012), The ash dispersion over Europe during the Eyjafjallajökull eruption–Comparison of CMAQ simulations to remote sensing and air-borne in-situ observations, Atmospheric Environment, 48, 184-194.

McPeters, Richard D., P. K. Bhartia, Arlin J. Krueger, Jay R. Herman, Charles G. Wellemeyer, Colin J. Seftor, Glen Jaross et al. "Earth probe total ozone mapping spectrometer (TOMS): data products user's guide." (1998).

McGill, Matthew J., John E. Yorks, V. Stanley Scott, Andrew W. Kupchock, and Patrick A. Selmer. "The Cloud-Aerosol Transport System (CATS): A technology demonstration on the International Space Station." Lidar Remote Sensing for Environmental Monitoring XV 9612 (2015): 96120A.

Niemeier, U., C. Timmreck, H-F. Graf, S. Kinne, S. Rast, and S. Self. "Initial fate of fine ash and sulfur from large volcanic eruptions." Atmospheric Chemistry and Physics 9, no. 22 (2009): 9043-9057.

Prata, A. J., and C. Bernardo. "Retrieval of volcanic SO_2 column abundance from Atmospheric Infrared Sounder data." Journal of Geophysical Research: Atmospheres 112, no. D20 (2007a).

Prata, A. J., and J. Kerkmann. "Simultaneous retrieval of volcanic ash and SO2 using MSG-SEVIRI measurements." *Geophysical Research Letters* 34, no. 5 (2007b).

Prata, A. J., and A. Tupper. "Aviation hazards from volcanoes: the state of the science." (2009): 239-244.

Rienecker, M., Suarez, M. J., Gelaro, R., Todling, R., Bacmeister, J., Liu, E., Bosilovich, M. G., Schubert, S. D., Takacs, L., Kim, G.-K., Bloom, S., Chen, J., Collins, D., Conaty, A., da Silva, A., Gu, W., Joiner, J., Koster, R. D., Lucchesi, R., Molod, A., Owens, T., Pawson, S., Pegion, P., Redder, C. R., Reichle, R., Robertson, F. R., Ruddick, A. G., Sienkiewicz, M., and Woollen, J.: MERRA – NASA's Modern-Era Retrospective Analysis for Research and Applications, J. Climate, 24, 3624–3648, doi:10.1175/JCLI-D-11-00015.1, 2011.

Robock, A. (2000), Volcanic eruptions and climate, Reviews of Geophysics, 38(2), 191-219.

Schoeberl, Mark R., Scott D. Doiron, Leslie R. Lait, Paul A. Newman, and Arlin J. Krueger. "A simulation of the Cerro Hudson SO_2 cloud." Journal of Geophysical Research: Atmospheres 98, no. D2 (1993): 2949-2955.

Shipley, Susan, and A. M. Sarna-Wojcicki. "Distribution, thickness, and mass of late Pleistocene and Holocene tephra from major volcanoes in the northwestern United States: a preliminary assessment of hazards from volcanic ejecta to nuclear reactors in the Pacific Northwest." US Geological Survey Miscellaneous Field Studies Map MF-1435 (1982).

Sparks, R. S. J. "The dimensions and dynamics of volcanic eruption columns." Bulletin of Volcanology 48, no. 1 (1986): 3-15.

Sparks, Robert Stephen John, M. I. Bursik, S. N. Carey, Jennifer Gilbert, L. S. Glaze, H. Sigurdsson, and A. W. Woods. "Volcanic plumes." (1997).

Stohl, Andreas, A. J. Prata, Sabine Eckhardt, Lieven Clarisse, A. Durant, S. Henne, Nina Iren Kristiansen et al. "Determination of time-and height-resolved volcanic ash emissions and their use for quantitative ash dispersion modeling: the 2010 Eyjafjallajökull eruption." Atmospheric Chemistry and Physics 11, no. 9 (2011): 4333-4351.

Stevenson, David S., Colin E. Johnson, William J. Collins, and Richard G. Derwent. "The tropospheric sulphur cycle and the role of volcanic SO_2." *Geological Society, London, Special Publications* 213, no. 1 (2003): 295-305.

Strahan, S. E. and Douglass, A. R.: Evaluating the credibility of transport processes in simulations of ozone recovery using the Global Modeling Initiative three-dimensional model, J. Geophys. Res., 109, D05110, doi:10.1029/2003JD004238, 2004.

Suarez, Max J., M. M. Rienecker, R. Todling, J. Bacmeister, L. Takacs, H. C. Liu, W. Gu et al. "The GEOS-5 Data Assimilation System-Documentation of Versions 5.0. 1, 5.1. 0, and 5.2. 0." (2008).

Suzuki, Yujiro J., Takehiro Koyaguchi, Masaki Ogawa, and Izumi Hachisu. "A numerical study of turbulent mixing in eruption clouds using a three-dimensional fluid dynamics model." Journal of Geophysical Research: Solid Earth 110, no. B8 (2005).

Torres, Omar, Aapo Tanskanen, Ben Veihelmann, Changwoo Ahn, Remco Braak, Pawan K. Bhartia, Pepijn Veefkind, and Pieternel Levelt. "Aerosols and surface UV products from Ozone Monitoring Instrument observations: An overview." Journal of Geophysical Research: Atmospheres 112, no. D24 (2007).

Torres, O., P. K. Bhartia, J. R. Herman, Z. Ahmad, and J. Gleason. "Derivation of aerosol properties from satellite measurements of backscattered ultraviolet radiation: Theoretical basis." Journal of Geophysical Research: Atmospheres 103, no. D14 (1998): 17099-17110.

United States Environmental Protection Agency: Retrieved from the EPA Air Quality System website, https://www.epa.gov/so2-pollution/sulfur-dioxide-basics (last access: April 2018), 2018.

Vernier, J-P., T. D. Fairlie, J. J. Murray, A. Tupper, C. Trepte, D. Winker, Jacques Pelon et al. "An advanced system to monitor the 3D structure of diffuse volcanic ash clouds." Journal of Applied Meteorology and Climatology 52, no. 9 (2013): 2125-2138.

Webley, P. W., T. Steensen, M. Stuefer, G. Grell, S. Freitas, and M. Pavolonis. "Analyzing the Eyjafjallajökull 2010 eruption using satellite remote sensing, lidar and WRF-Chem dispersion and tracking model." Journal of Geophysical Research: Atmospheres 117, no. D20 (2012).

Webster, H. N., D. J. Thomson, B. T. Johnson, I. P. C. Heard, K. Turnbull, F. Marenco, N. I. Kristiansen et al. "Operational prediction of ash concentrations in the distal volcanic cloud from the 2010 Eyjafjallajökull eruption." Journal of Geophysical Research: Atmospheres 117, no. D20 (2012).

Wilson, L., and G. P. L. Walker. "Explosive volcanic eruptions-VI. Ejecta dispersal in plinian eruptions: the control of eruption conditions and atmospheric properties." Geophysical Journal International 89, no. 2 (1987): 657-679.

Winker, David M., Mark A. Vaughan, Ali Omar, Yongxiang Hu, Kathleen A. Powell, Zhaoyan Liu, William H. Hunt, and Stuart A. Young. "Overview of the CALIPSO mission and CALIOP data processing algorithms." Journal of Atmospheric and Oceanic Technology 26, no. 11 (2009): 2310-2323.

Winker, D. M., Z. Liu, A. Omar, J. Tackett, and D. Fairlie. "CALIOP observations of the transport of ash from the Eyjafjallajökull volcano in April 2010." Journal of Geophysical Research: Atmospheres 117, no. D20 (2012).

Yang, Kai, Nickolay A. Krotkov, Arlin J. Krueger, Simon A. Carn, Pawan K. Bhartia, and Pieternel F. Levelt. "Retrieval of large volcanic SO_2 columns from the Aura Ozone Monitoring Instrument: Comparison and limitations." Journal of Geophysical Research: Atmospheres 112, no. D24 (2007).

Yang, Kai, Xiong Liu, Pawan K. Bhartia, Nickolay A. Krotkov, Simon A. Carn, Eric J. Hughes, Arlin J. Krueger, Robert JD Spurr, and Samuel G. Trahan. "Direct retrieval of sulfur dioxide amount and altitude from spaceborne hyperspectral UV measurements: Theory and application." Journal of Geophysical Research: Atmospheres 115, no. D2 (2010).

Yang, Kai, Russell R. Dickerson, Simon A. Carn, Cui Ge, and Jun Wang. "First observations of SO_2 from the satellite Suomi NPP OMPS: Widespread air pollution events over China." Geophysical Research Letters 40, no. 18 (2013): 4957-4962.

Yorks, J. E., M. J. McGill, S. P. Palm, D. L. Hlavka, P. A. Selmer, E. P. Nowottnick, M. A. Vaughan, S. D. Rodier, and W. D. Hart. "An overview of the CATS level 1 processing algorithms and data products." Geophysical Research Letters43, no. 9 (2016): 4632-4639.

Chapter 3: Forecasting Volcanic Ash dispersion in GEOS-5

3.1 Introduction

The April 14th, 2010 eruption of Iceland's Eyjafjallajökull volcano spewed hazardous ash clouds into that atmosphere leading to mass closure of commercial air space, and placing a public spotlight on volcanic ash as an aviation hazard. This eruption has been the focus of numerous studies modeling the transport of the ash and SO2 clouds [*Webster et al. 2012*, *Folch et al. 2012*, *Webley et al. 2012*, *Dacre et al. 2011*, *Lu et al. 2016*, *Matthias et al. 2012*] and observing their various properties [*Arason et al., 2011; Darce et al., 2011; Flentje et al., 2010; Emeis et al., 2011; Prata and Prata, 2012; Thomas and Prata, 2011; Webley et al., 2012; Winker et al., 2012*]. Having received so much scientific and public attention, this eruption serves as an ideal case study to evaluate the accuracy of newly developed models and observational analyses. In this chapter, I develop ash modeling capabilities within GEOS-5, and use the depth of modeling and observational studies of the Eyjafjallajökull eruption to evaluate the accuracy of the ash forecasts.

Barring the more obvious reason, the Eyjafjallajökull eruption is unique in that the plume top altitude was nearly continuously monitored at 5-minute intervals from a weather radar station located nearby the Keflavík International Airport. These radar observations provide a direct observation of the volcanic ash emission source terms required to initialized volcanic ash within transport models. Naturally, modeling studies of the Eyjafjallajökull eruption overwhelming use the radar observed plume top altitudes to initialize volcanic ash within their respective models.

Following the guidance of these studies, I also use the radar observations of the plume top altitude to initialize a baseline simulation of volcanic ash with GEOS-5. I denote this as the "baseline" simulations as it follows much of the conventions and assumptions used in other modeling studies. The results of the baseline simulations generally match the forecasted locations of volcanic ash that were produced by the London VAAC at the time of the eruption, as well as with simulations from other modeling studies.

UV satellite observations from the Ozone Monitoring Instrument (OMI) show the ash and SO_2 cloud's horizontal extent following the eruption of Eyjafjallajökull. The OMI observations notably disagree with the baseline ash simulations. In order to gain insights into the nature of this discrepancy, I used a backward trajectory analysis to estimate the ash emission source terms from the OMI observations and compare these results to the radar plume top observations. A set of revised emission source terms are constructed accounting for observations from both OMI and the Keflavík radar. Simulations of the volcanic ash transport are generated using the refined emission source terms and compared to the baseline simulations. The comparisons between the baseline and refined ash simulations are used to gain insights the possible limitations of the radar plume top observations.

3.2 Observations of the Eyjafjallajökull Eruption

In this study, I aim to construct ash simulations that are similar to what was observed by satellites. From the aviation impact perspective, I want to understand flight rerouting scenarios based on a simulation that is close to what was actually

observed. This will provide insight to the utility of flight rerouting applications in the wake of a volcanic eruption.

Given the impact of the eruption of Eyjafjallajökull on air traffic, there has been a lot of effort to publish satellite observations of the volcanic ash and SO_2 clouds that pose aviation hazards. Observations notable for this study primarily include those from geostationary SEVIRI [*Schmetz et al. , 2002, Prata and Prata, 2012; Webley et al. 2012; Thomas and Prata, 2011*], polar orbiting IASI [*Clerbaux et al., 2009, Carboni et al. 2012; Dacre et al. 2011; Thomas and Prata, 2011*], and space lidar CALIOP [*Hunt et al. 2009; Winker et al. 2012*].

Routinely processed imagery of volcanic SO_2 and ash clouds from multiple polar satellite observations can be found using the Support to Aviation Control Service website (SACS, http://sacs.aeronomie.be) [*Brenot et al., 2014*]. The SACS website contains an archive of SO_2 and ash observations from the Eyjafjallajökull eruption, which assist in understanding the observed path of the ash and SO_2 cloud from April 14th to April 17th.

3.2.1 Satellite Observations

The Ozone Monitoring Instrument (OMI) onboard the polar-orbiting NASA's EOS Aura satellite has been frequently used to monitor volcanic SO_2 clouds [*Carn et al 2009; Carn et al. 2015*]. OMI is a nadir looking wide field-of-view push-broom UV-VIS spectrometer [*Levelt et al., 2006*] that images a swath with a 2,600 km width, with 13km along-track sampling. The 2,600 km wide swatch is broken up into 60 "cross-track" pixels with smallest size at nadir (24 km x 13 km), while at the swath

edge the resolution is 128 km x 13 km. OMI measures the Earth radiance from reflected sunlight in the 270 nm - 500 nm wavelength range. OMI observations are used to derive ozone and other trace gases, including SO_2 vertical column density (VCD) maps in Dobson Units (1 DU= $2.69*10^{16}$ molecules SO_2 cm^{-2}) and Aerosol Index (AI). OMI SO_2 products have been generated using progressively more sensitive retrieval algorithms across the instrument's lifetime. Initially, the SO_2 products were derived using the Band-Residual Difference (BRD) algorithm [*Krotkov et al. 2006*], and then improved for large volcanic eruptions using the Linear Fit algorithm of [*Yang et al. 2007*]. The current archived OMI SO_2 data has been reprocessed using the most sensitive Principal Component Analysis (PCA) algorithm [*Li et al 2013; 2017*] to derive both volcanic and pollution SO_2. The Aerosol Index (AI), describes the ratio of the measured radiance to the radiance expected from molecular (Rayleigh-only) scattering atmosphere [*Torres et al., 1998*]. A positive AI indicates the presence of absorbing aerosols, such as dust and volcanic ash [*Seftor et al., 1997; Krotkov et al., 1999a, 1999b*], whereas near-zero AI indicates large non-absorbing aerosol particles or no aerosols at all [*Torres et al. 2007*].

Beginning in June 2007, OMI observations begin detecting anomalous observations along the central (near nadir) positions of the OMI swath (see http://projects.knmi.nl/omi/research/product/rowanomaly-background.php). As a result, portions of the OMI's central swath must be filtered out.

The Infrared Atmospheric Sounding Interferometer (IASI) has also been a valuable tool in monitoring volcanic ash [*Clarisse et al., 2010*] and SO_2 clouds [*Carboni et al., 2012*]. IASI, onboard the polar orbiting MetOp-A and -B

meteorological satellites measures volcanic ash and SO_2 in the Thermal infrared (IR), twice daily [*Clerbaux et al., 2009*]. The volcanic ash observations are sensitive to ash particles with a diameter between 2 to 32 μm [*Stohl et al., 2011*]. Although I do not directly present any IASI observations here, I do make reference to their observations published elsewhere.

3.2.2 Radar Observations

The evolution of the ash plume-top for the Eyjafjallajökull eruption was monitored from the ground by C-band radar at an Icelandic weather radar station, just north of Keflavík International Airport. This radar station is situated approximately 155 km away from Eyjafjallajökull and has been previously used to monitor volcanic eruptions, including the eruptions of Hekla in 2000 [*Lacasse et al., 2004*] and Grímsvötn in 2004 [*Vogfjörd et al., 2005*]. A detailed description of the radar observations of the Eyjafjallajökull plume top is found in Arason et al. [*2011*]. The radar scans both horizontally and at increasing inclination angle, measuring the reflectivity of the atmospheric column containing the volcanic ash plume. For the eruption of Eyjafjallajökull, the radar was used to measure the echo top of the volcanic plume, i.e. the volcanic plume max altitude. The echo top defines the maximum altitude where the reflectivity exceeded a threshold value. Radar observations of ash are generally more sensitive to coarse ash. For example, the Volcanic Ash Radar Retrieval (VAAR) of Marzano et al. [*2011*] noted a sensitivity of their retrieval to coarse ash, of 64 microns or greater.

This radar station produced observations of the volcanic plume-top altitudes at 5 minute intervals form April 14th to May 23rd. The observations are also provided in hourly and 6-hour averages. The radar station was set to measure altitudes between 0 to 12 km, but due to obscuration from the Brennisteinsfjöll mountain range the radar had a minimum altitude sensitivity of 2.5 km.

3.3 Modeling Volcanic Eruptions in GEOS-5

3.3.1 GEOS-5 Model

This work uses NASA's state of the art global Eulerian Goddard Earth Observing System, version 5 (GEOS-5) [*Suarez et al., 2008*] Earth System model, which includes atmospheric circulation and composition, as well as land and ocean characterization. The GEOS-5 model has 72 vertical layers and can be run in both fine and coarse horizontal resolutions, in the following modes: forecast mode, data assimilation mode, or replay mode. In forecast mode, the model is initialized with meteorology fields and further dynamics are computed, or forecasted, from these initial conditions. Data assimilation is similar to the forecast mode, but includes a data assimilation analysis step to evaluate and correct the state of the model meteorology. In replay mode, the model meteorology is updated at temporal intervals using archived meteorology.

The GEOS-5 model is capable of adjusting the meteorological fields based on the radiative properties of simulated aerosols, referred as running in "online" mode. When GEOS-5 is run online the optical properties of aerosols are used to

compute the effects of radiative heating affecting the simulation meteorology during the model run. In the "offline" mode, the aerosols act like passive tracers since they do not affect the meteorological fields. The advantage of running GEOS-5 online is that it should yield a more realistic representation of aerosol transport.

It is important to note, however, that the aerosol effects of GEOS-5 online run can be nullified by running the model in replay mode. Running GEOS-5 in replay mode is desirable since it continually updates the simulation meteorology with an accurate archived meteorology. However, periodically updating the simulation meteorology with archived meteorology would overwrite the aerosol effects on meteorological fields. This could be avoided by running my simulations under settings that maximize accuracy in the meteorology (high resolution, online, active data assimilation, etc.), but this would be very computationally demanding. Since the observed ash loadings are not extremely large, compared to other larger volcanic eruptions, I choose to run GEOS-5 in replay mode in order to represent accurate meteorology, and neglect the aerosol feedbacks on dynamics.

The GEOS-5 simulations presented in this work were run on a cube-sphere grid at c180 horizontal resolution (~ 0.5^{o} x 0.5^{o}). The initial meteorological conditions come from the MERRA analysis, regridded to the c180 resolution.

3.3.2 GOCART Ash Model

Aerosols are modeled in GEOS-5 using the internal online Goddard Chemistry, Aerosol, Radiation, and Transport (GOCART) module [*Chin et al., 2000; Colarco et al., 2010*]. GOCART is equipped to model dust, black carbon, organic

carbon, sea salt, and sulfate aerosols. Species in GOCART are transported by advection, convection, and turbulent mixing. Advection of tracers in GEOS-5 is computed by a flux-form semi-Lagrangian method [*Lin and Rood, 1996*], and archived cloud mass flux fields are used to parameterize the moist convection. Turbulent mixing due to buoyancy and mechanical shear is approximated by eddy diffusion.

GOCART simulates dust through a sectional approach, allowing for different density and size distributions to be simulated. Dust is removed from the atmosphere through gravitational settling and wet and dry deposition. The GOCART dust module [*Ginoux et al. 2001*] has been modified to simulate multiple instances of dust-like particles in the atmosphere. In this research, the dust model is used to model the dispersion of volcanic ash clouds. When the dust module is used to simulate volcanic ash, all the dust emission sources are shut-off and only predefined ash emission sources are retained. Volcanic ash, like dust, is removed from the model atmosphere by wet removal, dry deposition, sedimentation, and convective scavenging, see Chin et al. [*2002*]. The dry deposition of ash is modeled as both gravitational settling and the turbulent transfer of particles to the surface. Wet scavenging is modeled as removal from below cloud precipitation (washout) and from in-cloud precipitation (rainout). Due to a lack of better information, Ginoux et al. [*2001*] assumed the scavenging efficiency of wet removal process for dust was the same as that used for sulfates. I also make this assumption for the volcanic ash simulations.

Volcanic ash is initialized in the model by emitting a mass flux of ash directly into the grid box that corresponds to the prescribed emission latitude, longitude, and altitude. The ash plume's top and bottom altitudes are used to vertically distribute the ash flux across the grid boxes that overlap this altitude range. The shape of the ash plume is currently assumed to be a constant from the top to the bottom, i.e. the ash flux is equally distributed across this range. The horizontal location of the ash emissions is defined as the grid column that encapsulates the prescribed emissions latitude and longitude location. The duration of the ash mass flux emission is defined by a start and stop time.

3.4 Modeling the 2010 Eruption of Eyjafjallajökull: Baseline Simulation

3.4.1 Ash Particle Size Distribution

The ash particle size distribution used in the GOCART simulations were chosen based on *in situ* observations of the ash particle size distributions and the sensitivity range of satellite Thermal IR observations (IASI and SEVIRI) to volcanic ash.

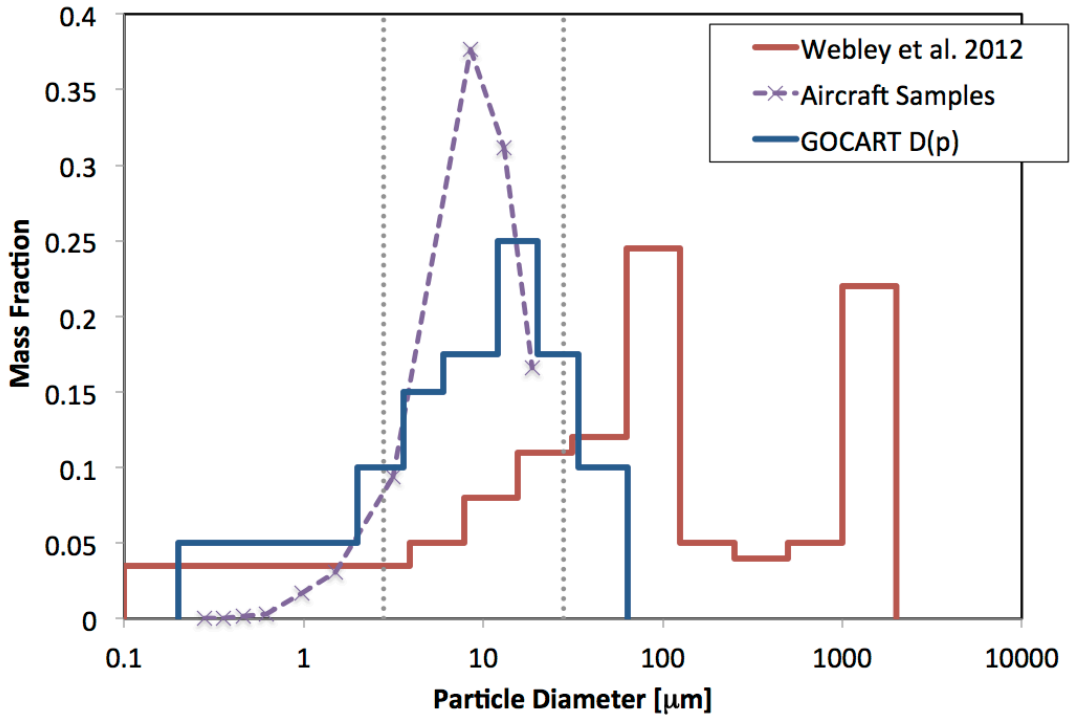

Figure 3.3 Ash particle size distributions (PSD) from models and observations. The solid red line shows the distribution used in Webley et al. 2012, representing a distribution typically assumed for an eruption of this type. The dashed line shows the aircraft measured *in situ* ash particle size distribution from Schumann et al. 2011, observed at ~15:00 UTC on May 2nd 2010 approximately 450km downwind of Eyjafjallajökull volcano. The vertical dotted lines represent the range of TIR (IASI and SEVIRI) ash retrieval sensitivity. Blue solid line is PSD assumed in this work.

Figure 3.3 shows the particle size distribution (PSD) of ash samples from Schumann et al. 2011, representing *in situ* aircraft measurements of the ash cloud. The aircraft measurement shown in Figure 3.3 show a peak particle diameter ~9 μm. These aircraft observations were used to construct the ash size distribution used in Stohl et al.'s [*2011*] simulations. Also noted in Figure 3.3 is the sensitivity range of IASI and SEVIRI observations, primarily for ash particles diameters between 2 - 32 μm. Based on aircraft observations of Schumann et al. [*2011*] and the sensitivity of IASI observations, I chose a particle size distribution that peaks at 16 μm. Since this study

is primarily interested in modeling the ash cloud transport compared with satellite observations, I chose to only model the fine ash particles. Simulations by Webley et al. [*2012*] found that when the ash cloud had travelled hundreds of kilometers from the volcano, it was best represented by particle bins with a diameter of 62.5 μm or smaller. Gravitational settling causes heavier ash particle bins to settle out much closer to the volcano. Based on this result, I chose to only simulate ash particles with radii smaller then approximately 32 μm. The ash is simulated for 7 size bins, with parameters as shown in Table 3.1. My model simulations also assume a constant ash mass density of 2,700 kg/m^3.

Table 3.1 GEOS-5 Ash Size Bins

Bin Number		**1**	**2**	**3**	**4**	**5**	**6**	**7**
Effective Radius	[μm]	0.55	1.4	2.4	4.5	8	13.5	24.5
Lower Bound (radius)	[μm]	0.1	1	1.8	3	6	10	17
Upper Bound (radius)	[μm]	1	1.8	3	6	10	17	32

3.4.2 Ash Emission Source Terms: Altitude and Flux

The volcanic ash plume top observations from the weather radar at Keflavík airport [*Arason et al., 2011*] have been used by numerous studies to provide initial source terms for Eyjafjallajökull ash emissions [*Webster et al. 2012, Folch et al. 2012, Webley et al. 2012, Dacre et al. 2011, Lu et al. 2016, Matthias et al. 2012*]. In this study, the hourly averaged plume top radar observations are used to initialize the plume top in the GOCART model simulations. The hourly plume top observations are

an average over the 5-minute plume top observations, which are not always provided. Thus, the hourly plume top observations are discarded if more than 80% of the 5-minute observations are not valid. More information about the frequency of missing scans can be found in Arason et al. [*2011*].

As the plume top only describes the maximum altitude of the volcanic plume, the vertical structure of the volcanic plume must be assumed. In this study, the volcanic ash is assumed to be uniformly distributed across the top third of the atmospheric column between volcanic summit elevation and the observed plume top. For example, an 8km plume top will have a 2.1km depth. This assumption for the vertical structure of volcanic plumes is typically used in GEOS-5, including the recent MERRA-2 Reanalysis [*Randles et al., 2017, Buchard et al. 2017*]. A typical umbrella cloud plume shape, as used in Webley et al. 2012, breaks up the plume into an umbrella region just below the plume top altitude, with a tapered off cloud tail attaching the umbrella region to the volcano vent. The depth of the umbrella region is defined as the top quarter of the atmospheric column between the plume top and the volcanic summit, and contains 75% of the total ash. For large eruptions that inject ash at 20 km – 30 km, the difference between our simplified 1/3 top column plume shape and the umbrella cloud plume shape may be significantly larger. However, the plume top altitudes used in this study are roughly between 8-4km and the model's vertical resolution is roughly 1 km in this altitude region, so our assumed plume shape is approximately similar to simulating only the umbrella region of a typical umbrella cloud plume shape.

Numerous studies have demonstrated an empirical relationship between the plume top altitude of a volcanic plume and the mass emission rate, or MER, of erupted tephra. Mastin et al. [*2009*] provides a thorough summary and analysis of this relationship. Following similar studies of the Eyjafjallajökull eruption, [*Folch et al. 2012, Webley et al. 2012, Dacre et al. 2011*] and many others noted previously, I use this relationship to estimate an ash mass flux from the radar plume top observations. In this study I use the relationship from Mastin et al. [*2009*] (see Equation 1).

The MER represents the total mass of tephra ejected from the volcano. In this study, I was primarily interested in modeling the fraction of fine ash that survived past initial aggregation process and gravitational settling to be advected hundreds of kilometers away from the volcano. The fraction of the downwind advected fine ash from the total erupted ash mass as described by the MER-height relationship (E 2.6) is unclear. Following Webley et al. [*2012*], I initially assume 40% of the total mass for particles with a diameter less than or equal to 63 μm. This assumption comes from the study of Mastin et al. [*2009*], which catalogued volcanic eruption styles and typical source term parameters.

3.5 Initial Model Results and Analysis

In this section the results from the GOCART ash simulations using the baseline emissions are presented and compared to other reports and observations. First, a general description of the simulated ash transport is given. This is followed by a comparison of the ash simulations to the VAAC reports, to see how my simulations

compare to the real-time estimates of the ash cloud. Then, the ash simulations are compared to observations of the ash and SO_2 cloud from the satellite instrument (Aura/OMI). I further note how my simulations compare to other published simulations that have done similar work, as well as other published observations.

3.5.1 Simulation Results

Strong westerly and northwesterly winds persisted across Iceland at lower and upper altitudes (3 -10km) at the beginning of the eruption on April 14th and 15, with strong westerly winds persisting for subsequent days at upper altitudes [*Petersen, 2010*]. In Figure 3.4, plots of the column integrated ash mass, or ash loading, from my GOCART simulation are shown. The GOCART simulations show the ash clouds transported by westerly winds, as the ash cloud is quickly advected towards continental Europe on April 14th and 15th. On April 15th, the simulations show the leading edge of the ash cloud undergoing a rapid meridional shearing, dispersing ash from the UK and up to the northern most regions of Scandinavia, with western part of the ash cloud trailing back to the volcano. The meridional shearing is likely caused by entrainment of the ash cloud into an anticyclone directly south of Iceland [*Petersen, 2010*]. By April 16th 00:00 UTC, the leading edge of the ash cloud has stretched into a filament-like structure moving to the south-east across continental Europe. The western part from the ash cloud that trailed back to the volcano on April 15th merges into the leading ash cloud on April 16th, resulting in a single large ash cloud stretching across much of Europe. The ash simulation 2D snapshots at different times in Figure 3.4 also show that the leading filament structure is part of the

volcanic cloud initialized during the initial explosive phase of the eruption, at ~9km; the trailing part of the cloud came from the emissions at lower altitudes, at ~5km. The emissions ceased after 12:00 UTC on April 15th but started up again on April 16th.

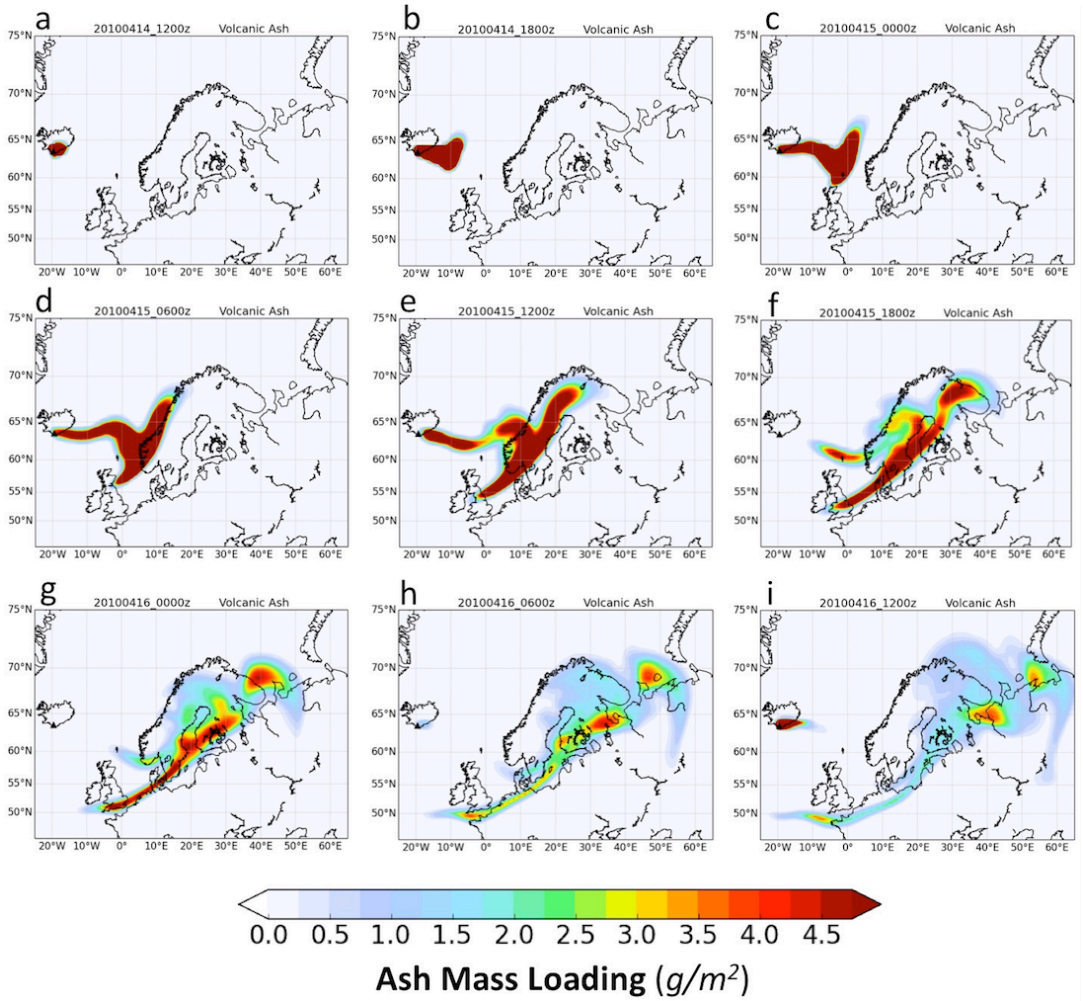

Figure 3.4 The Eyjafjallajökull ash cloud from the GOCART baseline simulations. The column ash loading is shown, starting on April 14th at 12:00 UTC (a). The snapshots of the ash simulation are shown at 6-hour intervals (b) – (i), through April 16 at 12:00 UTC (i).

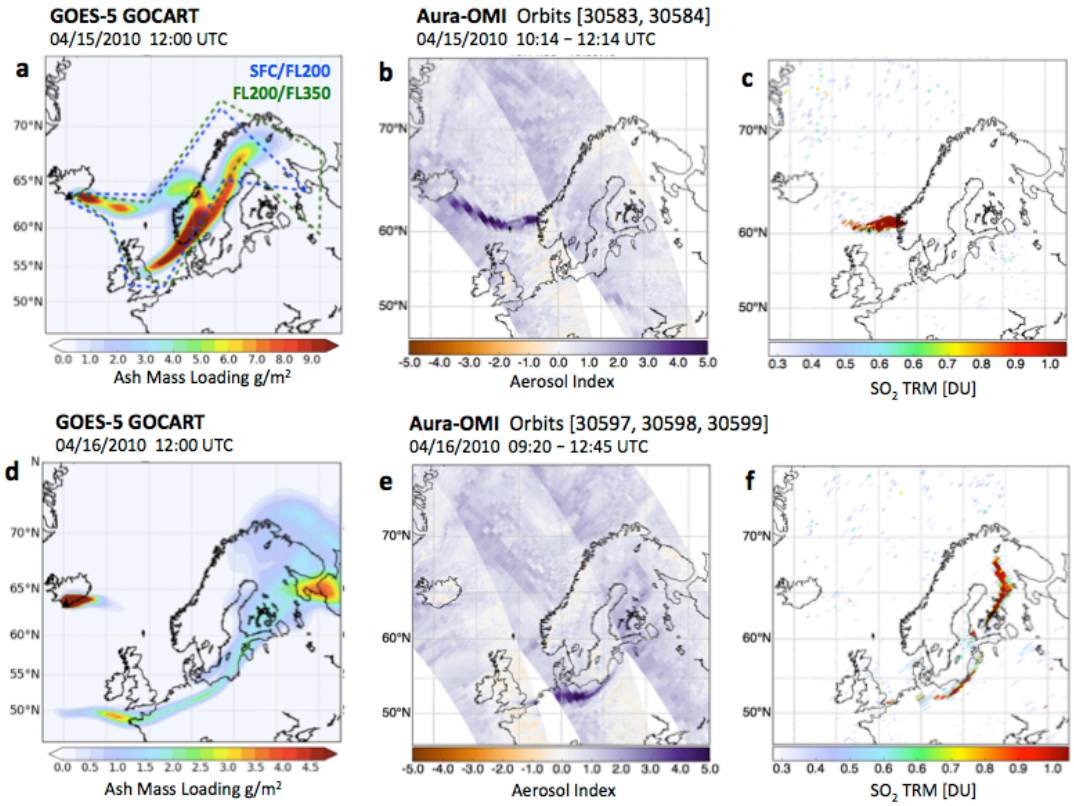

Figure 3.5 Comparison of the GEOS-5 baseline ash simulation to VAAC Reports (dash lines in a) and OMI Observations. The total column ash loading from the baseline simulations are shown in (a) and (d), for April 15th 12:00 UTC and April 16th 12:00 UTC respectively. The London VAAC VAA regions for the Surface-to-FL200 (dashed blue) and FL200-to-FL350 (dashed green) are shown in (a). The OMI AI and SO_2 composite observations for April 15th 10:14 – 12:14 UTC are shown in (b) and (c), and for April 16th 09:20-12:45 UTC in (e) and (f).

The VAAC produces Volcanic Ash Advisories (VAAs) that estimate the extent of volcanic ash in the atmosphere both vertically and horizontally. VAAs contain estimates of ash-contaminated regions for the current state of the atmosphere and forecasts at +6h, +12h and +18h. In Figure 3.5a, the VAAs estimating ash-contamination for the current state of the atmosphere, for SFC/FL200 and FL200/FL350, on April 15th at 12:00 UTC are overlaid on the corresponding ash simulation. The two different dashed regions represent two volumes of ash

containing air masses, constrained by a bottom/top vertical levels. VAAs use flight level as a vertical coordinate, where flight level is expressed as hundreds of feet and assumes a standard pressure. For example, SFC, FL200, FL350 correspond the surface, 20,000 ft (~ 6 km) and 35,000 ft (~ 10.7km). However, flight level assumes a standard pressure so these altitudes, while roughly similar, may not exactly reflect the true altitude or the altitude modeled in my simulations. The London VAAC also issued a VAA for FL350/FL550 on April 15th at 12:00 UTC, but they are not included here since none of the ash in my simulations were initialized at, or above, 10km.

In general, the baseline ash simulation tends to overlap with the corresponding VAAC VAAs for April 15th at 12:00 UTC. I can also see that the VAAC VAA tends to encompass a much larger area then seen in the simulations, though this should be expected with a zero-ash tolerance policy, since VAAs estimate air mass regions conservatively where any ash exposure is expected. The main point of this comparison is to demonstrate that my simulation agrees reasonably well with VAAC VAA estimates from the initial time of the eruption.

Also presented in Figure 3.5 are composite OMI swath observations of the volcanic ash and SO_2 clouds observed at ~2pm local time on April 15th and 16th. Note that here the UV Absorbing Aerosol Index (or simply, AI) is used to indicate the presence of volcanic ash. The OMI observations are blocked in the middle regions of the swath, so we've only plotted cross-track positions 1 through 27. Although this selection removes a significant part of the OMI orbit, the remaining observations still yield reasonable coverage of the ash and SO_2 clouds. The OMI observed location of the ash and SO_2 clouds agrees with observations from

other satellite instruments, such as GOME-2 [*Thomas and Prata, 2011*], SEVIRI [*Prata and Prata, 2012; Thomas and Prata, 2011*], and IASI [*Darce et al. 2011*]. The OMI observations show that the horizontal extent of the ash and SO_2 clouds generally overlap. Other studies have similarly noted the strong correlation between the horizontal extent of ash and SO_2 in the Eyjafjallajökull volcanic cloud [*Thomas and Prata, 2011*]. The correlation of the spatial extent is particularly better on April 16th then on April 15th, though, the mass distributions of ash and SO_2 across the cloud are not well correlated [*Thomas and Prata, 2011*].

The baseline simulation greatly overestimates the horizontal extent of the ash cloud, when compared to the OMI observed ash cloud locations. On April 15th, the simulations show an ash cloud extending over a large part of the Scandinavia and extending down to the UK, and tracing back to the volcano. The OMI observations show a much smaller ash cloud just barely reaching the coast of Norway, in agreement with SEVIRI observations [*Prata and Prata, 2012*]. On April 16th, the baseline ash cloud has dispersed and spread to cover a much larger geographic area. Part of the ash cloud sheared into a filament-like structure that stretches across much of Europe. In OMI AI observations, the ash cloud is mainly over central Europe, with smaller amounts further to the northeast, over Finland. SO_2 is observed covering the same region, but with a stronger signal in the northeastern part of the cloud. The baseline simulation generally overlaps with the OMI observations, but as shown on the 15th, greatly overestimates the extent of the volcanic ash cloud.

Looking at this comparison from the perspective of the OMI observations, I do see an overlap with the simulations. On April 15th, the leading edge of the

observed ash cloud is shifted south of the simulated ash clouds, thought the trailing part of the observed ash cloud that traces back to the volcano matches better with the simulated ash cloud. On April 16th, the observed sheared ash clouds tend to overlap better with the simulated ash cloud.

The results from the baseline ash simulations generally agree with results obtained by other studies that use the Keflavík radar plume top to initialize the Eyjafjallajökull volcanic ash cloud [*Webley et al. 2012, Folch et al. 2012; Darce et al. 2011*]. Though the simulations from these studies are not identical, they greatly overestimate the ash cloud's spatial extent on April 15th and 16th, when compared to satellite observations. Observations from IASI [*Darce et al. 2011*], suggest that volcanic ash was not advected away from Iceland until ~22:00UTC. This contradicts the source terms used in my simulations, assuming emission start time at 12:00 UTC (Figure 3.5a). In the next section I further investigate the impact of this time difference on ash advection and construct a modified source term that's used to run a revised ash simulation. These simulations are compared to the baseline simulation results from this section.

3.6 Revised Model Setup

An analysis of the baseline simulation suggests that the earlier timing of the ash emission source term is responsible for the overestimation of the dispersed ash cloud's spatial extent. In order to constrain the fine ash emission source timing to better agree with the observed dispersion pattern of the fine ash cloud, I will use a backward trajectory method [*Krotkov et al., 2010; Hughes et al. 2012*] and compare the results to the reported local radar emissions. The results of the back-trajectory analysis will be used to construct a revised emission source term that will be used to run a revised ash simulation. We'll compare the results of the revised simulation with those from the baseline and satellite observations.

3.6.1 Trajectory Analysis of Observations

Trajectories have frequently been used to analyze volcanic clouds, typically to deduce the altitude of emissions [*Schoeberl et al. 1993; Allen et al. 1999; Prata and Bernardo, 2007; Krotkov et al. 2010; Yang et al. 2010; Hughes et al. 2012; Hughes et al. 2016*]. Since we're interested in estimating both the height and the timing of volcanic emissions, I follow the methodology outlined in Hughes et al. [*2012*], where backward trajectories are used to resolve an emission height-time probability distribution function (PDF).

As previously described in Section 2.4.1, Hughes et al. [*2012*] initialized vertical stacks of trajectories at satellite total column measurements of volcanic SO_2 and drove the trajectories backwards in time (back-trajectories). Trajectories that travelled back to their known origin, the volcano, at any time are considered to have

successfully described potential SO_2 transport paths that lead to SO_2 observations and were combined in a trajectory ensemble. The trajectory ensemble were then be used to derive the SO_2 emission time PDF, the SO_2 emission altitude PDF [*Hughes et al. 2016*], or the joint PDF that describes the emission altitude as a function of time [*Hughes et al. 2012*].

Here I apply a back-trajectory analysis to OMI observations of SO_2 from Eyjafjallajökull volcanic cloud. As described in Hughes et al. [*2012*], initializing back trajectories from observations too close to their source can lead to trajectory ensembles that contain nearly all the initialized trajectories, which can yield meaningless or misleading PDFs. For this reason, I apply a back-trajectory analysis to OMI SO_2 observations from April 16th, shown in Figure 3.5, for all satellite SO_2 observations above a 0.25 DU noise threshold. The trajectories were run backward using the Goddard Space Flight Center Trajectory Model [*Schoeberl and Sparling, 1995*] driven by NCEP Operational 1^ox 1^o re-analysis [*Kalnay et al. 1996*]. Trajectories were initialized at the time of OMI observation on April 16 at ~2pm local time at 1 km intervals at altitudes ranging from 2 to 20 km. Trajectories that approach to within 50km of the volcano are added to the trajectory ensemble. The ensemble is used to derive the PDF of trajectory arrival times, at the volcano. Since the trajectories are not undergoing irreversible processes, the arrival time can also be described as the emission time from the volcano. I define the PDF of the emission times as, P(t*).

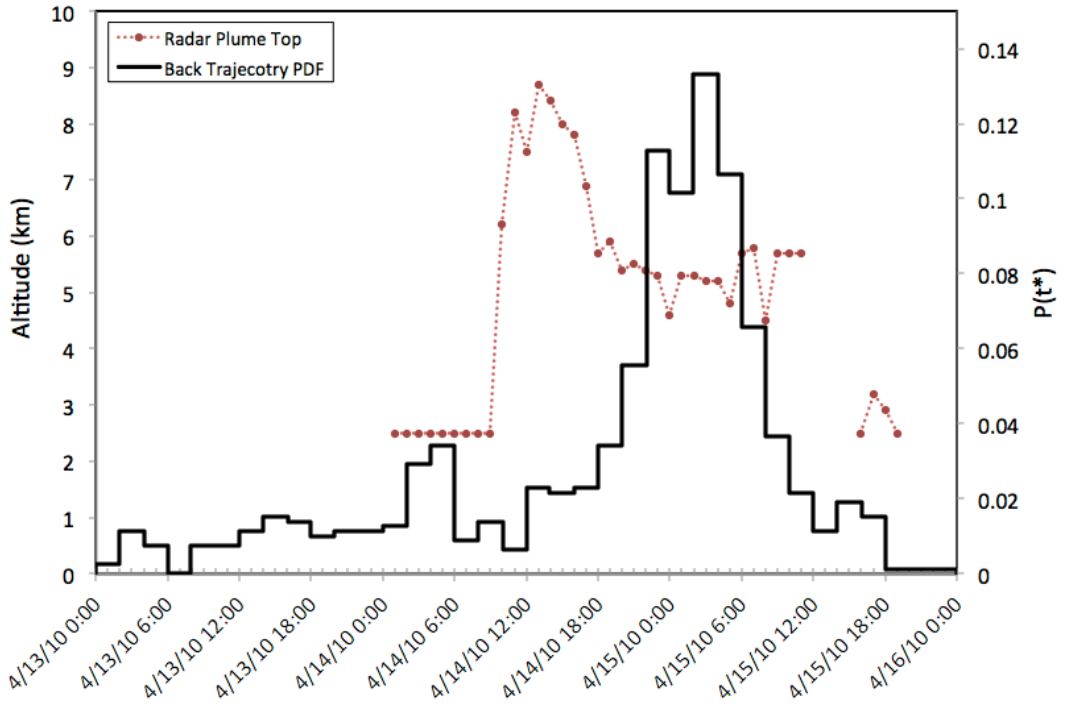

Figure 3.6 Emission time PDF defined by back trajectories from OMI volcanic SO_2 observations on April 16. The emission time PDF, P(t*), is plotted as a solid black line. The radar plume top observations for this time period are also shown, in red dots. The gap in the radar observations represents times that radar observations weren't reported.

P(t*) for the OMI SO_2 observations from April 16th are shown in Figure 3.6. P(t*) shows a well constrained Gaussian-like distribution of emission times with a most probable time around 2:00 UTC on April 15th and possible times range from ~21:00 UTC on April 14th until 08:00 UTC on April 15th. This result suggests that the observed SO_2 cloud was emitted and subsequently advected away from the volcano over the extended time period: April 14th 21:00 UTC - April 15th 08:00 UTC. The emission start time estimated from the emission time PDF agrees with IASI observations that show ash emission beginning to advect away from Iceland just before 22:00 UTC on April 14th [*Darce et al. 2011*].

Also plotted in Figure 3.6 are the radar hourly averaged height observations of the volcanic plume. Comparing P(t*) to the radar observations, I can see that the P(t*) peak overlaps with the period of the eruption, but is delayed until after the initial explosive phase. P(t*) also suggests that the bulk of SO_2 was emitted during the later less explosive phase of the eruption, and at lower altitudes ~5km - 6km.

Although P(t*) was estimated using OMI SO_2 observations, these results should also bear true for the emitted fine ash cloud given its collocation with the SO_2 cloud. Having collocated spatial patterns means that very similar wind fields advected the SO_2 and ash clouds. In this case, the colocation of ash and SO_2 clouds on April 15th and 16th requires that they have the similar emission times and altitudes. That said, the trailing part of the ash cloud on April 15th doesn't overlap SO_2 observations, so P(t*) is likely underestimating the stop time of the ash emissions at 08:00 UTC on April 15th. With this in mind, I only use P(t*) to estimate the ash emissions start time.

3.6.2 Revised Emission Duration

Using the emission time PDF, P(t*), as guidance, a revised ash emission vertical profile is constructed. Both my estimate P(t*) and IASI observations suggest that ash didn't start advecting away from the volcano until roughly 21:00 UTC, so for the revised emission I truncate the baseline ash flux emission at 21:00 UTC on April 14th. The revised ash flux is set to zero at all times before 21:00 UTC on April 14th. Radar observations showed that the eruption experienced a more explosive phase with the highest emission altitudes during the first 9 hours of activity, before 21:00 UTC on April 14th. My construction of the revised ash flux currently has the effect of

removing ash emissions from the more explosive portion of the eruption, keeping emission altitudes below 6km. This is partially in conflict with CALIOP observations from April 16th, which measured the ash cloud over west Germany at altitudes as high as 7.27 km [*Winker et al. 2012*]. It should also be noted that the 5-minute radar plume top observations did have a maximum value at 9.1 km during the 19:00 to 20:00 UTC hourly interval, though the average height was 5.9 km (Fig. 3.4). For these reasons, I chose to adjust the injection height to a higher altitude than what was observed by radar. The ash altitude in the revised emissions is initially set to 7.8 km, the average of the higher altitudes observed during the initial explosive phase of the eruption on April 14th during 10:00 - 17:00 UTC. For April 14th 22:00 UTC, and going forward, the ash emissions are assumed to follow the emissions observed by radar. A comparison of the baseline and revised emission altitudes is shown in Figure 3.7.

The ash flux for the revised emissions is derived using the same MER-altitude relationship used to derive the baseline ash flux emissions.

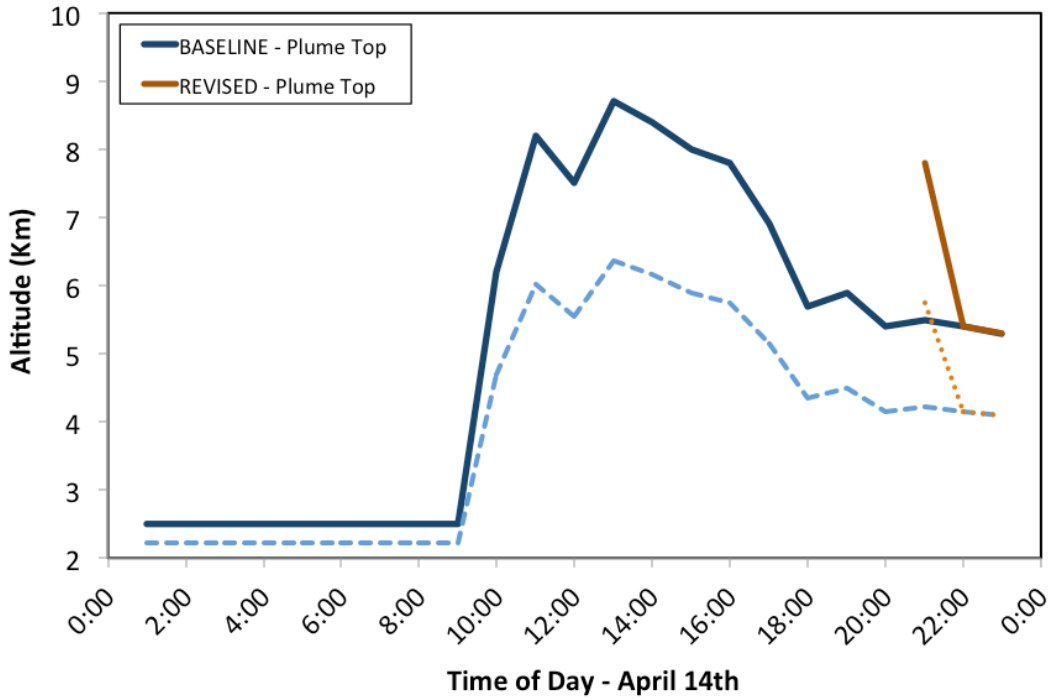

Figure 3.7 Initialized plume tops (solid lines) and bottoms (dashed lines) for the baseline (blue) and revised (orange) ash simulation.

3.7 Modeling Results: Baseline vs. Revised

In this section, the effects of modifying the emission source parameters in the revised ash simulation are compared with the baseline simulation and OMI observations. The vertical distributions of the baseline and revised simulations are also described. This is followed by analysis of the volcanic ash cloud that advected across central Europe, where timing and vertical distribution of the ash cloud was well observed by ceilometers and lidars.

3.7.1 April 15th, 2010

Altering the ash emissions in the revised simulation results in the removal of a significant portion of the ash cloud from the simulation. This can be seen in Figure 3.8 (a and b), where the simulated ash cloud on April 15th at 12:00 UTC is shown. In the baseline simulation, the anticyclone to the south of Iceland sheared the leading edge of the ash cloud. The revised simulation delays the ash emission start time, yielding a leading edge that experiences less meridional shearing and with less overall ash mass. As noted previously, the baseline simulation matches reasonably well with the VAAC VAA, but the leading edge drastically overestimates the horizontal extent of the ash cloud when compared to OMI observations. The revised simulation decreases the extent of the ash cloud within the VAA, coming into a better agreement with the OMI observations.

In order to better understand the vertical structure of the ash clouds in the GCOART simulations, the plume top of the simulations is computed and shown in Fig 3.6. For these figures, the plume top is defined as the height of a column that contains 90% of the total column ash.

Figure 3.8 shows the plume top of the simulated ash clouds on April 15th. In the baseline run, the leading edge of the ash cloud varies in altitude, with the southernmost part at 5 km and gradually increasing in altitude to 9 km at the northern edge. The leading edge of the ash cloud in the revised run is opposite to this, with the southern edge at a higher altitude (7km - 8km), with the northern edge at lower altitudes (6km - 7 km). This difference demonstrates that the change in the emission source terms primarily affected the structure of the leading edge of the ash cloud,

which didn't match OMI observations. The trailing edge of the ash cloud in both simulations is identically around 4 km - 6 km, showing that it was emitted at times when the baseline and revised simulations had the same emission source terms.

There are still places of notable disagreement between the revised simulation and the OMI observations, primarily at the leading edge of the cloud. The OMI observations place the leading edge of the cloud slightly further south than seen in the revised simulations, and only extending to the coast of Scandinavia. The revised simulation pushes the leading part of the ash cloud further inland, and shears southward. The revised ash simulation appears to hook around the region were OMI observed the leading ash cloud. The reason for the remaining disagreement between the ash simulations and OMI observations is unclear. A series of alternative ash simulations were generated by nudging the revised emission source terms along the time and altitude dimensions. None of these alternative ash simulations resulted in increased agreement between the ash simulations and OMI. However, the differences between the ash simulations and OMI observations did reduce when the resolution of the GEOS-5 simulations and MERRA initial meteorological conditions become more coarse, as see more coarse the c48 GEOS-5 simulations (~ 2^{o}x2^{o}), see Appendix Figure A.1. Our results here are similar to a comparison of the results of Webley et al. [*2012*] which ran ash simulations at a high resolution (18km) and Folch et al. [*2012*] which used a coarse resolution (1.5^{o}x1.5^{o}). Both of those studies used the radar observations to derive ash emission source terms. For this reason, I hypothesize that the disagreement between the OMI observations and ash simulations are the results of errors in the meteorology, which become "averaged-over" at coarser

meteorological resolutions.

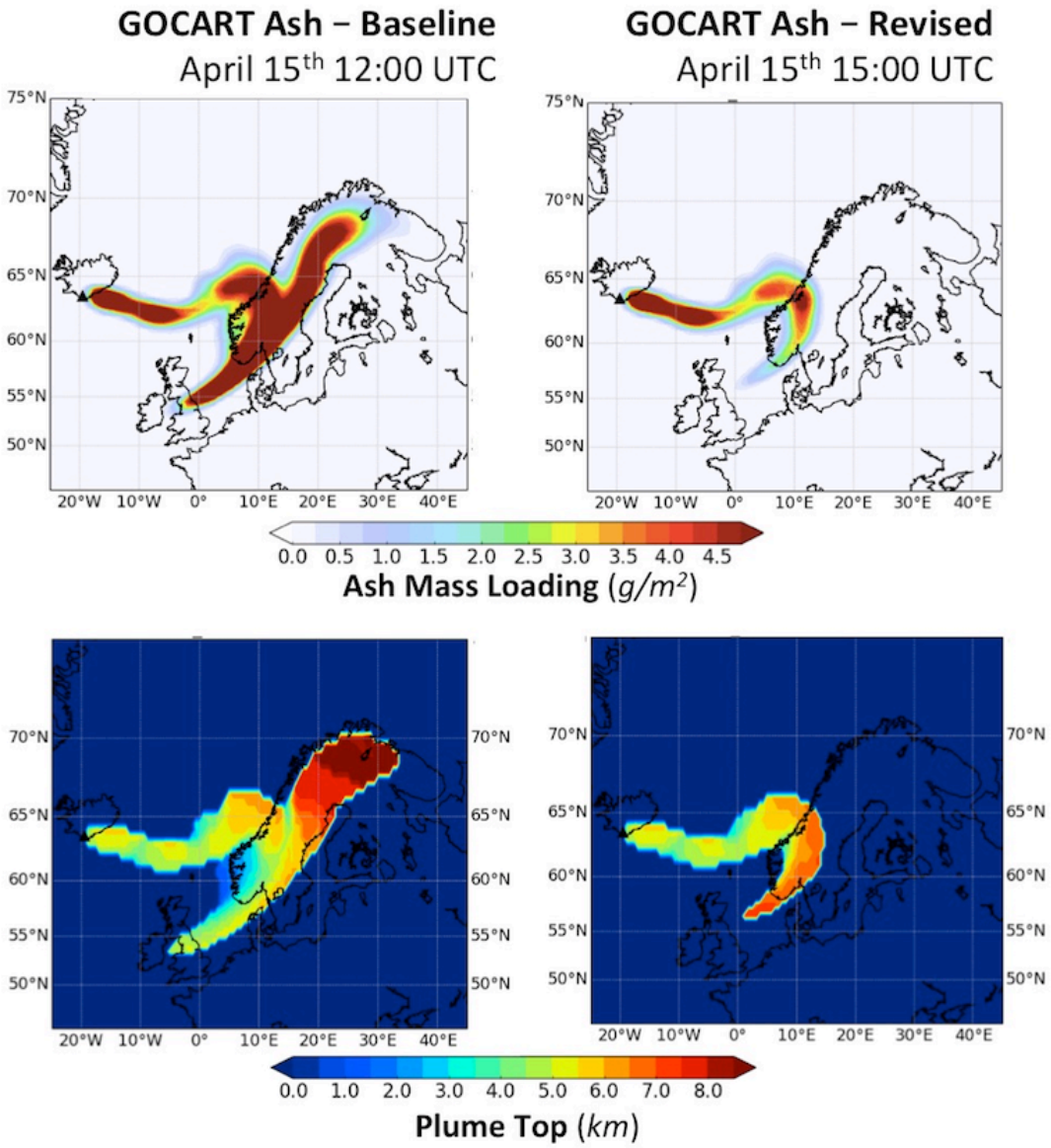

Figure 3.8 Comparisons of baseline and revised ash simulations for April 15th, 2010. The left panels show the ash mass loading (top) and plume top (bottom) for the baseline simulations on April 15th at 12:00 UTC. The same is shown for the revised simulations in the right panels.

3.7.2 April 16th, 2010

In general, there is a large difference in ash mass loading between the baseline and revised simulations that is apparent on the April 16th plots, Figure 3.9 (a) and (b). This is to be expected since the MER-Height relationship approximates larger ash fluxes with higher altitudes, so by removing the higher plume tops from the volcanic ash emission source term, there has also been a significant total ash mass reduction in the revised run. The difference between the ash mass spatial distributions on April 16th show that the emission source term from 09:00 UTC to 21:00 UTC greatly influenced the distribution of ash on April 16th. In the baseline simulation, the ash mass is distributed rather uniformly across the ash cloud, whereas the revised ash cloud has two distinct peaks in the ash cloud concentrations. The peaks in ash mass in the revised simulations do occur at locations near where ash was observed in the OMI observations.

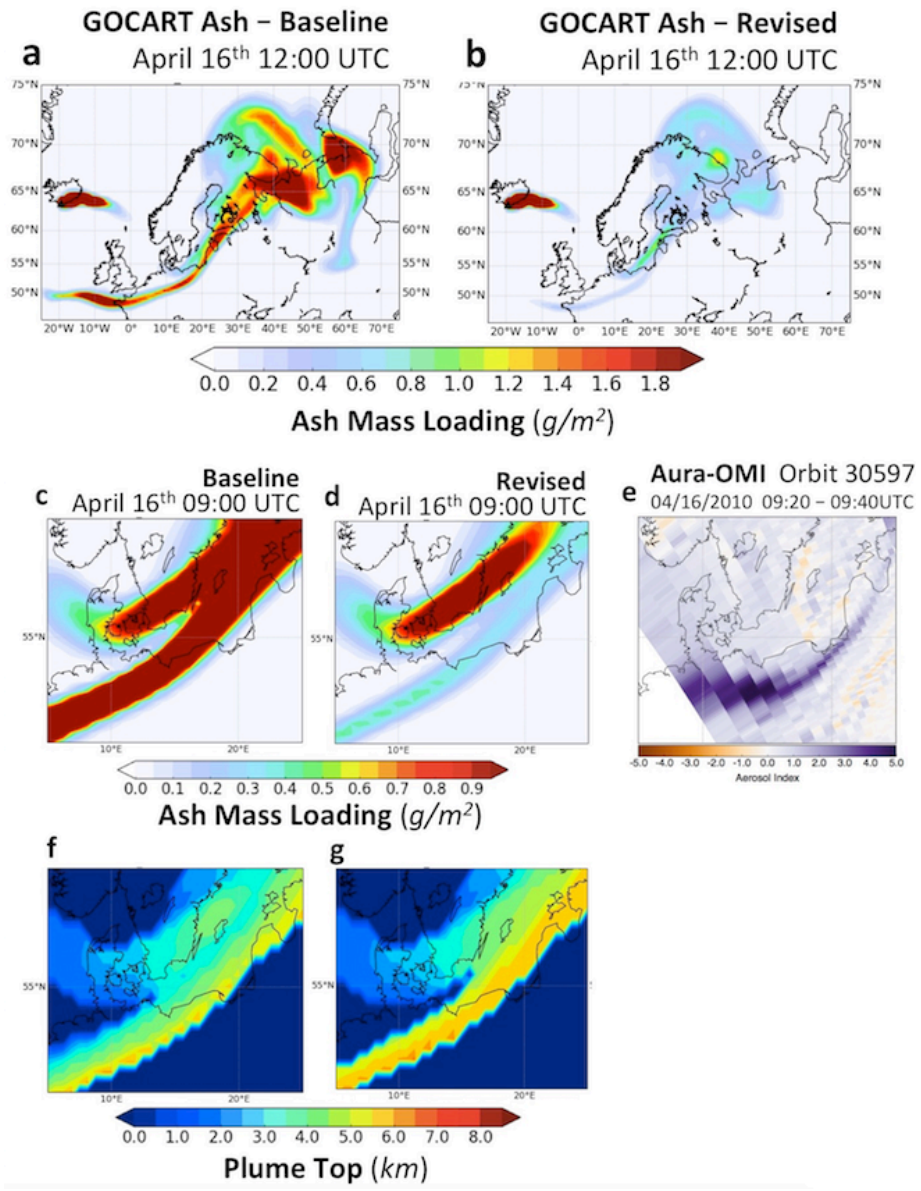

Figure 3.9 Comparison of the baseline and revised ash simulations for April 16th 2010. The full extent of the baseline (a) and revised (b) ash clouds are shown as ash mass loading maps at 12:00 UTC. Zoomed-in views of the ash cloud that approached central Europe are shown for baseline (c) and revised (d) ash mass loadings, and for baseline (f) and revised (g) cloud top altitudes. The OMI Aerosol Index (AI) observations at 09:20 – 09:40 UTC are shown in (e).

In the OMI observations from April 16th, a well-defined ash cloud extends over central Europe. Figure 3.9 shows a zoomed in view of the ash cloud as it

approaches central Europe. In both baseline and revised simulations, the ash cloud is sheared into two filament-like structures that advect across central Europe. The leading filament is associated with the leading edge of the ash cloud from April 15th, and similarly the trailing filament is associated with the trailing part of the cloud on April 15th that tracks back to the volcano, see Figure 3.4e. This is apparent from the comparison of the baseline vs. revised simulation, where the mass of the leading filament has been greatly reduced in the revised simulation. The evolution of the ash cloud shown in Figure 3.4 can also be used to understand the development of the two filament structures.

The OMI observations, Figure 3.9 (e), match better with the location of the leading filament, which is unexpected. Observations from OMI, IASI [*Darce et al. 2011*], and SEVIRI [*Prata and Prata, 2012*] show that the ash cloud that travelled over central Europe is associated with the trailing part of the ash cloud from April 15th, and should match the trailing filament. This difference between OMI observations and the model simulation is likely due to the inaccuracies in the quantification of the source parameters and meteorology. In particular, there are inconsistencies between the revised simulation and the OMI observations on April 15th that are likely associated with inaccurate ash emission source terms. As the model simulates the forward movement of the ash cloud I should generally expect the model and observations to drift further apart with time.

The two filament-like structures of the ash cloud in the model simulations are likely accurate, but with an exaggerated spatial extent. Observations from SEVIRI on April 16th at 8:00 UTC show a two filament-like structures for the ash cloud over

central Europe [*Webley et al., 2012*], though they are much closer together then in either model simulation. The two filament-like structure is less detailed in the SEVIRI retrievals by Prata and Prata [*2012*], but they still show that ash cloud over central Europe has a leading and trailing layer on April 16th at 05:30 UTC.

The ash plume's arrival over central Europe and vertical distribution was well observed by satellite based lidar [*Winker et al., 2012*] and ground based lidar and ceilometers [*Flentje et al., 2010, Emeis et al., 2011*]. As shown in Emeis et al. [*2011*], the ceilometer and lidar observation network over the northern alpine region measured the leading edge of the ash cloud at 6 km - 7.5 km that gradually descends down to 2 km as the ash cloud passed. The leading edge of the ash cloud is also characterized by a thinner (approximately 0.25 km) and weaker scattering signal, descending until 3 km - 4 km, when the scattering signal is much stronger and the cloud is notably thicker (approximately 0.5 km). These observations match those seen by CALIOP over this region [*Winker et al., 2012*]. These observations are better captured in the revised simulation than in the baseline simulation. The plume top plots show that the leading filament is at a higher altitude then the following filament. In the baseline simulation, the leading filament has a plume top from 3 km to 6 km, whereas the revised simulation places the leading filament higher, at 5 km - 7 km. The trailing filament is at the same plume top altitude in both simulations, 2km - 3.5 km. The revised simulation also places more ash mass in the lower altitude, trailing edge of the ash cloud.

3.*8 Discussion*

In previous model simulations of the long-range transport of the 2010 Eyjafjallajökull

volcanic ash cloud, local Keflavík, Iceland radar observations were used to initialize height-time dependence of the ash emission source term. In this study, I used an inverse trajectory analysis to construct a revised emission source term, which improved agreement of the long-term ash dispersion simulation with satellite and ground-based observations. I show that neglecting Eyjafjallajökull volcanic ash emissions before 21:00 UTC on April 14th yields a better match with satellite and ground-based observations. This alteration to the baseline ash emissions has the effect of removing 12 hours of the initial period of volcanic activity from the emission source term, where some of the highest radar observed plume heights were reported.

Previous studies of the Eyjafjallajökull eruption have noted the discrepancy between the model simulations of volcanic ash and satellite and ground-based observations, particularly on the initial days of the eruption [*Webley et al., 2012; Darce et al., 2011; Thomas and Prata 2011; Prata and Prata 2012*] Webley et al. [*2012*] and Thomas and Prata [*2011*] both suggest that this difference may be the result of thermal infrared (TIR) satellite observations limited sensitivity to the fine (less than 1 micron) and coarse (more than 30 micron) ash size or large mass loading making ash plume opaque to transmitted thermal radiation. Though possible, this explanation would require significant portions of the initial ash cloud to be confined exclusively to size ranges where the TIR instruments lack ash sensitivity, specifically in the diameter range of 32 to 64 microns [*Stohl et al., 2011*] or smaller than 1 micron [*Prata and Prata, 2012*]. Recall that ash particles greater than 64 microns in diameter settled out too quickly to influence long-range downwind ash concentrations [*Webley*

et al., 2012]. Furthermore, since the OMI UV-based Aerosol Index (AI) is sensitive to all ash sizes [*Krotkov et al., 1997; 1999ab; Torres et al., 1998; Carn and Krotkov 2016*], the correlation between OMI, IASI and SEVIRI further suggests that satellite observations were observing the full extent of the ash cloud on April 15th. It's also possible that the full extent of the ash was possibly below the threshold of the satellite observations [*Thomas and Prata 2012*]. In a sense, this is always true since satellite instruments have a detection threshold limit. However, my results suggest that any emissions before 21:00 UTC on April 14th would have had a significantly lower impact on the long-range ash transport than the emissions observed afterwards. This would be very counterintuitive since the initial hours of the eruption marked the highest sustained plume top altitudes.

Other studies have noted errors in modeling the timing of the ash cloud, where the modeled ash cloud arrives at UK on April 16th, but 13 hours too early [*Darce et al., 2012*]. Emeis et al., [*2012*] also notes an early arrival of the modeled ash cloud, but by only a few hours. Darce et al. [*2012*] suggested that errors in model meteorology (i.e., the wind fields) may explain the differences between the modeled and observed ash timing. While generally true, the revised emissions present a specific correction to the volcanic source term that yield better agreement with satellite observations, despite the uncertainties in the meteorology.

The results from my analysis are not meant to imply that the eruption did not begin until 21:00 UTC. The Keflavík radar did indeed observe the volcanic plume starting at 09:00 UTC on April 14th and this aligns with other local reports [*Gudmundsson et al., 2012*]. The results from this study suggests that little or no fine

ash was transported far downwind of Eyjafjallajökull until after 21:00 UTC on April 14th. Understanding exactly why this might be the case is beyond the scope of this study, but I offer some insight into possible reasons.

As noted previously, the radar observations tend to be more sensitive to larger ash particles (> 64 microns) [*Marzano et al. 2011*]. In this study, as with others, it's assumed that the radar observed plume top is representative of all ash particles in the volcanic plume. The ash size distribution is also assumed constant throughout the duration of the eruption. It's possible that the early phase of the eruption was dominated by coarse ash particles too large to undergo long-range transport. Radar observations are generally less sensitive to the fine ash, which has lower sedimentation velocities and could be transported over large distances.

The eruption of Eyjafjallajökull began underneath a 200 m thick glacier [*Gudmundsson et al., 2012*], which subsequently melted, allowing the volcano to erupt plumes of ash and SO_2 into the atmosphere. It seems plausible that the beginning of the eruption was marked by a volcanic plume dominated by steam, full of hydrometeors that potentially acted to rainout ash [*Textor et al., 2006a,b*] and quickly oxidize SO_2. Gudmundsson et al., [*2012*] notes that during the beginning of the eruption, on April 14th - 15th, the eruption plume varied in color from white to dark grey, suggesting a steam-rich or ash-rich plume, respectively. Although Gudmundsson et al., [*2012*] doesn't comment on the timing of these variations, MODIS observations from 14:30 UTC on April 14th show a white volcanic plume emitted from Eyjafjallajökull in Figure 3.10a. This is in stark contrast to the dark grey clouds MODIS observed on April 15th, Figure 3.10b. Furthermore, the early

steam volcanic plume observed on April 14th was not operationally flagged as ash by Support to Aviation Control Service (SACS website: http://sacs.aeronomie.be) [*Brenot et al., 2014*]. Gudmundsson et al., [*2012*] also notes that the most intense ash fallout began at 18:30 UTC on April 14th, which is close to the time this study has identified as the beginning of the long-range ash transport. Aggregation processes also limit the long-range transport of volcanic ash by enabling premature sedimentation of fine ash. Observations by Taddeucci et al., [2011] estimated that aggregation processes contributed to a ten-fold increase in ash mass sedimentation rates for the Eyjafjallajökull eruption. Though it should be noted that Taddeucci et al. [*2011*] looked at later periods of the eruption, in May 2010.

For the reasons previously stated, it seems plausible that during the initial hours of the Eyjafjallajökull eruption, the volcanic plume was steam-rich, enabling aggregation processes that caused premature sedimentation of fine ash. Later, on April 14th, the composition of the volcanic plume changed, allowing for the long-range transport of fine ash.

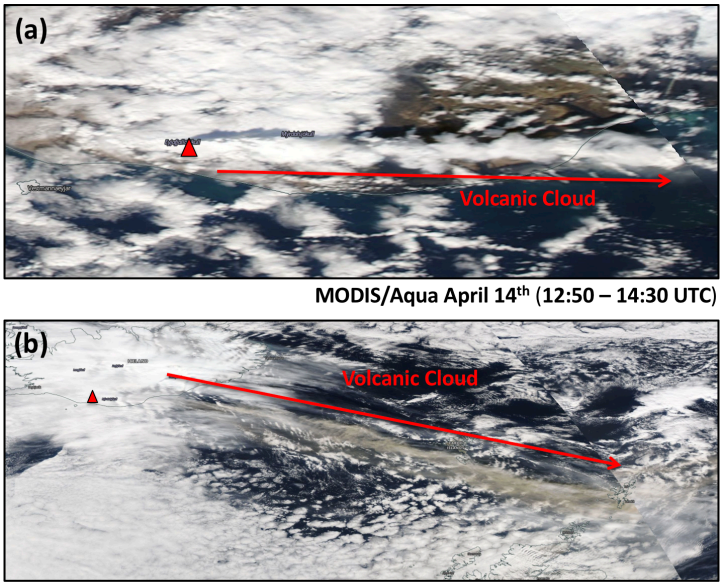

Figure 3.10 MODIS/Aqua True color composite observations of the Eyjafjallajökull volcanic plume. The top panel (a) shows a white, predominantly steam plume extending from the volcano on April 14th from 12:50 to 14:30 UTC. The bottom panel (b) shows the dark gray ash dominated plume extending from the volcano on April 15th from 11:50 UTC to 13:30 UTC.

The results of this work help explain why the London VAAC Volcanic Ash Advisories (VAAs) during the initial period of the eruption appear to overestimate the extent of the volcanic ash cloud. The VAA's were generated using the Numerical Atmospheric-dispersion Modeling Environment (NAME) and source terms derived from the Keflavík radar plume top observations [*Webster et al., 2012*]. Based on my analysis, the direct use of radar observations to initialize ash dispersion model simulations would have greatly contributed to the overestimation of the ash cloud extent in VAA forecasts. The revised simulations collapsed the extent of the ash cloud, yielding a better agreement with satellite observations. It's true that during the early stages of the Eyjafjallajökull eruption, the VAAC VAAs were based on an "any possible ash" restriction and have since pushed for more quantitative forecast. However, this would not have changed the extent of the overestimate of the ash cloud on April 15th. The baseline simulation shows that even a more quantitative

forecast would have led to similar extent of ash, since the source terms would still overestimate the timing and height of the Eyjafjallajökull ash emissions being transported away from the volcano.

Further implications of the results presented in this study center on the quantification of the mass of the airborne ash emitted from the Eyjafjallajökull eruption. By removing the higher altitude plume top observations from the ash emissions, the total ash mass in the revised simulation was significantly lower than in the baseline simulation. If the revised ash emissions are indeed a more accurate representation of actual fine ash emissions, then current dispersion modeling studies will have greatly overestimated the fraction of fine ash emitted from the Eyjafjallajökull eruption.

3.9 Conclusions

Forecasts of the Eyjafjallajökull ash cloud led to mass airspace cancellations, resulting in eased restrictions on the threshold concentrations of ash that were deemed safe for aviation. In this study, I reconstructed the Eyjafjallajökull ash cloud using ash emission source terms similar to those used in the original ash forecasts and further used by many later studies. The ash cloud transport was simulated using the newly developed ash modeling capabilities of GOCART within GEOS-5. The plume top altitude time series observed by the Keflavík C-band weather radar was used to define the initial ash cloud height, and the MER-height relationship was used to estimate the ash flux timeseries. Using these ash emission source terms, ash

simulations were produced that generally agreed with the ash forecasts at the time of the eruption and with many other papers that followed a similar methodology.

Satellite observations of the Eyjafjallajökull ash cloud's location on April 15th 2010 didn't match simulations of the ash cloud's horizontal extent. Backward trajectory analysis of the satellite observations suggests that volcanic ash clouds did not begin adverting away from the volcano until 21:00 UTC on April 14th, over 12 hours later then the radar observations suggest. The ash emission source terms were refined using the emission timeseries estimated from the backward trajectory analysis and another set of ash simulations were made using these refined emission source terms. The refined ash simulations reduced the horizontal extent of the ash cloud, coming into a better agreement with satellite observations.

The results from this study suggest that any ash from the initial hours of the Eyjafjallajökull eruption did not transport far away from the volcano. The model simulations that used the radar observations to directly construct ash emission source terms (1) overestimate the extent of the Eyjafjallajökull ash cloud by initializing the volcanic cloud to early into the atmosphere and (2) overestimate the ash mass loading since the radar observed the highest plume top altitudes at initial hours of the Eyjafjallajökull eruption, which the MER-height relationship translates into much larger ash emission fluxes.

I have proposed several theories as to why the radar plume top observations in the initial phase did not accurately characterize the emission source terms for fine ash. For example, the radar instrument is not sensitive to fine ash so it is possible that little to no fine ash was actually being emitted from the volcano during the initial hours of

the eruption. It is also plausible that the initial Eyjafjallajökull volcanic plume was dominated by steam and contained little ash initially.

Regardless of the reason, these results highlight the need for better characterization of ash emission source terms. The radar plume top observations provided unprecedented temporally resolved ash plume top observations, but lacked information about the ash initial particle size distributions. At the time of the eruption, the radar observations were assumed to be describing both fine and coarse ash. Many publications noted throughout this chapter also made this assumption, leading to ash cloud simulations that greatly overestimate the extent of the Eyjafjallajökull on the initial days of the eruption.

This chapter has highlighted the importance of understanding the limitations of volcanic plume and cloud observations. In the next chapter, I further my investigation into the limitations of volcanic cloud observations by constructing an experimental setup to evaluate the accuracy and limitation of the OMPS SO_2 retrieval.

References, Chapter 3

Allen, D., M. Schoeberl, and J. Herman (1999), Trajectory modeling of aerosol clouds observed by TOMS, *Journal of Geophysical Research: Atmospheres*, *104*(D22), 27461-27471.

Arason, P., G. Petersen, and H. Bjornsson (2011), Observations of the altitude of the volcanic plume during the eruption of Eyjafjallajökull, April–May 2010, *Earth System Science Data*, *3*(1), 9-17.

Brenot, H., N. Theys, L. Clarisse, J. Van Geffen, J. Van Gent, M. Van Roozendael, R. Van Der A, D. Hurtmans, P.-F. Coheur, and C. Clerbaux (2014), Support to Aviation Control Service (SACS): an online service for near real-time satellite monitoring of volcanic plumes, *Natural hazards and earth system sciences*, *14*(5), 1099-1123.

Buchard, V., C. Randles, A. Da Silva, A. Darmenov, P. Colarco, R. Govindaraju, R. Ferrare, J. Hair, A. Beyersdorf, and L. Ziemba (2017), The MERRA-2 aerosol reanalysis, 1980 onward. Part II: Evaluation and case studies, *Journal of Climate*, *30*(17), 6851-6872.

Carboni, E., R. Grainger, J. Walker, A. Dudhia, and R. Siddans (2012), A new scheme for sulphur dioxide retrieval from IASI measurements: application to the Eyjafjallajökull eruption of April and May 2010, *Atmospheric Chemistry and Physics*, *12*(23), 11417-11434.

Carn, S.A. and N.A. Krotkov (2016), UV Satellite Measurements of Volcanic Ash, In: S. Mackie, K. Cashman, A. Rust, H. Ricketts and I.M. Watson (eds.), *Volcanic ash: Hazard Observation*, Elsevier, pp. 217-231, doi:10.1016/B978-0-08-100405-0.00018-5

Carn, S., K. Yang, A. Prata, and N. Krotkov (2015), Extending the long-term record of volcanic SO2 emissions with the Ozone Mapping and Profiler Suite nadir mapper, *Geophysical Research Letters*, *42*(3), 925-932.

Carn, S. A., A. J. Krueger, N. A. Krotkov, K. Yang, and K. Evans (2009), Tracking volcanic sulfur dioxide clouds for aviation hazard mitigation, *Natural Hazards*, *51*(2), 325-343.

Chin, M., P. Ginoux, S. Kinne, O. Torres, B. N. Holben, B. N. Duncan, R. V. Martin, J. A. Logan, A. Higurashi, and T. Nakajima (2002), Tropospheric aerosol optical

thickness from the GOCART model and comparisons with satellite and Sun photometer measurements, *Journal of the atmospheric sciences*, *59*(3), 461-483.

Chin, M., R. B. Rood, S. J. Lin, J. F. Müller, and A. M. Thompson (2000), Atmospheric sulfur cycle simulated in the global model GOCART: Model description and global properties, *Journal of Geophysical Research: Atmospheres*, *105*(D20), 24671-24687.

Clarisse, L., F. Prata, J. L. Lacour, D. Hurtmans, C. Clerbaux, and P. F. Coheur (2010), A correlation method for volcanic ash detection using hyperspectral infrared measurements, *Geophysical research letters*, *37*(19).

Clerbaux, C., A. Boynard, L. Clarisse, M. George, J. Hadji-Lazaro, H. Herbin, D. Hurtmans, M. Pommier, A. Razavi, and S. Turquety (2009), Monitoring of atmospheric composition using the thermal infrared IASI/MetOp sounder, *Atmospheric Chemistry and Physics*, *9*(16), 6041-6054.

Colarco, P., A. da Silva, M. Chin, and T. Diehl (2010), Online simulations of global aerosol distributions in the NASA GEOS-4 model and comparisons to satellite and ground-based aerosol optical depth, *Journal of Geophysical Research: Atmospheres*, *115*(D14).

Dacre, H. F., A. L. Grant, R. J. Hogan, S. E. Belcher, D. Thomson, B. Devenish, F. Marenco, M. Hort, J. M. Haywood, and A. Ansmann (2011), Evaluating the structure and magnitude of the ash plume during the initial phase of the 2010 Eyjafjallajökull eruption using lidar observations and NAME simulations, *Journal of Geophysical Research: Atmospheres*, *116*(D20).

Emeis, S., R. Forkel, W. Junkermann, K. Schäfer, H. Flentje, S. Gilge, W. Fricke, M. Wiegner, V. Freudenthaler, and S. Grob (2011), Measurement and simulation of the

16/17 April 2010 Eyjafjallajokull volcanic ash layer dispersion in the northern Alpine region, *Atmospheric Chemistry and Physics*, *11*(6), 2689.

Flentje, H., H. Claude, T. Elste, S. Gilge, U. Köhler, C. Plass-Dülmer, W. Steinbrecht, W. Thomas, A. Werner, and W. Fricke (2010), The Eyjafjallajökull eruption in April 2010–detection of volcanic plume using in-situ measurements, ozone sondes and lidar-ceilometer profiles, *Atmospheric Chemistry and Physics*, *10*(20), 10085-10092.

Folch, A., A. Costa, and S. Basart (2012), Validation of the FALL3D ash dispersion model using observations of the 2010 Eyjafjallajökull volcanic ash clouds, *Atmospheric Environment*, *48*, 165-183.

Ginoux, P., M. Chin, I. Tegen, J. M. Prospero, B. Holben, O. Dubovik, and S. J. Lin (2001), Sources and distributions of dust aerosols simulated with the GOCART model, *Journal of Geophysical Research: Atmospheres*, *106*(D17), 20255-20273.

Gudmundsson, M. T., T. Thordarson, Á. Höskuldsson, G. Larsen, H. Björnsson, F. J. Prata, B. Oddsson, E. Magnússon, T. Högnadóttir, and G. N. Petersen (2012), Ash generation and distribution from the April-May 2010 eruption of Eyjafjallajökull, Iceland, *Scientific reports*, *2*, 572.

Hughes, E., L. Sparling, S. Carn, and A. Krueger (2012), Using horizontal transport characteristics to infer an emission height time series of volcanic SO2, *Journal of Geophysical Research: Atmospheres*, *117*(D18).

Hughes, E., J. Yorks, N. Krotkov, A. Silva, and M. McGill (2016), Using CATS near-real-time lidar observations to monitor and constrain volcanic sulfur dioxide (SO2) forecasts, *Geophysical Research Letters*, *43*(20).

Hunt, W. H., D. M. Winker, M. A. Vaughan, K. A. Powell, P. L. Lucker, and C. Weimer (2009), CALIPSO lidar description and performance assessment, *Journal of Atmospheric and Oceanic Technology*, *26*(7), 1214-1228.

Kalnay, E., M. Kanamitsu, R. Kistler, W. Collins, D. Deaven, L. Gandin, M. Iredell, S. Saha, G. White, and J. Woollen (1996), The NCEP/NCAR 40-year reanalysis project, *Bulletin of the American meteorological Society*, *77*(3), 437-472.

Krotkov, N., M. Schoeberl, G. Morris, S. Carn, and K. Yang (2010), Dispersion and lifetime of the SO2 cloud from the August 2008 Kasatochi eruption, *Journal of Geophysical Research: Atmospheres*, *115*(D2).

Krotkov, N. A., S. A. Carn, A. J. Krueger, P. K. Bhartia, and K. Yang (2006), Band residual difference algorithm for retrieval of SO/sub 2/from the aura ozone monitoring instrument (OMI), *IEEE Transactions on geoscience and remote sensing*, *44*(5), 1259-1266.

Krotkov, N. A., A. J. Krueger, P. K. Bhartia, Ultraviolet optical model of volcanic clouds for remote sensing of ash and sulfur dioxide, *J. Geophys. Res*., 102(D18), 21891-21904, 10.1029/97JD01690, 1997

Krotkov, N.A., D.E. Flittner, A.J. Krueger, A. Kostinski, C. Riley and W. Rose, O. Torres, (1999a) Effect of particle non-sphericity on satellite monitoring of drifting volcanic ash clouds, JQSRT, **63**, 613-630

Krotkov, N. A., O. Torres, C. Seftor, A. J. Krueger, A. Kostinski, W. I. Rose, G. J. S. Bluth, D. Schneider, and S. J. Schaefer (1999b), Comparison of TOMS and AVHRR volcanic ash retrievals from the August 1992 eruption of Mt. Spurr, *Geophys. Res. Lett*., 26(4), 455–458

Lacasse, C., S. Karlsdóttir, G. Larsen, H. Soosalu, W. Rose, and G. Ernst (2004), Weather radar observations of the Hekla 2000 eruption cloud, Iceland, *Bulletin of Volcanology*, *66*(5), 457-473.

Levelt, P. F., G. H. van den Oord, M. R. Dobber, A. Malkki, H. Visser, J. de Vries, P. Stammes, J. O. Lundell, and H. Saari (2006), The ozone monitoring instrument, *IEEE Transactions on geoscience and remote sensing*, *44*(5), 1093-1101.

Li, C., J. Joiner, N. A. Krotkov, and P. K. Bhartia (2013), A fast and sensitive new satellite SO2 retrieval algorithm based on principal component analysis: Application to the ozone monitoring instrument, *Geophysical Research Letters*, *40*(23), 6314-6318.

Li, C., N. A. Krotkov, S. Carn, Y. Zhang, R. J. Spurr, and J. Joiner (2017), New-generation NASA Aura Ozone Monitoring Instrument (OMI) volcanic SO 2 dataset: Algorithm description, initial results, and continuation with the Suomi-NPP Ozone Mapping and Profiler Suite (OMPS), *Atmospheric Measurement Techniques*, *10*(2), 445-458.

Lin, S.-J., and R. B. Rood (1996), Multidimensional flux-form semi-Lagrangian transport schemes, *Monthly Weather Review*, *124*(9), 2046-2070.

Lu, S., H. Lin, A. Heemink, G. Fu, and A. Segers (2016), Estimation of volcanic ash emissions using trajectory-based 4D-Var data assimilation, *Monthly Weather Review*, *144*(2), 575-589.

Marzano, F., M. Lamantea, M. Montopoli, S. D. Fabio, and E. Picciotti (2011), The Eyjafjöll explosive volcanic eruption from a microwave weather radar perspective, *Atmospheric Chemistry and Physics*, *11*(18), 9503-9518.

Mastin, L. G., M. Guffanti, R. Servranckx, P. Webley, S. Barsotti, K. Dean, A. Durant, J. W. Ewert, A. Neri, and W. I. Rose (2009), A multidisciplinary effort to assign realistic source parameters to models of volcanic ash-cloud transport and dispersion during eruptions, *Journal of Volcanology and Geothermal Research*, *186*(1-2), 10-21.

Matthias, V., A. Aulinger, J. Bieser, J. Cuesta, B. Geyer, B. Langmann, I. Serikov, I. Mattis, A. Minikin, and L. Mona (2012), The ash dispersion over Europe during the Eyjafjallajökull eruption–Comparison of CMAQ simulations to remote sensing and air-borne in-situ observations, *Atmospheric Environment*, *48*, 184-194.

Petersen, G. N. (2010), A short meteorological overview of the Eyjafjallajökull eruption 14 April–23 May 2010, *Weather*, *65*(8), 203-207.

Prata, A., and C. Bernardo (2007), Retrieval of volcanic SO2 column abundance from Atmospheric Infrared Sounder data, *Journal of Geophysical Research: Atmospheres*, *112*(D20).

Prata, A., and A. Prata (2012), Eyjafjallajökull volcanic ash concentrations determined using Spin Enhanced Visible and Infrared Imager measurements, *Journal of Geophysical Research: Atmospheres*, *117*(D20).

Randles, C., A. M. da Silva, V. Buchard, P. Colarco, A. Darmenov, R. Govindaraju, A. Smirnov, B. Holben, R. Ferrare, and J. Hair (2017), The MERRA-2 aerosol reanalysis, 1980 onward. Part I: System description and data assimilation evaluation, *Journal of climate*, *30*(17), 6823-6850.

Schmetz, J., P. Pili, S. Tjemkes, D. Just, J. Kerkmann, S. Rota, and A. Ratier (2002), An introduction to Meteosat second generation (MSG), *Bulletin of the American Meteorological Society*, *83*(7), 977-992.

Schoeberl, M., and L. Sparling (1995), Trajectory modelling, paper presented at Diagnostic tools in atmospheric physics.

Schoeberl, M. R., S. D. Doiron, L. R. Lait, P. A. Newman, and A. J. Krueger (1993), A simulation of the Cerro Hudson SO2 cloud, *Journal of Geophysical Research: Atmospheres*, *98*(D2), 2949-2955.

Schumann, U., B. Weinzierl, O. Reitebuch, H. Schlager, A. Minikin, C. Forster, R. Baumann, T. Sailer, K. Graf, and H. Mannstein (2011), Airborne observations of the Eyjafjalla volcano ash cloud over Europe during air space closure in April and May 2010, *Atmospheric Chemistry and Physics*.

Seftor, C., N. Hsu, J. Herman, P. Bhartia, O. Torres, W. I. Rose, D. J. Schneider, and N. Krotkov (1997), Detection of volcanic ash clouds from Nimbus 7/total ozone mapping spectrometer, *Journal of Geophysical Research: Atmospheres*, *102*(D14), 16749-16759.

Stohl, A., A. Prata, S. Eckhardt, L. Clarisse, A. Durant, S. Henne, N. I. Kristiansen, A. Minikin, U. Schumann, and P. Seibert (2011), Determination of time-and height-resolved volcanic ash emissions and their use for quantitative ash dispersion modeling: the 2010 Eyjafjallajökull eruption, *Atmospheric Chemistry and Physics*, *11*(9), 4333-4351.

Suarez, M. J., M. Rienecker, R. Todling, J. Bacmeister, L. Takacs, H. Liu, W. Gu, M. Sienkiewicz, R. Koster, and R. Gelaro (2008), The GEOS-5 Data Assimilation System-Documentation of Versions 5.0. 1, 5.1. 0, and 5.2. 0.

Taddeucci, J., P. Scarlato, C. Montanaro, C. Cimarelli, E. Del Bello, C. Freda, D. Andronico, M. Gudmundsson, and D. Dingwell (2011), Aggregation-dominated ash settling from the Eyjafjallajökull volcanic cloud illuminated by field and laboratory high-speed imaging, *Geology*, *39*(9), 891-894.

Textor, C., H.-F. Graf, M. Herzog, J. M. Oberhuber, W. I. Rose, and G. Ernst (2006a), Volcanic particle aggregation in explosive eruption columns. Part II: Numerical experiments, *Journal of Volcanology and Geothermal Research*, *150*(4), 378-394.

Textor, C., H.-F. Graf, M. Herzog, J. M. Oberhuber, W. I. Rose, and G. G. Ernst (2006b), Volcanic particle aggregation in explosive eruption columns. Part I: Parameterization of the microphysics of hydrometeors and ash, *Journal of Volcanology and Geothermal Research*, *150*(4), 359-377.

Thomas, H. E., and A. Prata (2011), Sulphur dioxide as a volcanic ash proxy during the April-May 2010 eruption of Eyjafjallajokull Volcano, Iceland.

Torres, O., A. Tanskanen, B. Veihelmann, C. Ahn, R. Braak, P. K. Bhartia, P. Veefkind, and P. Levelt (2007), Aerosols and surface UV products from Ozone Monitoring Instrument observations: An overview, *Journal of Geophysical Research: Atmospheres*, *112*(D24).

Torres, O., P. K. Bhartia, J. R. Herman, Z. Ahmad, and J. Gleason. "Derivation of aerosol properties from satellite measurements of backscattered ultraviolet radiation: Theoretical basis." *Journal of Geophysical Research: Atmospheres* 103, no. D14 (1998): 17099-17110.

Vogfjörd, K., S. Jakobsdóttir, G. Gudmundsson, M. Roberts, K. Ágústsson, T. Arason, H. Geirsson, S. Karlsdóttir, S. Hjaltadóttir, and U. Ólafsdóttir (2005), Forecasting and monitoring a subglacial eruption in Iceland, *Eos, Transactions American Geophysical Union*, *86*(26), 245-248.

Webley, P., T. Steensen, M. Stuefer, G. Grell, S. Freitas, and M. Pavolonis (2012), Analyzing the Eyjafjallajökull 2010 eruption using satellite remote sensing, lidar and

WRF-Chem dispersion and tracking model, *Journal of Geophysical Research: Atmospheres*, *117*(D20).

Webster, H., D. Thomson, B. Johnson, I. Heard, K. Turnbull, F. Marenco, N. Kristiansen, J. Dorsey, A. Minikin, and B. Weinzierl (2012), Operational prediction of ash concentrations in the distal volcanic cloud from the 2010 Eyjafjallajökull eruption, *Journal of Geophysical Research: Atmospheres*, *117*(D20).

Winker, D., Z. Liu, A. Omar, J. Tackett, and D. Fairlie (2012), CALIOP observations of the transport of ash from the Eyjafjallajökull volcano in April 2010, *Journal of Geophysical Research: Atmospheres*, *117*(D20).

Yang, K., N. A. Krotkov, A. J. Krueger, S. A. Carn, P. K. Bhartia, and P. F. Levelt (2007), Retrieval of large volcanic SO2 columns from the Aura Ozone Monitoring Instrument: Comparison and limitations, *Journal of Geophysical Research: Atmospheres*, *112*(D24).

Yang, K., X. Liu, P. K. Bhartia, N. A. Krotkov, S. A. Carn, E. J. Hughes, A. J. Krueger, R. J. Spurr, and S. G. Trahan (2010), Direct retrieval of sulfur dioxide amount and altitude from spaceborne hyperspectral UV measurements: Theory and application, *Journal of Geophysical Research: Atmospheres*, *115*(D2).

Chapter 4: OMPS SO_2 Observation System Simulation Experiment

4.1 Introduction

Observations play a vital role in quantifying the emission source terms describing the initial state of volcanic clouds. Maps of the SO_2 total column density from UV observations have frequently been used to quantify the amount of SO_2 emitted from volcanic eruptions and estimate a volcanic SO_2 emission flux used in model simulations [*Wang et al, 2013, Hughes et al., 2012; Hughes et al. 2016, Flemming et al., 2013, Krotkov et al., 2010; Carn et al., 2009; Carn et al., 2015*]. Current UV SO_2 retrievals do not [explicitly] consider the potential effects of aerosols when computing the SO_2 total column densities. While not all volcanic clouds produce large masses of volcanic ash and sulfate aerosols, some volcanic eruptions have produced volcanic clouds with large aerosol loadings, such as in the 1991 eruption of Mt. Pinatubo [*Guo et al., 2004*]. In this study, I seek to investigate and quantify possible biases that volcanic aerosols may impose on the OMPS SO_2 retrieval.

I perform an Observing System Simulation Experiment (OSSE) to evaluate the effects of aerosols on the OMPS SO_2 retrieval. OSSE's have frequently been used to evaluate the influence of satellite observations on meteorological data assimilation systems [*Errico et al., 2013*]. In this study, I construct an OSSE in a manner similar to Colarco et al. [*2017*], where the atmospheric composition is

simulated and a radiative transfer model is then used to generate top-of-the-atmosphere (TOA) radiances to serve as input the OMPS SO_2 retrieval.

In the following section, I give a general overview of the OSSE setup and note some of the models used in this study that have yet to be discussed. This is followed by a discussion of the nature runs, detailing the setup and results of the simulations. The observation simulator is then discussed, followed by an analysis of the SO_2 generated from OMPS retrieval.

4.2 OSSE Methodology

The goal of the OMPS SO_2 OSSE is to evaluate the accuracy of the OMPS SO_2 retrieval and better understand its limitations. Performing an OSSE allows inputs to OMPS SO_2 retrieval to be controlled and the retrieval output checked under various conditions. The OSSE consists of three parts, (1) the nature run, (2) the observation simulator, and (3) the retrieval evaluation. The retrieval evaluation can also be considered the experiment part of this OSSE, as this OSSE is being setup the evaluate the OMPS SO_2 retrieval.

In the nature run, the atmospheric composition is simulated using an Earth system model. For this study, I use the GEOS-5 Earth system model to simulate the general state of the atmosphere and the GOCART and Community Aerosol and Radiation Model for Atmospheres (CARMA) [*Toon et al., 1988; Jensen et al., 1994; Ackerman et al., 1995*] models to simulate chemical and aerosol species within GEOS-5. The GOCART model is used to simulate the transport of SO_2, and the sulfuric acid production from SO_2. Most of the aerosol modeling is performed by the

sectional aerosol and cloud microphysical model CARMA. I use CARMA to model volcanic ash and the sulfate aerosols that are produced by oxidation of SO_2 from GOCART. CARMA has previously been used to model dust [*Colarco et al., 2004, 2014*], smoke [*Matichuk et al., 2007, 2008*] and sulfate aerosols [*English et al., 2011, 2012*]. In this study, CARMA is used to model ash in manner similar to how GOCART modeled ash in the previous chapter. The only microphysical process that affects ash in CARMA is sedimentation, whereas sulfate aerosols also undergo nucleation, coagulation, and condensational growth. The primary benefit of using CARMA to model aerosols in this study instead of GOCART is that CARMA contains a larger number of size bins and that permit a more realistic characterization of the ash and sulfate aerosol size distribution.

As the focus of this experiment is on OMPS SO_2 column observations of volcanic clouds, the GEOS-5 model will be used to simulate the dispersion of a volcanic cloud produced from an explosive volcanic eruption. For this OSSE, I simulate the volcanic clouds emitted by the 1991 eruption of Mt. Pinatubo. It should be noted that it is not necessary to reconstruct a volcanic simulation based on an actual volcanic eruption. I could have constructed a fictitious volcanic eruption for this experiment, but a realistic simulation was chosen for other collaborative research efforts that are beyond the scope of this work.

The GEOS-5 nature run is used to simulate 3D fields of ozone, SO_2, sulfate aerosols, and volcanic ash. In order to generate synthetic radiances, as input for the OMPS SO_2 algorithm, an observation simulator is needed. The observation simulator derives optical properties from the nature run fields, such as gas extinction and Mie

scattering optical properties, and then uses a radiative transfer model to simulate the top-of-the-atmosphere (TOA) radiances that would be observed by the OMPS instrument. For this experiment, the state-of-the-art VLIDORT (Vector LInearized Discrete Ordinate Radiative Transfer) [*Spurr 2006*] radiative transfer code is used. VLIDORT is used to generate radiances at the wavelengths channels used in the OMPS SO_2 MS_SO2 algorithm [*Bhartia et al., 2016; Fisher et al., 2017*]. The MS_SO2 algorithm is similar to the BRD and LF SO_2 retrieval previously described but has been adapted to work across multiple UV instruments (TOMS, OMI OMPS). The generated radiances are used as input to the OMPS MS_SO2 algorithm and compared to the GOCART column SO_2 fields used to generate the radiances. This experiment looks at the effects of volcanic ash and sulfate aerosols on the OMPS SO_2 retrieval by comparing the SO_2 computed by the retrieval to the SO_2 from the nature run. Different nature runs are generated in order to evaluate the OMPS SO_2 retrieval under scenarios of no aerosols, sulfate aerosols and both ash and sulfate aerosols. The current experiment setup only simulates "clear-sky" conditions.

4.3 Nature Runs

4.3.1 Setup

The first part of the OMPS SO_2 OSSE consists of a "Nature Run", where the GEOS-5 model is used to simulate the dispersion of a volcanic cloud produced from an explosive volcanic eruption. The goal of a nature run is to construct a realistic simulation of the environment being observed, in this case an atmosphere containing

a dispersed volcanic cloud. Two nature runs are constructed for this experiment, one assuming a volcanic plume consisting of volcanic ash, sulfate aerosols, and SO_2, and a second assuming only sulfate aerosols and SO_2. This chapter includes various contrasts between these two nature runs, and thus I will use the shorthand $NR_{ash+sulfate}$ to refer to the nature run that includes ash, sulfate aerosols, and SO_2, and $NR_{sulfate}$ to refer to the sulfate aerosols and SO_2 only scenario. A summary of the nature run setups is outlined in Table 4.2.

Table 4.2 Summary of Volcanic Eruption Source Terms in the Nature Runs

Nature Run	Ash	Sulfate	SO_2	Plume Top	Plume Base	Duration
	kt	*Mt*	*Mt*	*km*	*km*	UTC (*June 15th 1991*)
$NR_{Ash+Sulfate}$	5,000	4	12	21	18	06:00 – 15:00
$NR_{Sulfate}$	--	4	12	21	18	06:00 – 15:00

The SO_2, sulfate and ash emissions in Table 4.2 were chosen to be representative of a Pinatubo-like volcanic eruption in the mass, composition, injection altitude and timing. The total masses of SO_2 and sulfate were taken from estimates by Guo et al. [*2004a*]. The ash mass was initially assumed to be 50,000 kt, in accordance with Guo et al. [*2004b*], but provided unrealistic results when GEOS-5 was run online. The 50,000 kt ash mass loading produced rapid lofting of the volcanic cloud that pulled ozone poor air from the troposphere into the volcanic plume. While self-lofting of the ash cloud should be expected, this mass loading of ash produced aggressive lofting that resulted in a significant ozone hole within the volcanic cloud that was beyond the ozone bounds assumed by the OMPS retrieval. A 5,000 kt ash mass

produced a less substantial ozone hole that was within a range acceptable for the OMPS retrieval. The 5,000 kt ash mass was used as total ash mass for the $NR_{ash+sulfate}$ simulation.

An altitude distribution of 18 km – 21 km is assumed, similar to the altitude ranges used in other Pinatubo modeling studies [*Aquila et al. 2012; Niemeier et al., 2009; Sekiya et al. 2016*]. For all species, the initial injection altitude profile assumed a uniform distribution from the plume top to the plume bottom.

The largest eruption from 1991 Mt. Pinatubo eruptive event began on June 15th at 05:42 local time (13:42 UTC) and lasted for 9 hours [*Wolfe and Hoblitt, 1996*]. The model simulations begin at 06:00 UTC on June 15th 1991, and assume a 9 hour duration of the emissions. The emission flux over this period was computed by assuming a constant flux rate for each emission species, where the integrated sum equals the total injection amounts previously stated.

The initial ash particle size distribution assumed in $NR_{ash+sulfate}$ is shown in Figure 4.11, which is based off the ash distribution used by Niemeier et al., [*2009*]. The ash particle size distribution follows a log-normal distribution with mean, m = 2.4 μm, and standard deviation, s = 5.7 μm. The ash density is assumed 2,700 kg/m3 across all size bins. In GOCART, the sulfate aerosols are assumed to have a radius r = 0.60 μm, which can evolve in CARMA between r = .0002 μm to r = 3.25 μm across 22 bins.

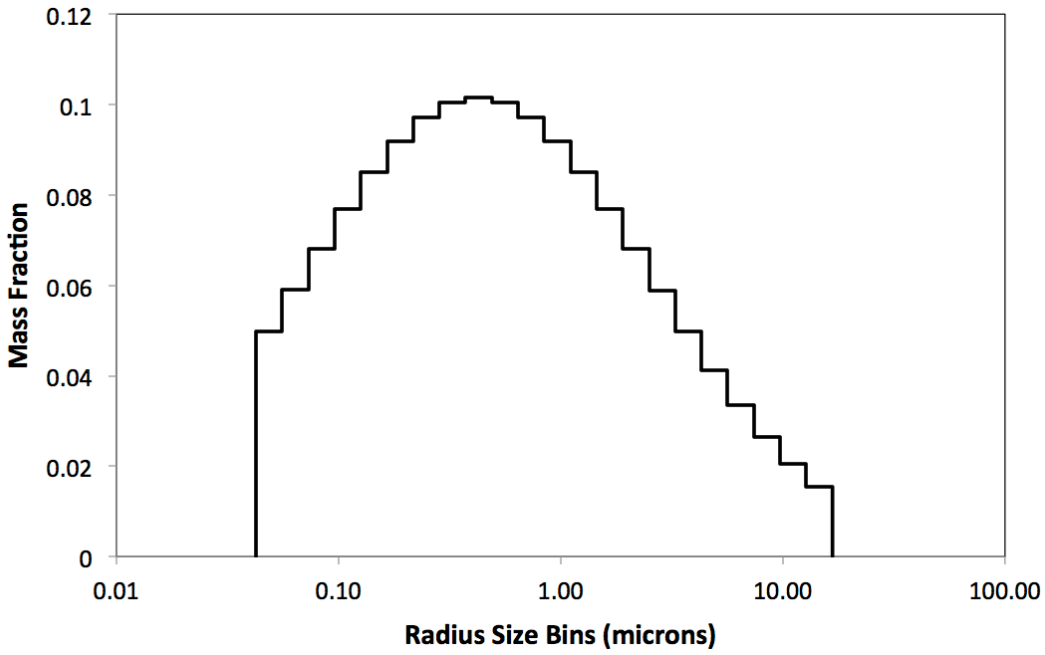

Figure 4.11 Size distribution for the ash particles used in the nature runs.

GEOS-5 is run in forecast mode, initialized with meteorological and atmospheric composition fields from the MERRA-2 analysis. The CARMA and GOCART modules were run online within GEOS-5 with the CARMA aerosols radiatively coupled to the AGCM. The large column ash loadings at the volcano during the period of the simulated eruption in combination with the model radiative coupling cause numerical problems at high model horizontal resolutions. To get around these problems, the initial 42-hour period of the model simulation was run at a coarse cubed-sphere grid at a c90 horizontal resolution (~ 1^{o} x 1^{o}), until June 16th 15:00 UTC. The remaining duration of the model simulation was run on a finer resolution, on a cubed-sphere grid at a c360 horizontal resolution (~25 km) and with 72 vertical layers. The GEOS-5 nature runs were simulated for the period of June 14th 21:00 UTC to June 20th 21:00 UTC, with the model state saved at three-hour

intervals. The ozone fields were taken from the StratChem module [*Pawson et al. 2008*] also run within GEOS-5.

4.3.2 Results

The nature run parameters that will have the greatest influence on changes in the BUV radiance, and subsequently the OMPS retrieval, are the volcanic species ash, SO_2, and sulfate aerosols, as well as atmospheric ozone. The evolution of these species in the nature runs $NR_{sulfate}$ and $NR_{ash+sulfate}$ is shown in Figure 4.12 through Figure 4.15. Aside from the absence of ash in $NR_{sulfate}$, the nature runs were both simulated with identical initial conditions and radiative coupling.

Figure 4.12 - Figure 4.15 show clear differences between the nature runs, mainly, (1) a difference in observed volcanic cloud transport, (2) larger total column SO_2 and sulfate values in the $NR_{sulfate}$ run, and (3) an ozone reduction associated with $NR_{ash+sulfate}$ run that's not present in the $NR_{sulfate}$.

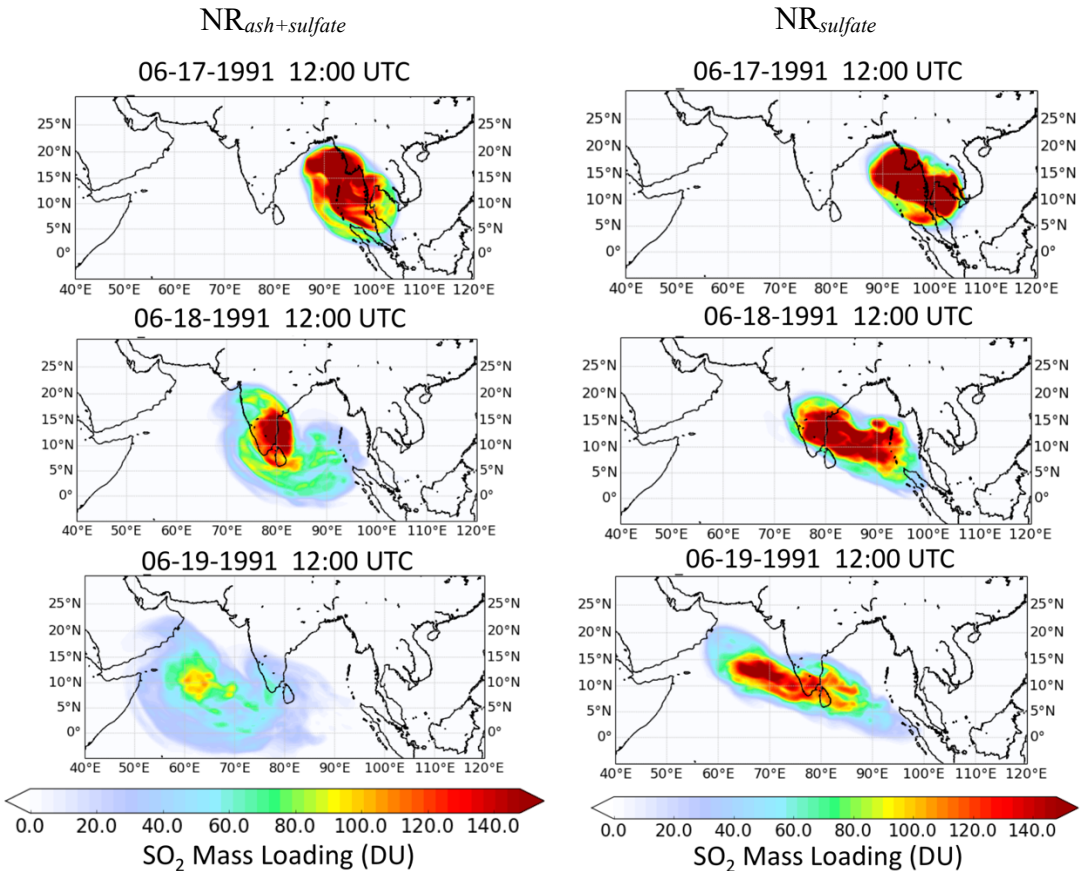

Figure 4.12 Transport of SO_2 in the nature runs. The left panels show the dispersion of SO_2 in $NR_{ash+sulfate}$, while the right panels show the progression for $NR_{sulfate}$. The panels show the vertically integrated column loading of SO_2 at 12:00UTC on June 17th, 18th, and 19th.

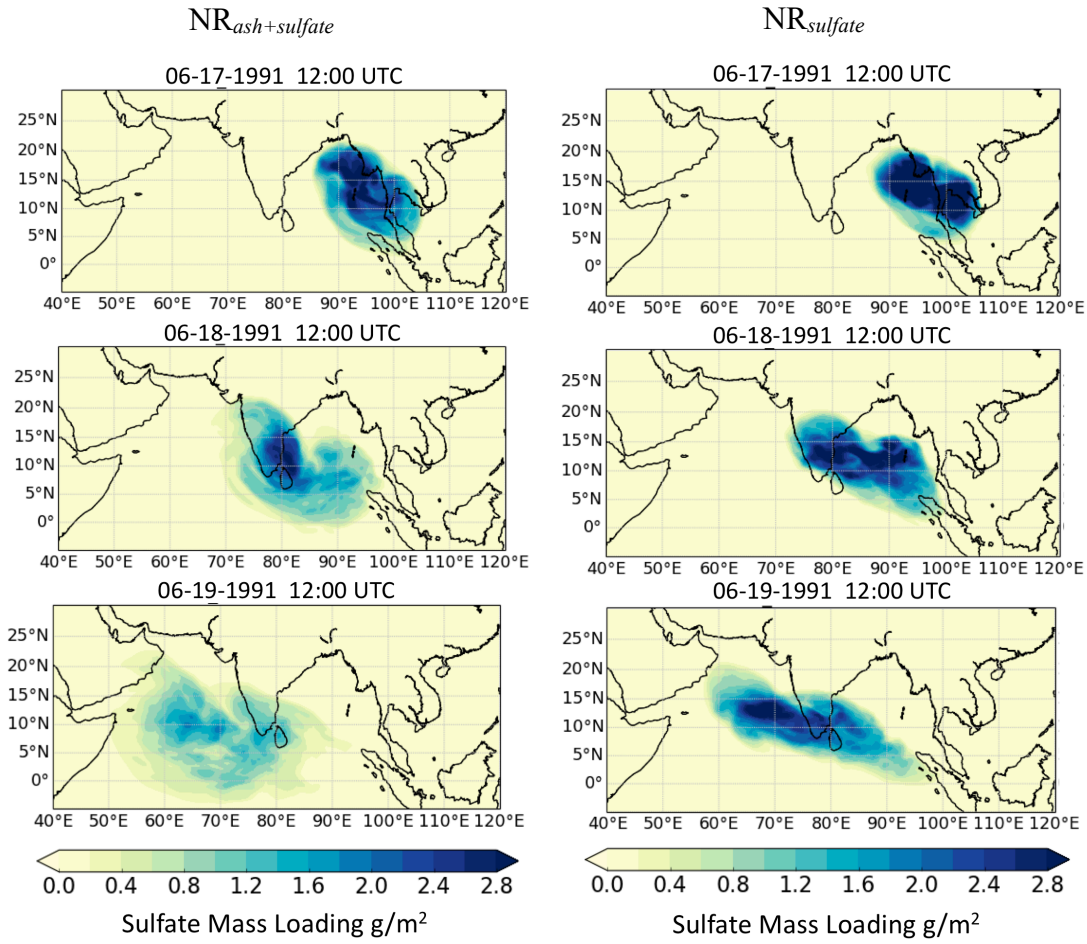

Figure 4.13 Transport of sulfate aerosols in the nature runs. The left panels show the dispersion of SO2 in NRash+sulfate, while the right panels show the progression for NRsulfate. The panels show the vertically integrated column loading of sulfate aerosols at 12:00UTC on June 17th, 18th, and 19th.

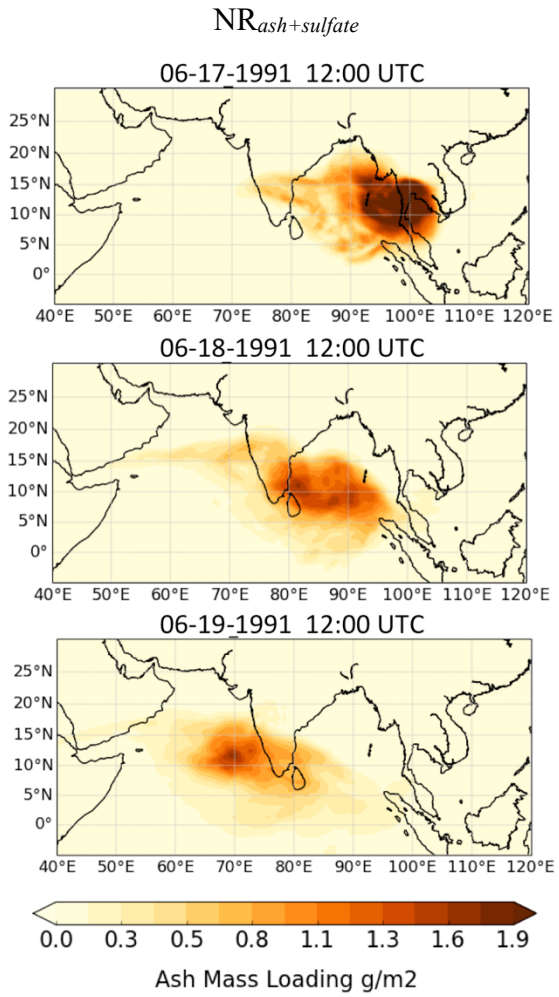

Figure 4.14 Transport of volcanic ash in the nature runs. The panels show the dispersion of ash in $NR_{ash+sulfate}$. The panels show the vertically integrated column loading of ash at 12:00UTC on June 17th, 18th, and 19th.

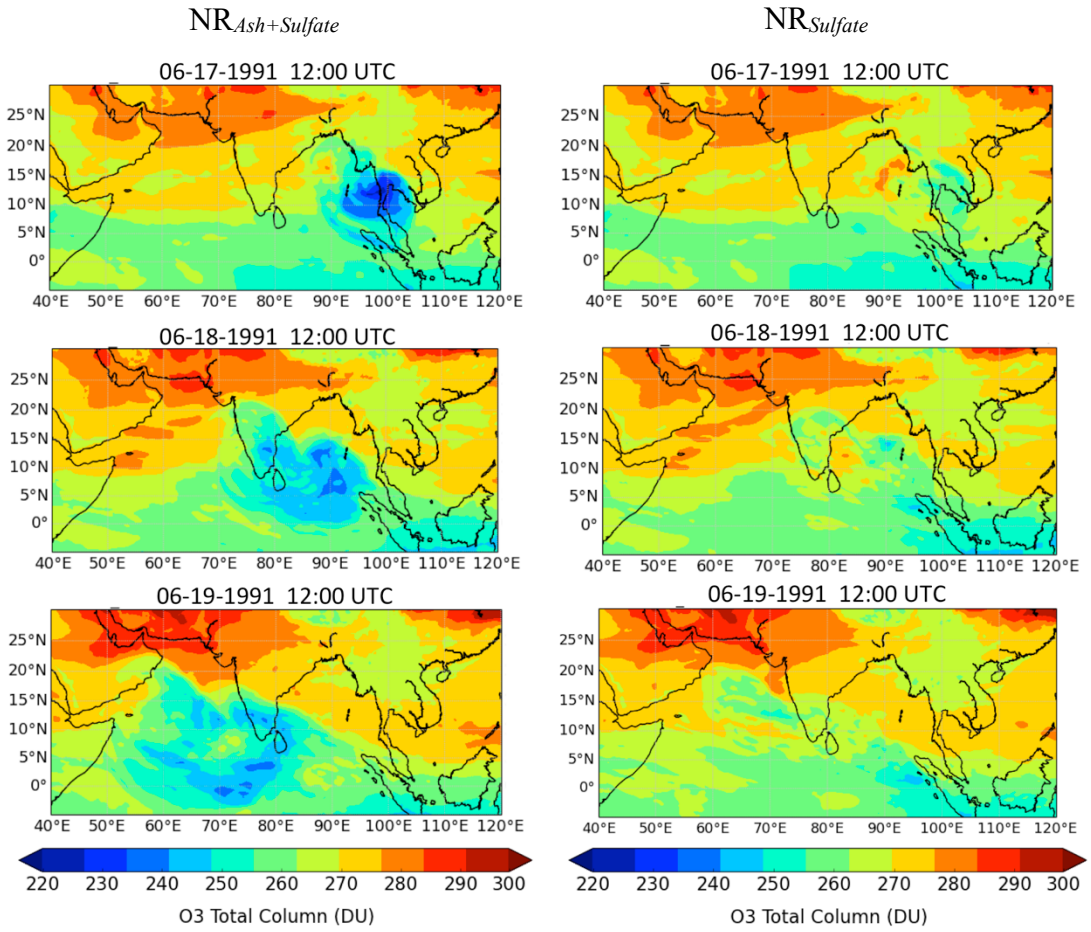

Figure 4.15 Distribution of column ozone in the nature runs. The left panels show the atmospheric ozone in $NR_{ash+sulfate}$, with $NR_{sulfate}$ shown in the right panels. The panels show the vertically integrated column loading of ozone at 12:00UTC on June 17th, 18th, and 19th.

The differences between the two nature runs can be better understood by investigating the role of volcanic ash in the $NR_{ash+sulfate}$ simulation. Since these model simulations are run "online", the volcanic ash induced radiative lofting of the volcanic cloud in $NR_{ash+sulfate}$. This lofting can be seen in the vertical component of the wind field, ω. To look exclusively at the influence of radiative lofting on the wind fields, the winds field differences between the nature run with ash, $NR_{ash+sulfate}$, and the nature run without ash, $NR_{sulfate}$, are investigated. Figure 4.16 shows the difference between the ω fields from $NR_{ash+sulfate}$ and $NR_{sulfate}$, for a cross-section at 15° latitude and from 40° to 120° longitude, the same longitude range as in the plots shown in

Figure 4.12 - Figure 4.15. The differences in the ω fields show increased vertical velocities at and slightly below the location of the volcanic SO_2 cloud, Figure

4.6c, in the range of 19 km to 21 km. The increased vertical velocities in $NR_{ash+sulfate}$ entrained ozone-poor air masses upwards, from the troposphere into the stratosphere. This is demonstrated in Figure 4.16a, where ozone-poor air masses from lower altitudes are pushed upwards, displacing ozone-rich air masses. The lofting of ozone-poor air upwards with the volcanic cloud results in a reduction of the total vertical column of ozone observed within the volcanic plume, compared to total vertical column ozone outside of the plume. This is exactly what was observed in Figure 4.15.

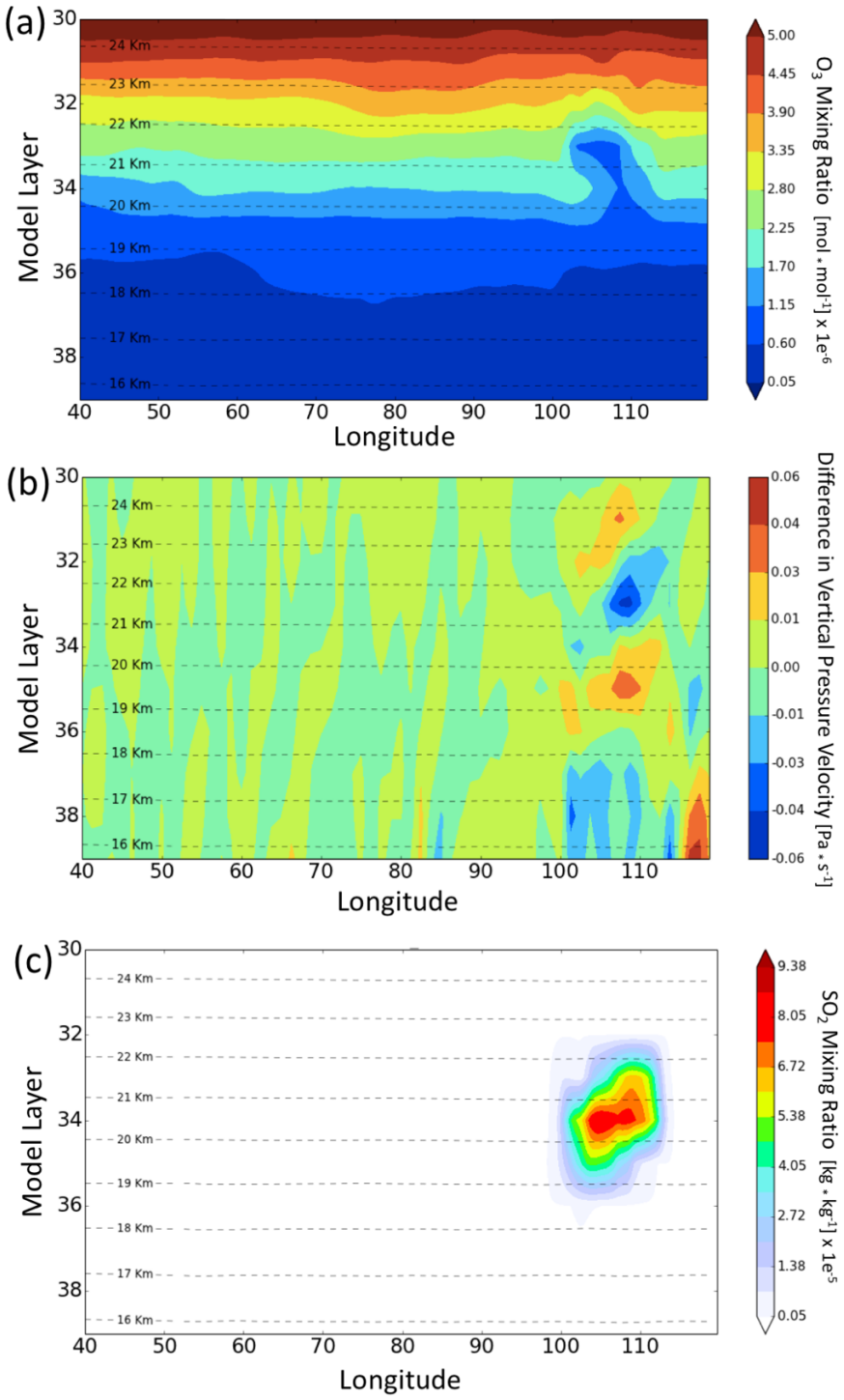

Figure 4.16 Upward entrainment of ozone poor air. A cross-section of the ozone field in the $NR_{ash+sulfate}$ run is shown in (a). Panel (b) shows the difference in vertical wind velocities between the $NR_{ash+sulfate}$ and $NR_{sulfate}$ runs. A vertical cross-section of the SO_2 cloud is shown in (c). All cross-sections are shown for the 15° latitude band, on June 16th at 15:00UTC, the beginning of the nature runs at fine horizontal resolution.

In addition to the lofting associated with the volcanic cloud, the ω differences also show an increased downward vertical velocity at altitudes above the volcanic cloud, followed by increased vertical velocities at even higher altitudes (23 km - 24 km). The differences in the vertical wind fields do not persist for long, by June 17th there are only minor ω differences associated with the volcanic cloud.

The adjustment to the vertical velocities caused by volcanic ash radiative heating further induced a modification to the horizontal wind fields, u and v. The modifications to the horizontal wind fields produced a more lasting adjustment to the meteorology that influenced the volcanic cloud transport differences observed in Figure 4.12 - Figure 4.15. In FiguresFigure 4.17Figure 4.18, the differences in the horizontal wind fields, u and v, between the $NR_{ash+sulfate}$ and $NR_{sulfate}$ are shown for the model layers at approximately 18 km - 19 km and 21 km - 22 km. At the 18km - 19 km layer, the ash lofting induces a cyclonic flow consistent with a low pressure located below the volcanic cloud. The cyclonic system follows along with the volcanic cloud throughout the simulation, with dissipating strength and increasing extent. Conversely, at the 21-22 km layer, the lofting induces an anticyclonic flow associated with a high-pressure system. The anticyclonic flow similarly follows along with the volcanic cloud, also dissipating in strength and increasing in extent.

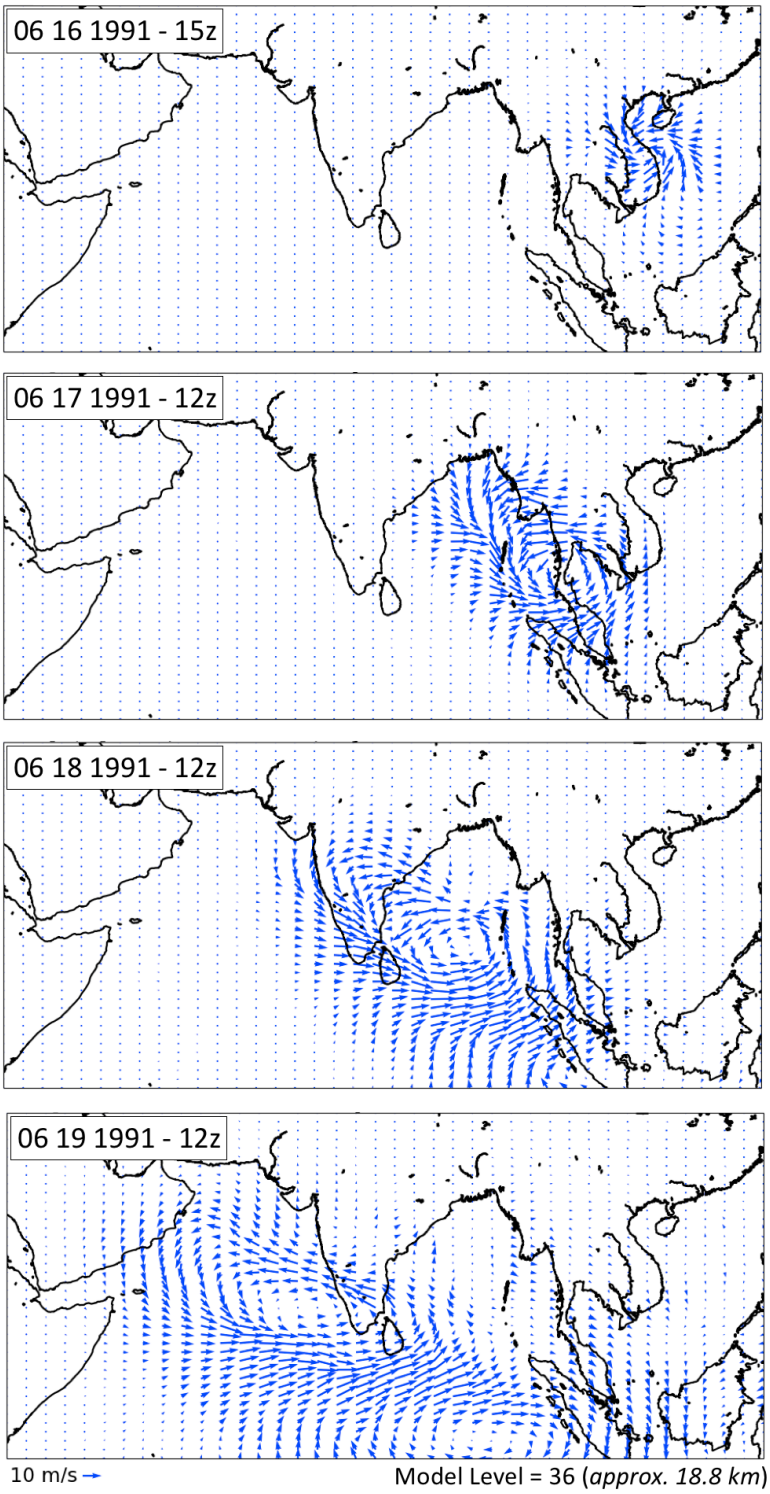

Figure 4.17 Influence of ash lofting on horizontal wind fields. The differences between the $NR_{ash+sulfate}$ and $NR_{sulfate}$ (u,v) components of the wind field are shown, for model level = 36 (approximately 18.8 km). Panels are shown for June 16th 15:00UTC, 17th 12:00UTC, 18th 12:00UTC, and 19th 12:00UTC.

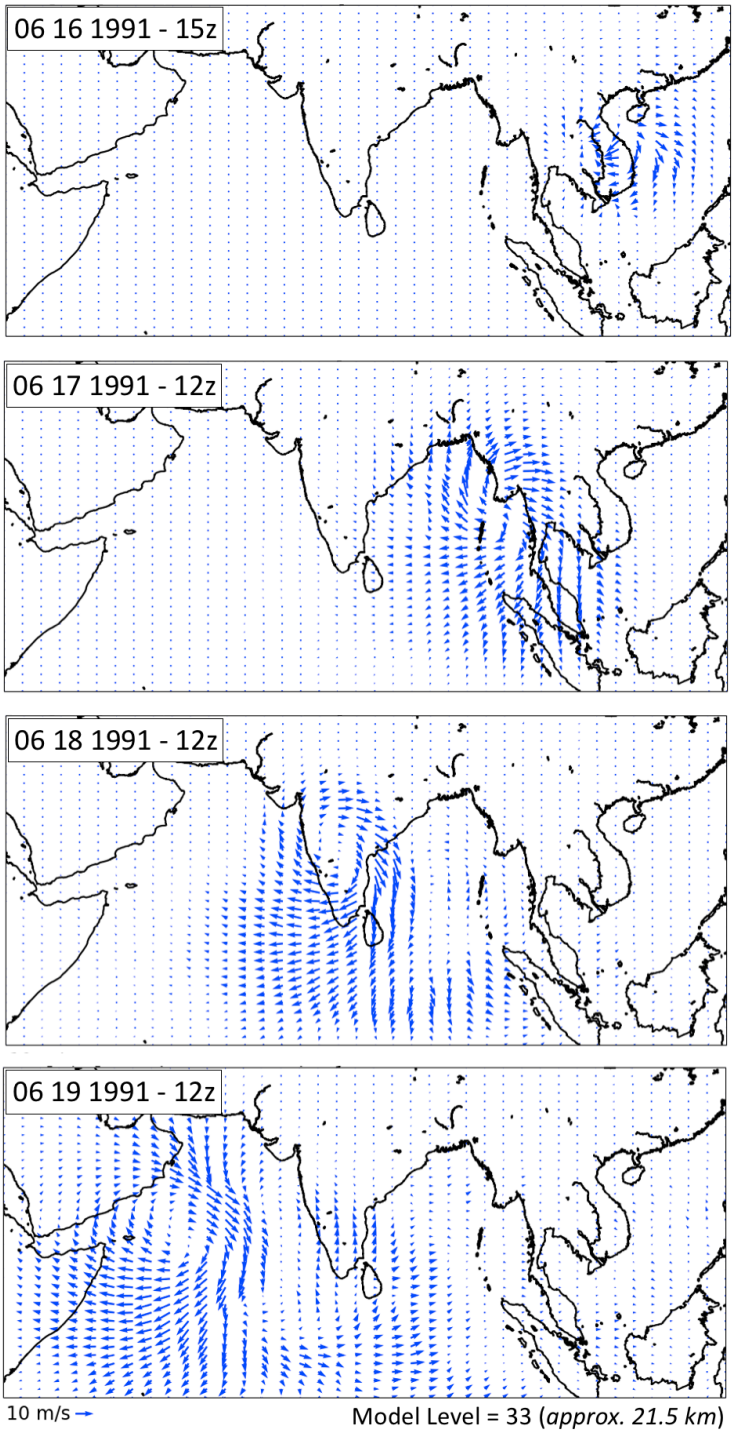

Figure 4.18 Influence of ash lofting on horizontal wind fields. The differences between the $NR_{ash+sulfate}$ and $NR_{sulfate}$ (u,v) components of the wind field are shown, for model level = 33 (approximately 21.5 km). Panels are shown for June 16th 15:00UTC, 17th 12:00UTC, 18th 12:00UTC, and 19th 12:00UTC.

The anticyclonic flow appears to have induced an upper level downward ω flow between 21 km – 23 km, as seen in Figure 4.16. This upper-level downward flow has the effect of limiting the lofting potential of the volcanic cloud. The simulations of SO_2 in the two nature runs yield different transport patterns, see

Figure 4.12. The SO_2 plume in $NR_{ash+sulfate}$ rotates in an apparent anticyclonic motion, similar to what was observed in the wind field difference maps, Figure Figure 4.18. Thus, the ash radiative lofting did indeed cause the differences between the SO_2 transport in the nature runs.

Figure 4.12 also seems to suggest less SO_2 in $NR_{ash+sulfate}$. This is not the case, as integration of the columns reveals (Figure 4.19). I understand the difference as a result of (a) a more dispersed (sheared) plume in $NR_{ash+sulfate}$ and (b) vertical displacement of the plume to higher altitudes in $NR_{ash+sulfate}$ which have less OH and thus less destruction of SO_2. This also suggests less sulfate in $NR_{ash+sulfate}$, Figure 4.19b.

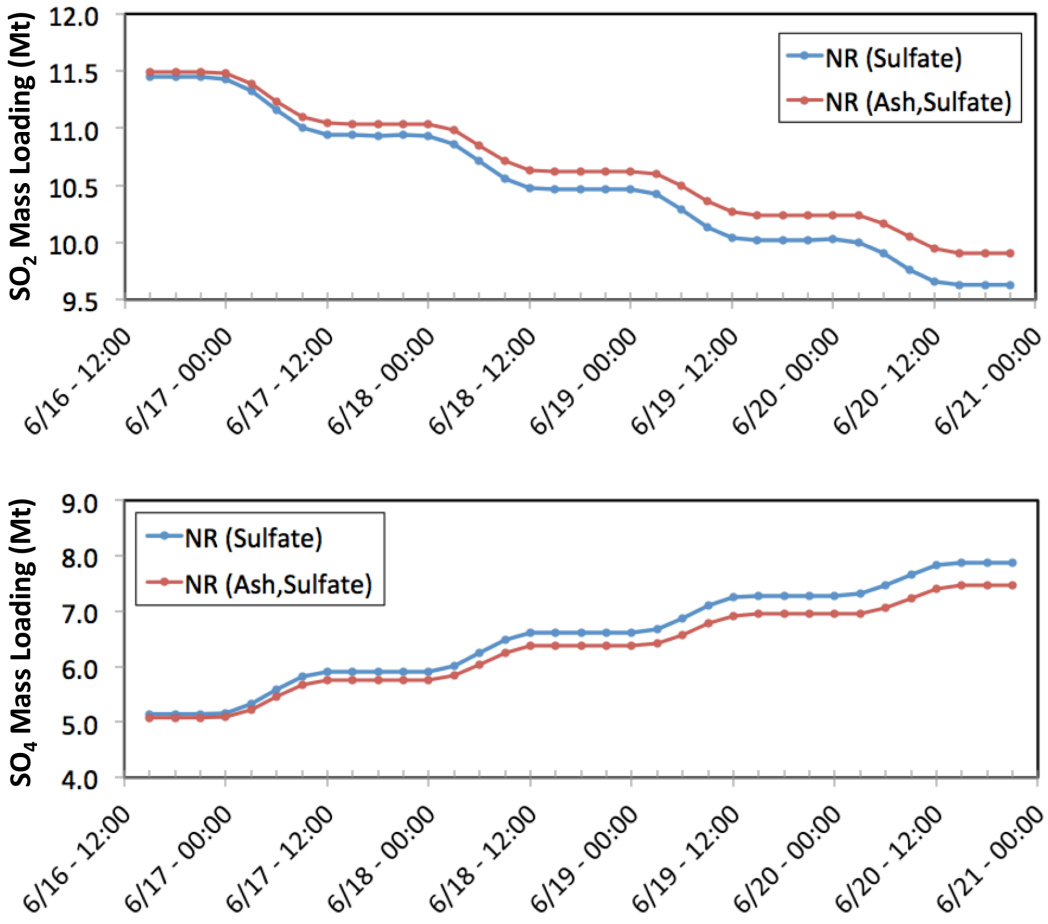

Figure 4.19 Loss and production of SO_2 and sulfate aerosols. The evolution of the SO_2 total mass is shown in the top panel, for both nature runs. The sulfate aerosol total mass is similarly shown in the bottom panel

Much of the discussion thus far has focused on the ash induced lofting, but sulfate aerosols can also loft volcanic clouds. The vertical structure and subsequent lofting of the SO_2 clouds is shown in Figure 4.20. Both nature runs initialized the volcanic cloud evenly between 18 km - 21 km. By June 16th at approximately 15z (24 hours after the eruption), the SO_2 cloud was vertically distributed between 20 km – 23.5 km in the $NR_{ash+sulfate}$ simulation and 19 km – 22 km in $NR_{sulfate}$. By the end of the simulation on June 20th at 12z, the SO_2 cloud in $NR_{sulfate}$ had lofted upwards to 24 km, but most of the mass remained centered around 19 – 23.5 km. The $NR_{ash+sulfate}$

SO_2 cloud lofted to 22.5 km – 26 km by June 20th 12z. When compared to the initialization altitude, $NR_{sulfate}$ SO_2 cloud lofted 1 km – 1.5 km and $NR_{ash+sulfate}$ lofted about 4 km across the first 5 days after the eruption.

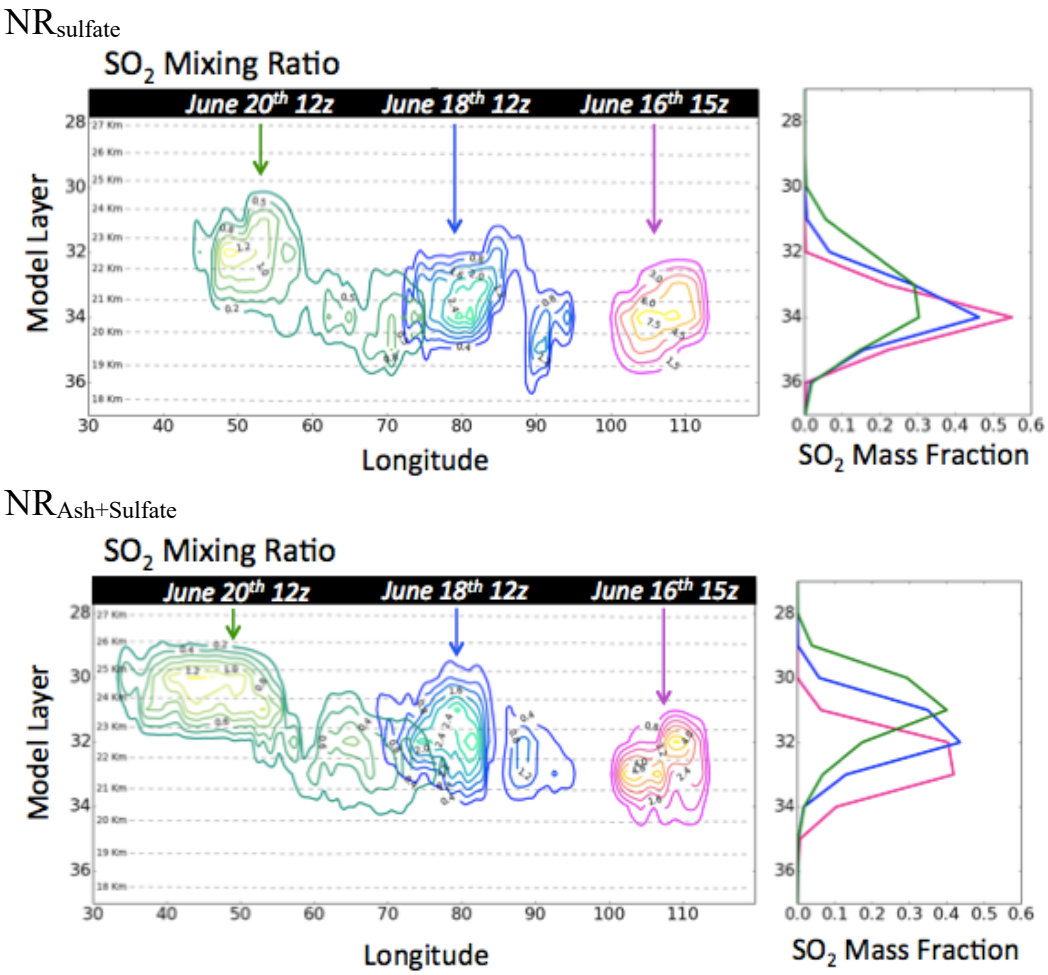

Figure 4.20 Lofting of SO_2 in the nature runs. The left panels show cross-section through the SO_2 plume at three different times: June 16th 15:00UTC (magenta contours), June 18th 12:00UTC (blue contours), and June 20th 12:00UTC (green contours). The right panels show the vertical mass distributions of the entire SO_2 plume, for the same times and associated colors as in the left panels. The top panels show SO_2 profiles for $NR_{suflate}$ and the bottom for $NR_{ash+sulfate}$.

4.4 Observation Simulator

4.4.1 Setup

The observation simulator serves to construct synthetic observable quantities based on input from the nature run. For the OMPS SO_2 Retrieval OSSE, the volcanic cloud nature runs provide profiles of gases and aerosols. The observation simulator is primarily driven by the radiative transfer model VLIDORT [*Spurr, 2006*], which is used to simulate synthetic TOA BUV radiances, the input for the OMPS SO_2 retrieval. The results of the nature run are pre-processed before they can be used as input to VLIDORT. The nature run preprocessing consists of (1) regridding results onto the spatial location of the OMPS pixels using a sample orbit, (2) computing optical properties of the simulated aerosols, and (3) computing the column ozone and SO_2 extinction as observed by the OMPS instrument. VLIDORT is then used to generate TOA BUV radiances at 11 wavelengths [312 nm, 317 nm, 322 nm, 325 nm, 331 nm, 340 nm, 354 nm, 360 nm, 380 nm, 388 nm, 471 nm]. However, further discussion focuses on results at the wavelengths used by the OMPS SO_2 retrieval [317 nm, 331 nm, 340 nm, 380 nm].

The nature run results are interpolated to orbital swaths using OMPS observations from June 16th - 19th 2016. A select number of orbital files from this time range where used templates, providing geolocation information observation simulator. The date information in these OMPS orbital files are altered to reflect measurements at the time of the nature runs, i.e. during 1991 instead of 2016. A bi-linear interpolation scheme is used to interpolate the nature run parameters across space and time to the central point of each OMPS pixel within each of the OMPS

orbital files used as templates in this study. This results in a set of nature run orbital files which complement each of OMPS orbital files used in the experiment, containing the profiles of parameters simulated in the nature runs. The OMPS observations also provide the satellite viewing geometry, needed by VLIDORT to construct TOA radiances at the instrument viewing angles.

The optical properties of the ash and sulfate aerosols are quantified in terms of their mass extinction efficiency, single scattering albedo, asymmetry factor, and Legendre polynomial moments of the polarized phase function. These properties are estimated from lookup tables computed from the Mie theory code of Wiscombe [*1980*], for sulfate aerosols, and non-spherical optics after Colarco et al. [*2014*], for volcanic ash. The optical properties are computed for each of the ash and sulfate size bins and then integrated across each species. For each bin, a log-normal size distribution is assumed. The optical properties are computed for the 4 wavelengths used in the OMPS SO_2 retrieval.

Simulating the TOA radiances requires an estimate of the Earth's surface albedo. In this study the TOMS UV surface albedo climatology is used, which is also used in the OMPS Aerosol Index retrieval [*Flynn et al., 2014*]. The TOMS UV surface albedo climatology is compiled at wavelengths: [331 nm, 340 nm, 354 nm, 360 nm, 378.5 nm, 380 nm] which are assigned wavelengths used in this study by a "nearest neighbor" approach.

The nature runs simulate profiles of SO_2 in the atmosphere which are used by the observation simulator to generate synthetic BUV TOA radiances, but this is not necessarily the same as what the OMPS instrument would observe. The physical

construction of the instrument affects the amount of light that the instrument sensors are able to view. The OMPS slit function is used to understand the relationship between radiance measurements by the instrument and the magnitude of the radiance actually viewable by the instrument sensor as a function of nominal wavelength. In this analysis, the SO_2 and ozone absorption cross-sections are used to compute the extinction due to the total column SO_2 and O_3 from the nature runs. The total column SO_2 and ozone extinction is then convolved with the OMPS slit function for the 4 wavelengths used in this study.

In the previous section, two nature runs were performed to contrast an eruption with and without volcanic ash. The observation simulator can further discriminate different volcanic cloud scenarios by excluding various components of the nature run from the observation simulator. For example, for both nature runs, the observation simulator can ignore the volcanic ash and sulfate aerosols to create "aerosol free" synthetic radiances. Removing the aerosols in this fashion provides a baseline of synthetic radiances that are more in line with the retrievals assumption, providing a sort of "best case" scenario in favor of the retrieval. The various observation simulator output scenarios are shown in Table 4.3.

Table 4.3 Observation Simulator Input Conditions

	Observation Simulator		
	Ash + Sulfate	*Sulfate*	*No Aerosols*
Nature Run $_{Ash+Sulfate}$	Ash, Sulfate, SO_2, O_3	Sulfate, SO_2, O_3	SO_2, O_3
Nature Run $_{Sulfate}$		Sulfate, SO_2, O_3	SO_2, O_3

4.4.2 Results

Trace gases and aerosols have different and sometimes competing effects to the TOA BUV radiance. In the OMPS OSSE, these effects are explored by comparing the results of the observation simulator under the various input conditions shown in Table 4.3. Both ash and sulfate aerosols are only simulated in $NR_{ash+sulfates}$, so only this nature run is used to investigate the relative effects of ash and sulfate aerosols on the TOA BUV radiances. The effects of the SO_2, sulfate and ash on the TOA BUV radiance specifically at 317 nm are shown in Figure 4.21. The aerosol free radiances in Figure 4.21a show a reduction is radiance due to absorption by the volcanic SO_2. In order to look at the sulfate aerosol contribution to the radiance, the radiance difference for $OS_{sulfate} - OS_{No\ Aerosols}$ is shown in Figure 4.21b. The radiance difference shows that sulfate aerosols have the effect of increasing the radiance. This behavior is expected since enhanced scattering should increase the observable backscatter radiance and sulfate aerosols are largely scattering aerosols. The effect of volcanic ash on the radiance is shown in Figure 4.21c, showing the radiance difference $OS_{ash+sulfate} - OS_{sulfate}$. This radiance difference shows that volcanic ash contributes to a reduction in the TOA BUV radiance. This behavior is opposite of that seen by sulfate aerosols but is consistent with the absorbing properties of the ash, and thus produces a reduction in the backscatter radiance. These results suggest that sulfate aerosols and volcanic ash have competing effects, where the sulfates tend to increase the radiance while the ash acts reduce the radiance.

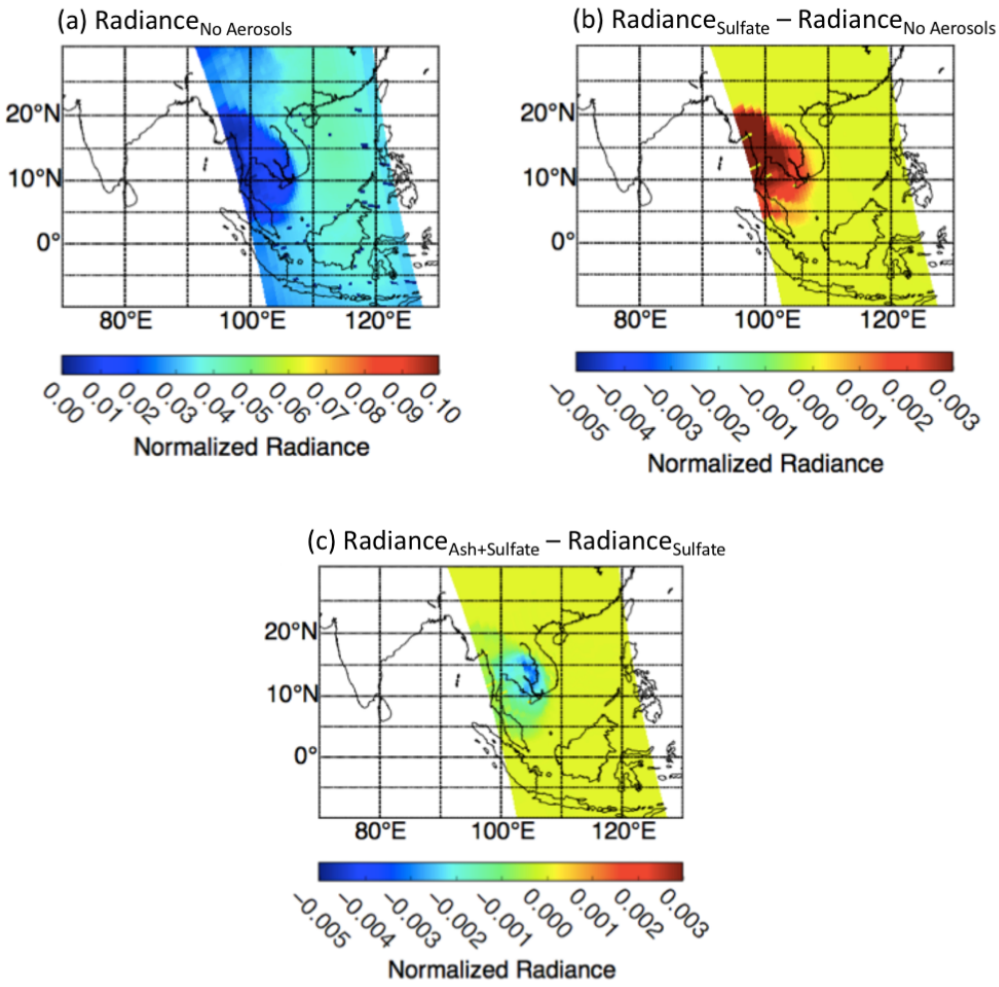

Figure 4.21 Synthetic BUV TOA radiances at 317nm. The TOA normalized radiances for NRash+sulfate for the no aerosols case is shown in (a). The contribution of the sulfate aerosols to the radiances is shown in (b), as the normalized radiance difference between the sulfate minus no aerosols run. The ash contribution is then shown in (c) as the normalized radiance difference between ash+sulfate minus sulfate.

Individual pixels are investigated in order to take a closer look at how the radiance changes at increasing SO_2 column loadings, and across the four wavelength channels used in the OMPS SO_2 retrieval. The pixels of interest are plotted in Figure 4.22. For each of these pixels, the $OS_{No\ Aerosols}$, $OS_{sulfate}$ and $OS_{ash+sulfate}$ radiances are plotted. Once again, the radiances are generated using inputs from

$NR_{ash+sulfate}$. Similar to Figure 4.21, the difference between the $OS_{No\ Aerosols}$ and $OS_{sulfate}$ curves represent the contribution of the sulfates to the radiance, and the difference between the $OS_{sulfate}$ and $OS_{ash+sulfate}$ curves represents the contribution of the ash to the radiance. The radiance curves for three different SO_2 column loadings are shown in Figure 4.22, for a low column SO_2 loading (DU = 5), medium column SO_2 loading (DU = 54), and high column SO_2 loading (DU = 176).

At low column SO_2 loading, Figure 4.22d, the radiance curves are all generally the same. This makes sense given that the ash and sulfate aerosols generally travel with the bulk mass of the volcanic cloud, so lower column mass pixels mainly reflect Rayleigh scattering and gas absorption. The radiance curve show more deviation at the medium column loading, Figure 4.22e. As previously seen in the Figure 4.21, the sulfate aerosols tend to elevate the radiances, though at all wavelength channels. Similarly, the ash tends to reduce the radiance across all wavelength channels. The net effect of the ash and sulfate aerosols results in a radiance increase across all OMPS channels, when compared to the no aerosols case. At the high column SO_2 loading, Figure 4.22 f, ash and sulfate aerosols produce similar responses as seen in the medium column loading pixel but yield a different net effect. In the high column loading pixel, the competing effects of the ash and sulfate aerosols yield net radiances that are actually lower than the no aerosol radiances, at the 331 nm and 340 nm channels. This result is important because it highlights that the effects of sulfates and ash can result in enhanced or reduced TOA BUV radiances, when compared to the no aerosol radiances. This result implies that ash and sulfate aerosols could potentially increase or decrease the amount of SO_2 derived by OMPS

SO_2 retrieval, by altering the amount SO_2 absorption the retrieval assumes to observe.

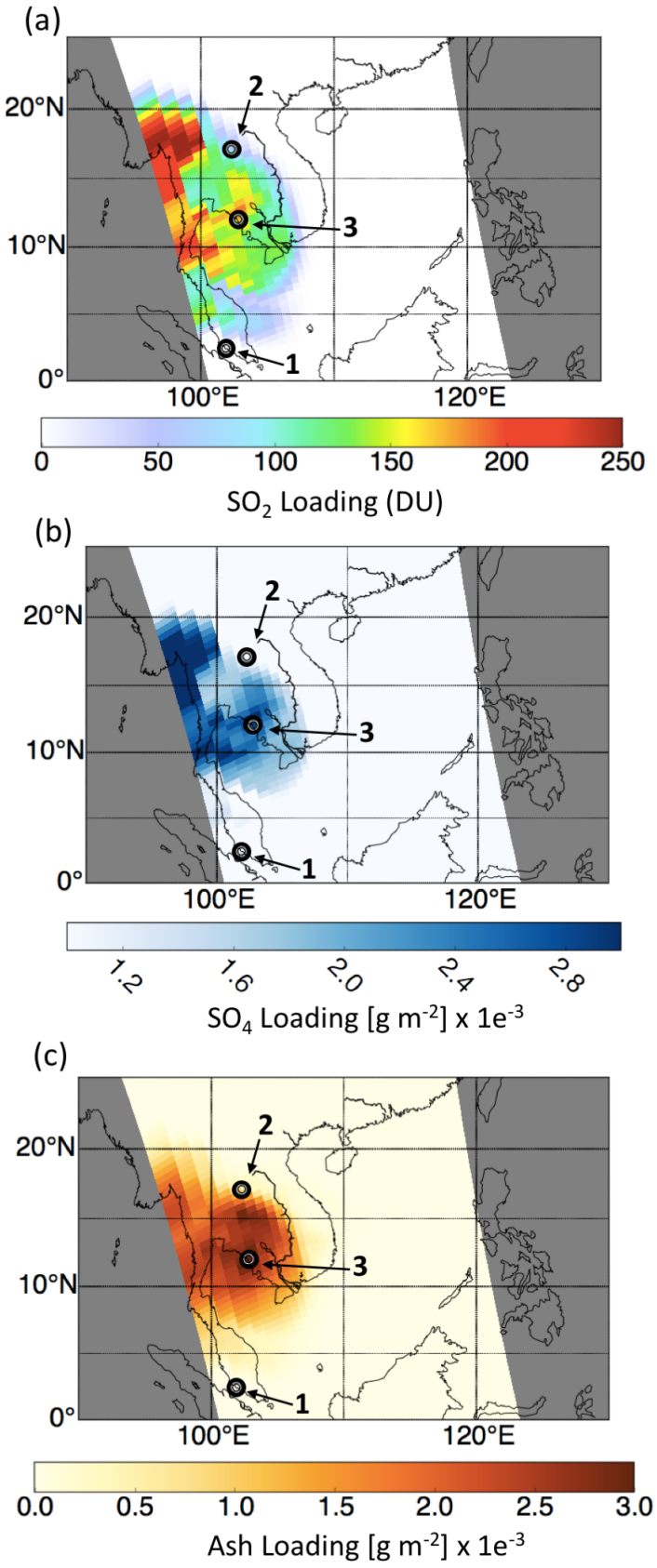
(a)
20°N
10°N
0°
100°E
120°E
1
2
3
0
50
100
150
200
250
SO2 Loading (DU)
(b)
20°N
10°N
0°
100°E
120°E
1
2
3
1.2
1.6
2.0
2.4
2.8
SO4 Loading [g m-2] x 1e-3
(c)
20°N
10°N
0°
100°E
120°E
1
2
3
0.0
0.5
1.0
1.5
2.0
2.5
3.0
Ash Loading [g m-2] x 1e-3

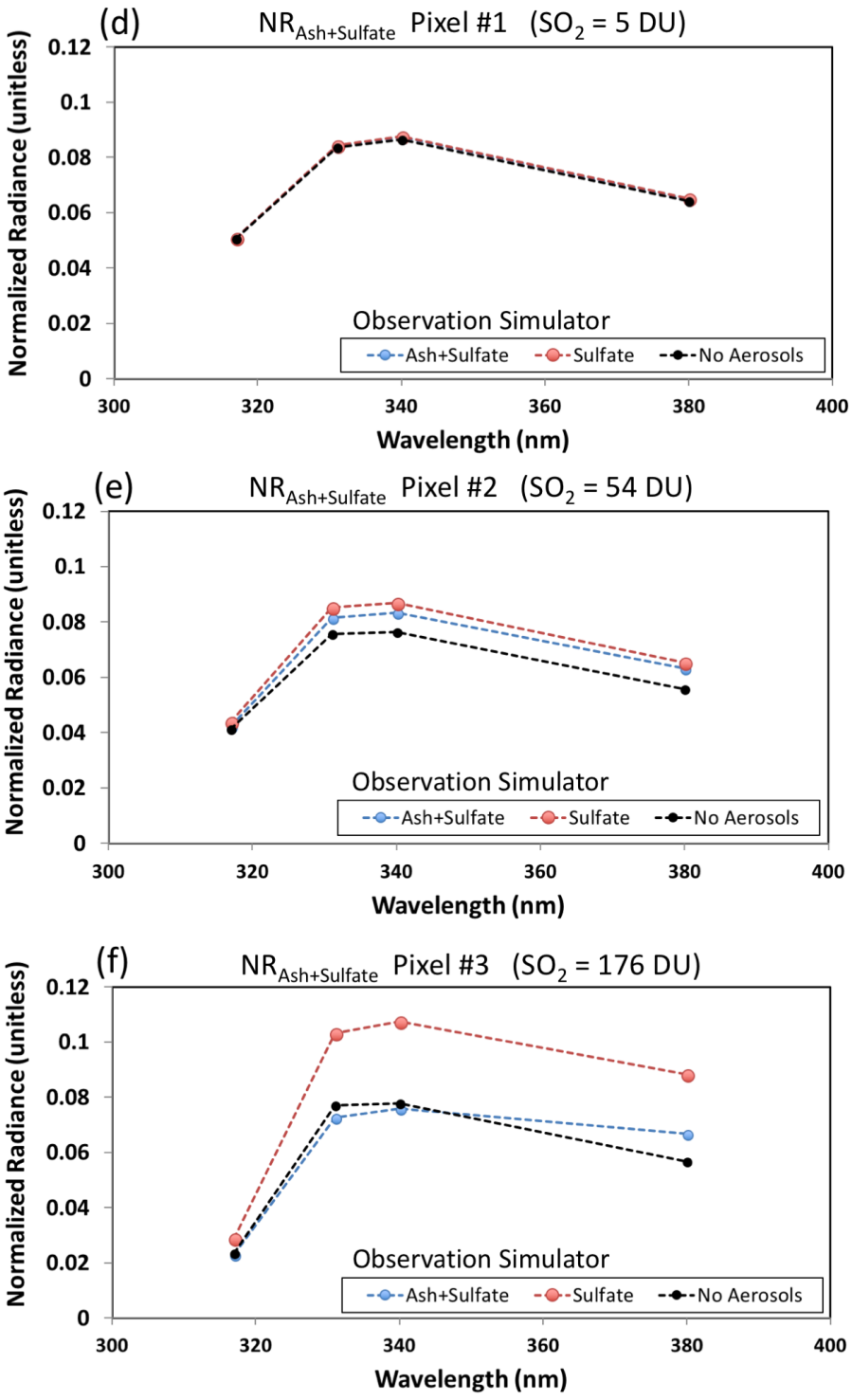

Figure 4.22 Synthetic radiances across OMPS wavelengths. The SO_2, SO_4, and ash loading three pixels is shown in a,b,c. In d,e,f the normalized radiances of each pixel for different OS cases are shown. The normalized radiances are shown at 317 nm, 331 nm, 340 nm, 380 nm. The radiances are shown for the no aerosols case (black), sulfate (red), and ash+sulfate (blue).

4.5 Experiment Results

Synthetic BUV TOA radiances are generated for both Nature Runs detailed in Section 4.3 and the various Observations Simulation conditions from Table 4.3. The OMPS SO_2 retrieval is processed from synthetic radiances for June 17th, 18th, and 19th. Figure 4.23 shows the OMPS orbits that were generated for this study.

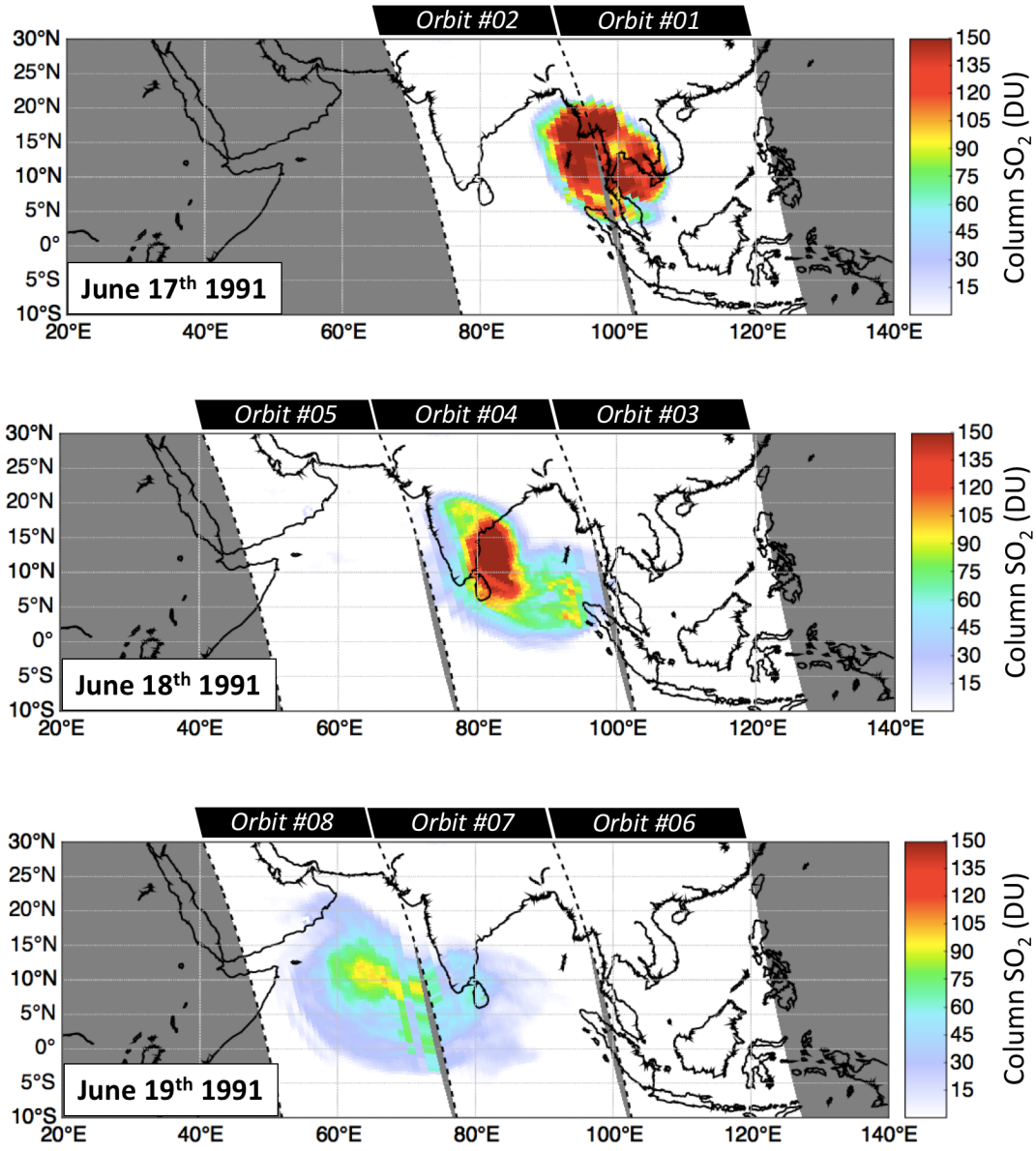

Figure 4.23 OMPS SO_2 orbits from synthetic radiances. The maps above show all the OMPS SO_2 orbits generated for this study. The OMPS SO_2 displayed above were generated for $NR_{Ash+Sulfate}$, OMPS SO_2 orbits were also generated for $NR_{sulfate}$.

The accuracy of the OMPS SO_2 retrieval is evaluated by comparing the column SO_2 estimated by the OMPS SO_2 retrieval, or *retrieval SO_2*, with the nature run column SO_2 values used to generate the synthetic radiances, or *model SO_2*. I further contrast the cases where no aerosols have been included in the synthetic

radiance calculation, $OS_{No\ Aerosols}$, with the cases with sulfate aerosols, $OS_{Sulfate}$, and the cases with ash and sulfate aerosols, $OS_{Ash+Sulfate}$. The results begin with an analysis of SO_2 generated by the OMPS SO_2 retrieval for June 17th, then expand to consider the OMPS retrieval SO_2 generated across all days.

4.5.1 OMPS Orbit #01

4.5.1.1 Observation Simulator with No Aerosols

OMPS orbit #01 on June 17th intersects the volcanic plume the earliest in the simulation, sampling the simulated SO_2 cloud at relatively high concentrations. The analysis starts with this orbit as it provides synthetic radiances under a large range of SO_2 column concentrations, providing a large sampling space to evaluate the OMPS SO_2 retrieval. For orbit #01, the OMPS SO_2 retrieval is processed multiple times, using synthetic radiances that were generated from both nature runs, and under the observation simulator conditions: $OS_{No\ Aerosols}$, $OS_{sulfate}$ and $OS_{ash\ +\ sulfate}$.

The OMPS SO_2 retrieval generally assumes an aerosol-free observation, so the "no aerosols" condition should provide synthetic radiances that best match the conditions assumed by the OMPS SO_2 retrieval. In Figure 4.24, the input from both nature runs are considered, but the observation simulator assumes an aerosol free atmosphere, $OS_{No\ Aerosols}$. The nature run SO_2 is shown in Figure 4.24a for $NR_{ash+sulfate}$ and Figure 4.24d for $NR_{sulfate}$. The accompanying output SO_2 from the OMPS retrieval is shown in Figure 4.24b and e, for $NR_{ash+sulfate}$ and $NR_{sulfate}$ respectively. In both nature run scenarios, the OMPS retrieval generally reproduces the SO_2 from the nature runs that were used as input to the synthetic radiances. Note

that, as shown previously, the $NR_{sulfate}$ produced higher SO_2 column concentrations then in NRash+sulfate. Comparison of the retrieval SO_2 to the model SO_2 is further demonstrated in the 1:1 plots in Figure 4.24 c and f.

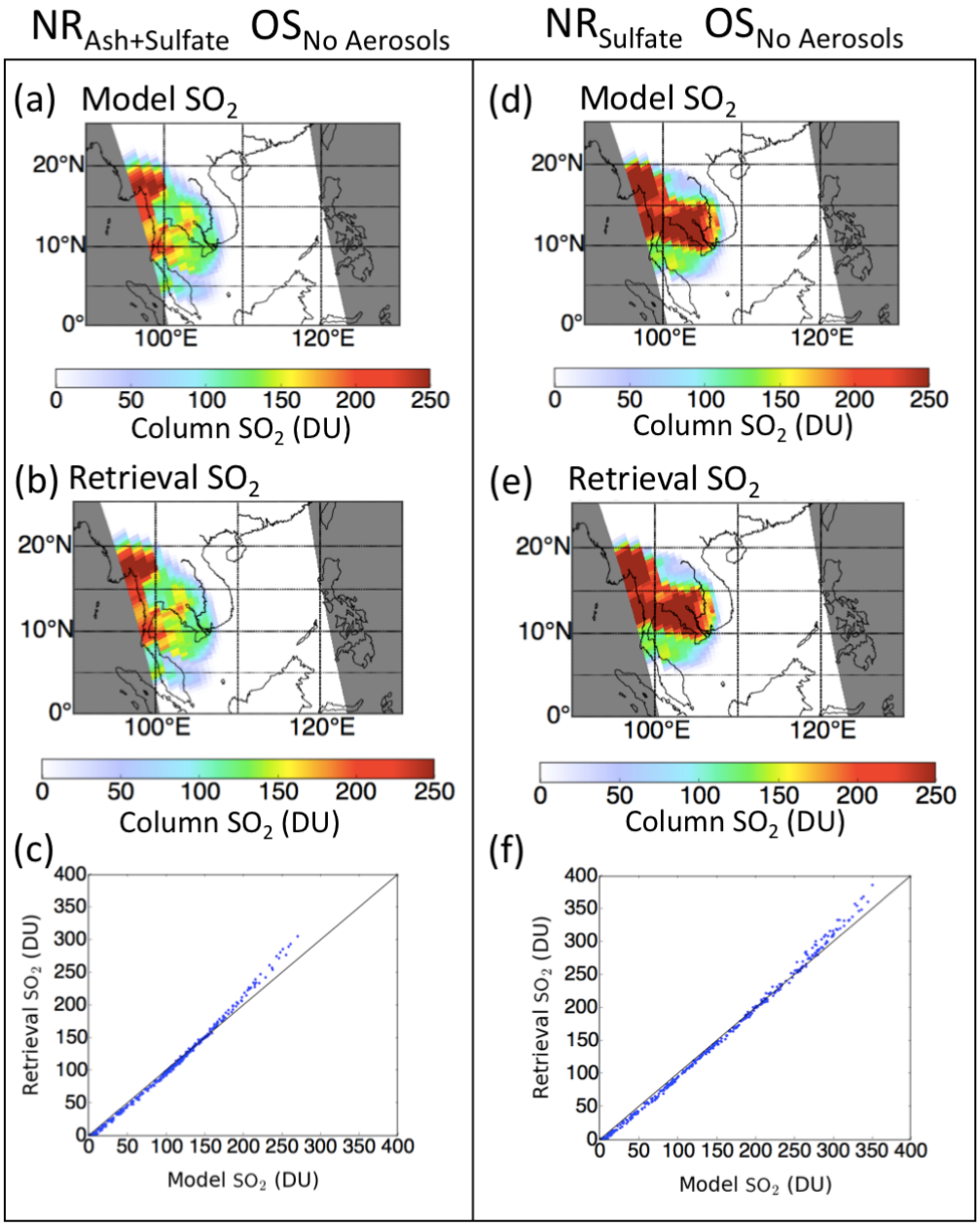

Figure 4.24 OMPS SO_2 from aerosols-free radiances. The NR SO2 is shown for NRash+sulfate (a) and NRsulfate (d). The OMPS retrieval given the NRash+sulfate is shown in (b) and for NRsulfate in (e). Scatter plots of the NR SO_2 and OMPS SO_2 are shown in the bottom panels, for the NRash+sulfate (c) and NRsulfate (f).

At relatively low column SO_2 concentrations, the OMPS retrieval closely reproduces the nature run SO_2. The 1:1 comparisons show a slight bias at for the OMPS retrieval to underestimate the nature run SO_2 column concentrations by roughly 5 DU for both nature runs, but this bias acts as a constant offset at low concentrations. For both nature run scenarios, there is a maximum column concentration where the OMPS retrieval begins to increasingly overestimate the SO_2 column. In the $NR_{sulfate}$, the OMPS retrieval overestimation starts to occur above 250 DU - 300 DU. The overestimation begins at much lower column concentrations in the $NR_{ash+sulfate}$, around 150 DU.

The primary differences between the nature run inputs for the $OS_{No\ Aerosols}$ scenario are the in-plume ozone levels (lower in $NR_{ash+sulfate}$) and the SO_2 plume height (higher in the $NR_{ash+sulfate}$). Both of these differences affect the OMPS SO_2 retrieval. Ozone absorption occurs at the same wavelengths as SO_2 absorption, so the retrieval must partition the observed radiance reductions to either SO_2 or ozone. Incorrect partitioning can produce either more or less SO_2 in the OMPS retrieval. As previously mentioned, the OMPS retrieval assumes a center of mass altitude for the SO_2. For this study, the OMPS SO_2 retrieval assumed a center of mass altitude of 18 km. The altitude provides information about the degree of attenuation expected for the radiances. When the OMPS retrieval underestimates the SO_2 plume altitude, it overestimates the atmospheric attenuation and thus overestimates the SO_2 column concentration. In this case, the SO_2 plume in the $NR_{ash+sulfate}$ run has lofted a few kilometers higher in than in $NR_{sulfate}$, so the OMPS retrieval should overestimate the SO_2 column. However, even given these differences

in the ozone fields and SO_2 plume altitudes, for moderate and low SO_2 column densities there is good agreement between the model and retrieval. This agreement demonstrates the ability of the OMPS SO_2 retrieval to reproduce the model SO_2 under the OMPS SO_2 OSSE framework.

4.5.1.2 Observation Simulator with Sulfate Aerosols

The setup of the aerosol free analysis in the previous section is altered to included sulfate aerosols in the observation simulator, $OS_{sulfate}$. In Section 4.4, sulfate aerosols were shown to significantly affect the BUV TOA radiances. The influence that sulfate aerosols have on the OMPS SO_2 retrieval are shown in Figure 4.25. The OMPS retrieval SO_2 maps are shown in Figure 4.25 a and c, which show that the OMPS retrieval has estimated less SO_2 than in the no aerosols OMPS retrieval in Figure 4.24 b and e, and the nature run inputs in Figure 4.24 a and d.

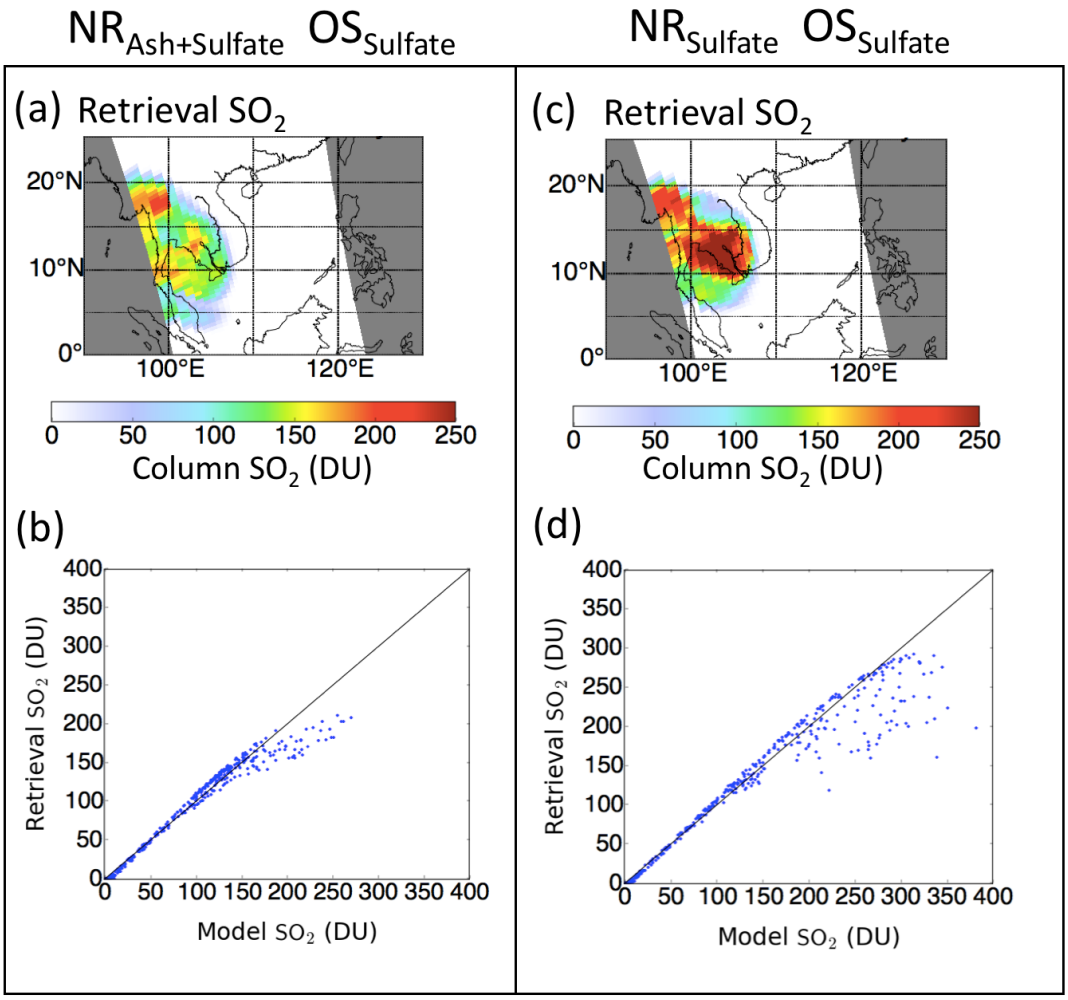

Figure 4.25 OMPS SO_2 from radiances with sulfate aerosols. The OMPS retrieval given the NRash+sulfate is shown in (a) and for NRsulfate in (c). Scatter plots of the NR SO_2 and OMPS SO_2 are shown in the bottom panels, for the $NR_{ash+sulfate}$ (b) and $NR_{sulfate}$ (d).

The 1:1 plots in Figure 4.25 b and d show that the SO_2 reduction observed in the OMPS retrieval maps is the result of saturation-like effect in the retrieval, where the SO_2 amount is increasingly underestimated at high model column SO_2 concentrations. In $NR_{ash+sulfate}$, the OMPS retrieval underestimation starts at around 150 DU - 200 DU, while this appears to occur bit higher in $NR_{sulfate}$, at around 200 DU. Below the point of retrieval saturation, the OMPS retrieval tends to reproduce

the nature run SO_2 following along the 1:1 line. At very low column concentrations, the OMPS retrieval tends to slightly underestimate the SO_2 amount, in a manner similarly seen in the no aerosols case. This generally occurs below 50 DU. Above 50 DU and below the point of retrieval saturation, the OMPS retrieval tends to slightly overestimate the SO_2 column concentrations. This overestimation also slightly increases with increasing model SO_2 amount.

The effects of sulfate aerosols on the OMPS retrieval can be summarized as (1) producing retrieval saturation at high SO_2 column densities and (2) causing the OMPS retrieval to slightly overestimate the SO_2 column densities by as much as 10 DU for $NR_{ash+sulfate}$ and 15 DU for $NR_{sulfate}$, when above 50 DU.

4.5.1.3 Observation Simulator with Ash and Sulfate Aerosols

The addition of volcanic ash to the synthetic radiances is now considered. In previous sections it was observed that volcanic ash tends to have the opposite effect on the BUV TOA radiances than sulfate aerosols. Volcanic ash reduced the magnitude the synthetic radiances at OMPS channels, though this effect was stronger for some channels than others. In the Figure 4.26, the effects of the volcanic ash on the OMPS SO_2 retrieval are shown. Recall that $NR_{ash+sulfate}$ is the only simulation with volcanic ash, so no results with $NR_{sulfate}$ are shown. The OMPS SO_2 map in Figure 4.26 a shows a slight reduction in the retrieval SO_2, when compared to the map from the only sulfate aerosols case, Figure 4.25 a.

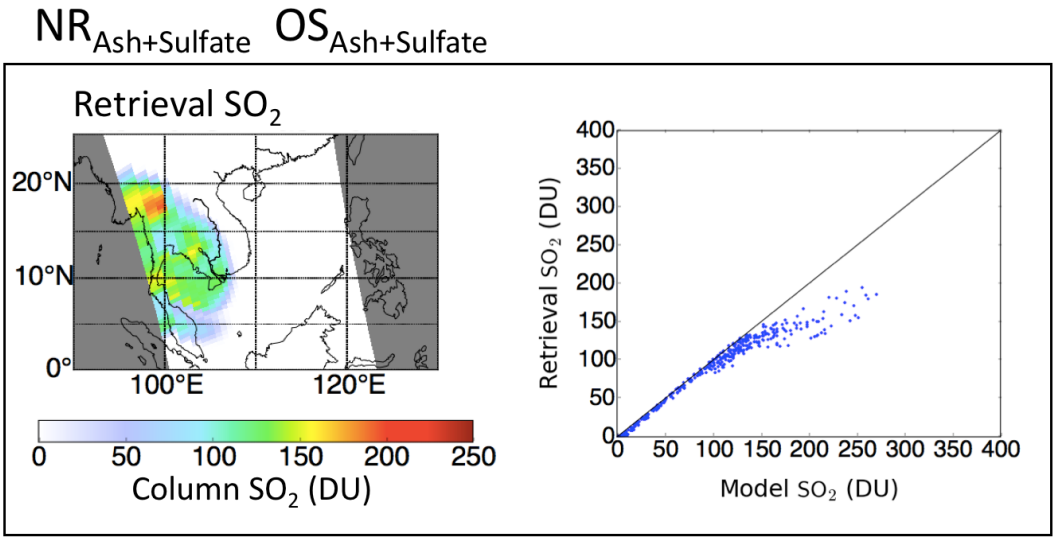

Figure 4.26 OMPS SO_2 from radiances with ash and sulfate aerosols. The OMPS retrieval given the NRash+sulfate is shown on the left and a scatter plot of the NR SO_2 and OMPS SO_2 is shown on the right.

The 1:1 plot in Figure 4.26 is similar to the 1:1 plot from the only sulfate aerosols case, Figure 4.25b with a few key differences. First, the point of saturation has decreased with the inclusion of volcanic ash, starting between 100 DU - 150 DU. Also, all the lower SO_2 amounts have now shifted slightly below the 1:1 line, showing that the OMPS retrieval is now underestimating the SO_2 column amount for all amounts. Interestingly, at low SO_2 values the effects of the ash and sulfate tend to combat each other and bring the retrieval SO_2 bias in back into rough agreement with the "no aerosols" case.

Investigating the relationship between sulfate aerosols and volcanic ash with the OMPS SO_2 retrieval suggests that the sulfate aerosols are responsible for the largest deviation in the OMPS retrieval from the nature run SO_2. Figure 4.27 shows maps of the sulfate aerosols and volcanic ash from the nature runs, and the ratio of OMPS SO_2 to the nature run SO_2. The ratio map in Figure 4.27 c shows that regions

with high sulfate aerosols concentrations show the largest saturation of the OMPS SO_2 retrieval. The regions of high ash also appear in regions where the OMPS SO_2 retrieval is underestimating the SO_2, but the correlation between high ash and retrieval saturation is not as clear. This result is consistent with the previous results, where the effects of sulfate aerosols and ash on the TOA BUV were compared. Figure 4.21 andFigure 4.22 showed that sulfate aerosols have a much larger effect on the radiances than volcanic ash. It makes sense that this relationship would results in a greater and lesser effect on the OMPS SO_2 retrieval, for sulfate aerosol and ash respectively.

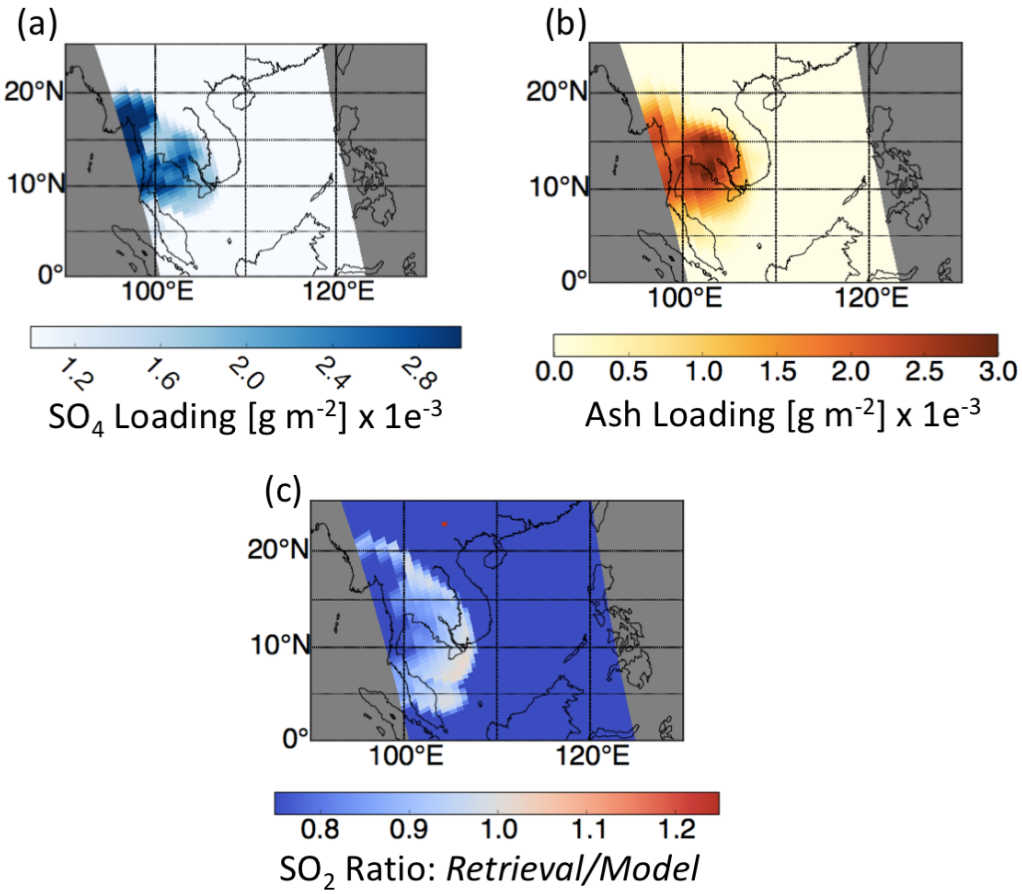

Figure 4.27 Maps of ash and sulfate and their relative effects. The sulfate aerosols and ash column loadings for $NR_{ash+sulfate}$ are shown in the top panels, left and right, respectively. A map of the ratio of OMPS SO_2 to NR SO_2 is shown in the bottom panel.

The analysis of orbit #01 has given some insights into how aerosols effect the OMPS SO_2 retrieval. It would appear that both volcanic ash and sulfate aerosols cause the OMPS retrieval to underestimate the SO_2 amount at high SO_2 column concentrations, causing a saturation-like effect. Aside from the high SO_2 column concentrations, the sulfate aerosols cause the retrieval to overestimate the SO_2 amount, while volcanic ash caused the retrieval to underestimate the SO_2 amount. Removing both the ash and sulfate aerosols from the radiance calculation

greatly improved the results of the OMPS SO_2 retrieval, coming into a better agreement with the nature run SO_2 amounts.

4.5.2 OMPS Viewing Angle

The previous section investigated the relationships between ash and sulfate aerosols and the accuracy of the OMPS SO_2 retrieval. However, the satellite viewing angles can also influence the OMPS retrieval which would be difficult to analyze from a single OMPS orbit. For instance, in orbit #01 much of the SO_2 is located along the side of the orbit, at relatively high satellite viewing angles. In order to untangle the effects of the viewing angle from the effects of aerosols on the OMPS SO_2 retrieval this analysis is extended to multiple orbits.

Extending the analysis to include all the orbits in Figure 4.23 provides a large set of OMPS SO_2 observations retrieved at a variety of satellite viewing angles. From this collection of orbits, 1:1 plots similar to those in Figure 4.24 - Figure 4.26 are shown, except now each point is color coded based on the pixel's satellite zenith angle. Figure 4.28 shows these 1:1 plots for $NR_{sulfate}$ with the sulfate observation simulator, $OS_{sulfate}$, and $NR_{ash+sulfate}$ with $OS_{ash+sulfate}$.

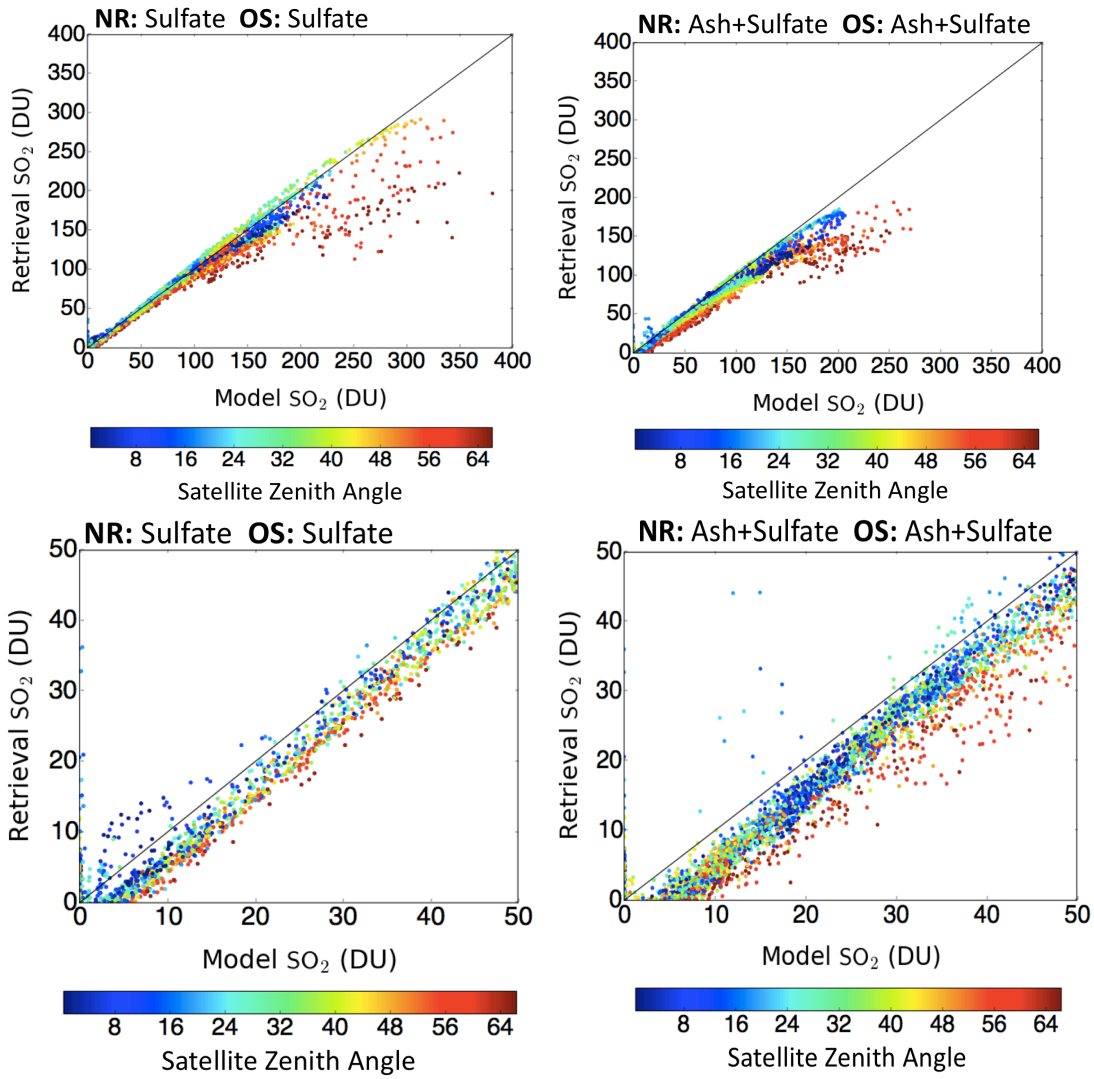

Figure 4.28 Effects of satellite zenith angle on the OMPS SO_2 retrieval. The top panels show all OMPS SO_2 pixels plotted against the nature run SO_2 pixels, for NRsulfate on the left and NRash+sulfate on the right. The bottom panels are the same as the top panels, but zoomed in on the lower SO_2 column pixels.

The color coding in Figure 4.28 shows that the OMPS SO_2 retrieval shows the greatest degree of underestimation at large satellite zenith. This result is consistent at both high and low SO_2 column concentrations. For both nature run input conditions, the SO_2 saturation at high column concentrations occurs at high zenith angles, with near nadir pixels falling much closer to the 1:1 line. This behavior also occurs at low

SO_2 column amount. Figure 4.28 displays a zoomed-in view of the SO_2 pixels at the lower column amounts, showing that the OMPS retrieval underestimation for low SO_2 column concentrations occurs as a direct offset which increases with increasing satellite zenith angle.

In the $OS_{sulfate}$ simulation, the OMPS retrieval tends to underestimate the SO_2 amount, but in some cases slightly overestimates the SO_2 amount. The inclusion of ash biases the OMPS SO_2 to further underestimate the SO_2 amount, with almost no cases of overestimation. This result is consistent with that seen in the analysis of orbit #01.

4.6 Conclusions

Volcanic clouds often contain mixtures of SO_2, ash and sulfate aerosols. In this study I constructed an OSSE to evaluate the influence of ash and sulfate aerosols on the OMPS SO_2 retrieval using two nature runs, one assuming an eruption of SO_2 and sulfate aerosols, $NR_{suflate}$, and another assuming SO_2, sulfate aerosols and volcanic ash, $NR_{ash+sulfate}$. An analysis of these nature runs showed that the ash induced significant lofting in the NRash+sulfate simulation. This lofting entrained ozone poor air from the troposphere upwards into the stratosphere, resulting in an apparent ozone hole within the volcanic plume. The lofting also induced an upper level anticyclone the altered the transport path of the volcanic cloud, leading to different transport patterns then what was observed in $NR_{sulfate}$. The ash in $NR_{ash+sulfate}$ caused the volcanic plume to loft by roughly 4 km over 5 days, compared to the 1 km – 1.5 km lofting in the $NR_{sulfate}$ simulation.

The observation simulator used the nature runs to compute TOA radiances. In general, it was shown that SO_2 and volcanic ash induce net reduction in the TOA radiances. Conversely, sulfate aerosols caused a relative increase to the TOA radiances. The magnitude of these effects varies depending on wavelength of the TOA radiance. When no aerosols are included in the synthetic radiance calculation, the OMPS SO_2 retrieval accurately reproduces the nature run SO_2. However, when the effects of sulfate aerosols are included in the synthetic radiances, the amount of SO_2 estimated from the OMPS SO_2 retrieval tends to increase at SO_2 column densities > 50 DU, except at high SO_2 column amounts which result in an SO_2 underestimation. At low SO_2 column densities, < 50 DU, the inclusion of sulfate aerosols produced negligible effects on the OMPS retrieval output. Volcanic ash caused a general underestimation of the SO_2 retrieval at all SO_2 column values. The ash and sulfate aerosols appear to have a neutralizing net effect, where their effects of over- and underestimation in the OMPS SO_2 retrieval can cancel each other out at low SO_2 column densities. The satellite viewing angle also plays a large role in amplifying the effects of sulfate aerosols and ash on the OMPS SO_2 retrieval. The largest underestimation of the OMPS SO_2 retrieval almost always occurred at high satellite zenith angles, regardless of the SO_2 column density.

These results highlight the importance of accounting for the effects of aerosols when using UV observations of SO_2 to estimate the total mass of SO_2 emitted from a volcanic eruption. The effects of ash and sulfate aerosols on low SO_2 column densities is mostly linear, while the effects at much higher SO_2 column densities becomes non-linear resulting in increased retrieval underestimation. This result is

important since large volcanic eruptions tend to become the most studied volcanic eruptive events. Understanding the limitations of UV satellite observations in these events will help inform researchers about the level of accuracy to expect when constructing volcanic SO_2 emission source terms for large volcanic eruptions.

References, Chapter 4

Ackerman, A. S., P. V. Hobbs, and O. B. Toon (1995), A model for particle microphysics, turbulent mixing, and radiative transfer in the stratocumulus-topped marine boundary layer and comparisons with measurements, *Journal of the atmospheric sciences*, *52*(8), 1204-1236.

Aquila, V., L. D. Oman, R. S. Stolarski, P. R. Colarco, and P. A. Newman (2012), Dispersion of the volcanic sulfate cloud from a Mount Pinatubo–like eruption, *Journal of Geophysical Research: Atmospheres*, *117*(D6).

Bhartia, P., N. Krotkov, V. Aquila, E. Hughes, C. Li, and B. Fisher (2016), Modern Day Re-analysis of Pinatubo SO2 Injection, Cloud dispersion and Stratospheric Aerosols, paper presented at AGU Fall Meeting Abstracts.

Carn, S., K. Yang, A. Prata, and N. Krotkov (2015), Extending the long-term record of volcanic SO2 emissions with the Ozone Mapping and Profiler Suite nadir mapper, *Geophysical Research Letters*, *42*(3), 925-932.

Carn, S. A., A. J. Krueger, N. A. Krotkov, K. Yang, and K. Evans (2009), Tracking volcanic sulfur dioxide clouds for aviation hazard mitigation, *Natural Hazards*, *51*(2), 325-343.

Colarco, P., M. Schoeberl, B. Doddridge, L. Marufu, O. Torres, and E. Welton (2004), Transport of smoke from Canadian forest fires to the surface near Washington, DC: Injection height, entrainment, and optical properties, *Journal of Geophysical Research: Atmospheres*, *109*(D6).

Colarco, P. R., S. Gassó, C. Ahn, V. Buchard, A. M. d. Silva, and O. Torres (2017), Simulation of the Ozone Monitoring Instrument aerosol index using the NASA Goddard Earth Observing System aerosol reanalysis products, *Atmospheric Measurement Techniques*, *10*(11), 4121-4134.

Colarco, P. R., E. P. Nowottnick, C. A. Randles, B. Yi, P. Yang, K. M. Kim, J. A. Smith, and C. G. Bardeen (2014), Impact of radiatively interactive dust aerosols in

the NASA GEOS-5 climate model: Sensitivity to dust particle shape and refractive index, *Journal of Geophysical Research: Atmospheres*, *119*(2), 753-786.

English, J., O. Toon, M. Mills, and F. Yu (2011), Microphysical simulations of new particle formation in the upper troposphere and lower stratosphere, *Atmos. Chem. Phys*, *11*(17), 9303-9322.

English, J. M., O. B. Toon, and M. J. Mills (2012), Microphysical simulations of sulfur burdens from stratospheric sulfur geoengineering, *Atmospheric Chemistry and Physics*, *12*(10), 4775-4793.

Errico, R. M., R. Yang, N. C. Privé, K. S. Tai, R. Todling, M. E. Sienkiewicz, and J. Guo (2013), Development and validation of observing-system simulation experiments at NASA's Global Modeling and Assimilation Office, *Quarterly Journal of the Royal Meteorological Society*, *139*(674), 1162-1178.

Fisher, B. L., N. Krotkov, S. Carn, S. Taylor, C. Li, P. Bhartia, L. Huang, and D. Haffner (2017), Retrieving Volcanic SO2 from the 4-UV channels on DSCOVR/EPIC, paper presented at AGU Fall Meeting Abstracts.

Flemming, J., and A. Inness (2013), Volcanic sulfur dioxide plume forecasts based on UV satellite retrievals for the 2011 Grímsvötn and the 2010 Eyjafjallajökull eruption, *Journal of Geophysical Research: Atmospheres*, *118*(17), 10,172-110,189.

Flynn, L., Long, C., Wu, X., Evans, R., Beck, C. T., Petropavlovskikh, I., McConville, G., Yu, W., Zhang, Z., Niu, J., Beach, E., Hao, Y., Pan, C., Sen, B., Novicki, M., Zhou, S. and Seftor, C.: Performance of the Ozone Mapping and Profiler Suite (OMPS) products, *J. Geophys. Res. Atmos*., 119(10), 6181–6195, doi:10.1002/2013JD020467, 2014.

Guo, S., G. J. Bluth, W. I. Rose, I. M. Watson, and A. Prata (2004a), Re-evaluation of SO2 release of the 15 June 1991 Pinatubo eruption using ultraviolet and infrared satellite sensors, *Geochemistry, Geophysics, Geosystems*, *5*(4).

Guo, S., W. I. Rose, G. J. Bluth, and I. M. Watson (2004b), Particles in the great Pinatubo volcanic cloud of June 1991: The role of ice, *Geochemistry, Geophysics, Geosystems*, *5*(5).

Hughes, E., L. Sparling, S. Carn, and A. Krueger (2012), Using horizontal transport characteristics to infer an emission height time series of volcanic SO2, *Journal of Geophysical Research: Atmospheres*, *117*(D18).

Hughes, E., J. Yorks, N. Krotkov, A. Silva, and M. McGill (2016), Using CATS near-real-time lidar observations to monitor and constrain volcanic sulfur dioxide (SO2) forecasts, *Geophysical Research Letters*, *43*(20).

Jensen, E. J., O. B. Toon, D. L. Westphal, S. Kinne, and A. J. Heymsfield (1994), Microphysical modeling of cirrus: 1. Comparison with 1986 FIRE IFO measurements, *Journal of Geophysical Research: Atmospheres*, *99*(D5), 10421-10442.

Krotkov, N., M. Schoeberl, G. Morris, S. Carn, and K. Yang (2010), Dispersion and lifetime of the SO2 cloud from the August 2008 Kasatochi eruption, *Journal of Geophysical Research: Atmospheres*, *115*(D2).

Matichuk, R. I., P. R. Colarco, J. A. Smith, and O. B. Toon. "Modeling the transport and optical properties of smoke plumes from South American biomass burning." *Journal of Geophysical Research: Atmospheres* 113, no. D7 (2008).

Matichuk, R. I., P. R. Colarco, J. A. Smith, and O. B. Toon. "Modeling the transport and optical properties of smoke aerosols from African savanna fires during the Southern African Regional Science Initiative campaign (SAFARI 2000)." *Journal of Geophysical Research: Atmospheres* 112, no. D8 (2007).

Niemeier, U., C. Timmreck, H.-F. Graf, S. Kinne, S. Rast, and S. Self (2009), Initial fate of fine ash and sulfur from large volcanic eruptions, *Atmospheric Chemistry and Physics*, *9*(22), 9043-9057.

Pawson, S., R. S. Stolarski, A. R. Douglass, P. A. Newman, J. E. Nielsen, S. M. Frith, and M. L. Gupta (2008), Goddard Earth Observing System chemistry-climate model simulations of stratospheric ozone-temperature coupling between 1950 and 2005, *Journal of Geophysical Research: Atmospheres*, *113*(D12).

Sekiya, T., K. Sudo, and T. Nagai (2016), Evolution of stratospheric sulfate aerosol from the 1991 Pinatubo eruption: Roles of aerosol microphysical processes, *Journal of Geophysical Research: Atmospheres*, *121*(6), 2911-2938.

Spurr, R. J. (2006), VLIDORT: A linearized pseudo-spherical vector discrete ordinate radiative transfer code for forward model and retrieval studies in multilayer multiple scattering media, *Journal of Quantitative Spectroscopy and Radiative Transfer*, *102*(2), 316-342.

Toon, O., R. Turco, D. Westphal, R. Malone, and M. Liu (1988), A multidimensional model for aerosols: Description of computational analogs, *Journal of the Atmospheric Sciences*, *45*(15), 2123-2144.

Wang, J., S. Park, J. Zeng, C. Ge, K. Yang, S. Carn, N. Krotkov, and A. Omar (2013), Modeling of 2008 Kasatochi volcanic sulfate direct radiative forcing: assimilation of OMI SO2 plume height data and comparison with MODIS and CALIOP observations.

Wiscombe, W. J. (1980), Improved Mie scattering algorithms, *Applied optics*, *19*(9), 1505-1509.

Wolfe, E. W., and R. P. Hoblitt (1996), Overview of the Eruptions, in Fire and Mud: Eruptions and Lahars of Mount Pinatubo, Philippines, edited by C. G. Newhall and R. S. Punongbayan, pp. 415–433, Univ. of Wash. Press, Seattle.

Chapter 5: CATS Near-Realtime Lidar Observations to Monitor and Constrain Volcanic Sulfur Dioxide (SO_2) Forecasts

5.1 Introduction

Forecasting the transport of volcanic plumes for aviation hazards mitigation requires timely analysis of all available observations to initialize and refine ash dispersion forecasts and issue Volcanic Ash Advisories in the wake of a volcanic eruption. UV spectrometers aboard polar orbiting satellites, like OMI [*Levelt et al.*, *2006*] and OMPS [*Flynn et al.*, *2014*], provide volcanic SO_2 vertical column density maps, used to track the horizontal transport of volcanic SO_2 clouds [*Ialongo et al., 2015; Carn et al., 2015, Li et al., 2017*]. Observations from both satellite and ground-based Lidar instruments have been used to monitor and track the altitude of volcanic sulfate aerosols, often co-located with volcanic SO_2, and ash clouds [*Winker and Osborn, 1992; Sassen et al., 2007; Wiegner et al., 2012; Vernier et al., 2013*]. Satellite based lidars, like CALIOP [*Winker et al.*, *2009*], have frequently been used to study volcanic eruptions [*Winker et al.*, *2012; Vernier et al., 2013*], but largely as a verification tool [*Eckhert et al., 2008; Hughes et al., 2012*]. CALIOP has a small sampling footprint, and similarly, a long repeat cycle, that limits the likelihood that the lidar will intercept a volcanic cloud (see Section 4). Furthermore, the data processing latency time for CALIOP is between 24 and 48 hours. In tandem, these two factors make it unlikely that observations will be available within the first days of a volcanic eruption, limiting their application for near-real time volcanic cloud monitoring and forecasting.

The CATS lidar onboard the International Space Station (ISS) was in operation from January 2015 to October 2017, and had an added benefit of near-real time product generation, i.e., within 3 – 6 hour latency. CATS utilized the ISS data downlinking capabilities, which transmit raw data to the CATS ground station from the ISS within seconds of collection using the Tracking and Data Relay Satellite (TDRS) network. Given interruption due to loss-of-signal (LOS) periods and processing of the CATS data, the latency time is about 3-6 hours [*Yorks et al.*, *2016*]. In contrast, CALIOP data is downlinked only once per day using X-band telemetry from Hawaii and Alaska ground stations. Near-real time processing permitted the use of CATS data to be incorporated into the data assimilation and/or model initialization processes of aerosol forecast models and potentially improve model forecasts of volcanic cloud transport at an expedited timing that's crucial for aviation hazards mitigation.

On December 3rd 2015, passive instruments on the geostationary satellite Meteosat Second Generation (MSG) and various polar orbiting satellites observed large volcanic SO_2 and ash plumes that resulted from the eruption of Mt. Etna volcano in Sicily, Italy. Observations mapped the volcanic ash and SO_2 transport towards the east. The CATS lidar instrument observed the backscattering from the aerosols in the volcanic cloud, providing a near-real time direct observation of the volcanic cloud's altitude. This was the first time observations from CATS have been used to observe volcanic clouds and model volcanic plumes.

The ash in the volcanic cloud falls out to the ground in less than 24 hours, so this study focuses on the observation and modeling of long-lasting volcanic SO_2 and

secondary sulfate aerosols. While ash is the primary hazard to aviation, SO_2 is often used as a proxy for co-located fine ash in order to track dispersed volcanic clouds for a longer time [*Carn et al.*, *2009*; *Thomas and Prata*, *2011*]. Satellite SO_2 observations in conjunction with backward trajectory analyses were used to estimate volcanic source terms: eruption duration, SO_2 emission flux and injection vertical profile [*Hughes et al.*, *2012*]. These source terms were used to model the transport of the volcanic emissions with the global Eulerian NASA Goddard Earth Observing System Version 5 (GEOS-5) Earth system model, accounting for the sulfur chemistry and aerosol physical – chemical processes with the coupled online Goddard Chemistry Aerosol and Radiation (GOCART) model [*Chin et al., 2000; Colarco et al., 2010* and references within]. Initial forecasts of the SO_2 and sulfate aerosols dispersion from this eruption used an injection height estimate derived from a back-trajectory analysis based on OMPS daily two-dimensional (2D) total column SO_2 observations. The results from these simulations differed substantially from the observed transport of the volcanic SO_2 cloud on subsequent days. CATS observations clearly showed that the actual altitude of the volcanic cloud was higher than what was initially estimated. Here we demonstrate how volcanic aerosol heights measured by CATS are used to correct the injection altitude for a volcanic SO_2 cloud, resulting in a drastic improvement in the cloud long-term dispersion forecast.

To keep this analysis in the scope of aviation hazards mitigation, only observations from the first 48 hours after the eruption, no later than December 4th 2015, are used to refine the model simulation. Later observations are used to evaluate

the accuracy of the model simulations. The results of this study were previously published in Hughes et al. [*2016*].

5.2 The Eruption of Mt. Etna

On December 3rd 2015, Mt. Etna began an explosive eruption at ~2:00 UTC, which lasted for approximately 3 hours, injecting large volcanic ash, sulfate, and SO_2 plumes in the upper troposphere. The eruption timing was estimated using geostationary Meteosat-10/SEVIRI RGB Dust and Airmass observations [*Lensky and Rosenfeld*, *2008*; *Smiljanic et al.*, *2015*]. An analysis of this SEVIRI imagery suggests that some ice may have been formed in the early stages of the volcanic cloud, but by 9:00 UTC the cloud was mostly SO_2 composed [*Smiljanic et al. 2015*]. After the eruption, upper tropospheric winds advected the volcanic SO_2 and secondary sulfate plume to the east, creating a large, fast moving volcanic cloud. Visible imagery on Dec 3rd shows the volcanic cloud with both a darkish brown color (ash) and a white cloud (ash, sulfate, or ice), as seen from satellite instruments: Terra/MODIS (09:05 UTC), S-NPP/VIIRS (11:05 UTC), and Aqua/MODIS (12:35 UTC). These successive observations appear to show the darker cloud (ash) splitting off of the whiter cloud. This imagery can be viewed using the NASA worldview website: https://worldview.earthdata.nasa.gov. On December 4th, polar orbiting satellite instruments typically used to observe volcanic ash and SO_2 were only detecting SO_2 in the volcanic cloud. Neither IR or UV instruments saw any clear ash signature. The ash and SO_2 products from these instruments can be viewed at the

Support to Aviation Control Service website (SACS, http://sacs.aeronomie.be) [*Brenot et al. 2014*].

The lack of observable ash in observations after December 3rd suggests that the volcanic ash fell out of this cloud within 1 day, and thus ash was not included in the model simulations.

5.3 Observed SO_2 Transport

The first OMPS observation of the Etna SO_2 cloud occurred approximately at 11:05 UTC on December 3rd, roughly 9 hours after the start of the eruption, estimating total SO_2 mass ~30 kt. On a global scale, eruptions producing SO_2 clouds of this magnitude are not uncommon. SO_2 clouds of this magnitude tend to be observable by satellites for several days, before dispersive and chemical conversion processes reduce the SO_2 column amount to below the satellite detection limit (~0.1 - 0.3 DU [Li *et al., 2016*]).

As the SO_2 cloud travelled eastward, it began shearing horizontally; parts of the cloud move to the east much more quickly than others. By December 4th, the SO_2 cloud spanned in longitude from 25E to 50E (Figure 5.1A). Continued transport on successive days further stretched the volcanic plume into a filament like structure and advected the entire cloud further to the east (Figure 5.3A).

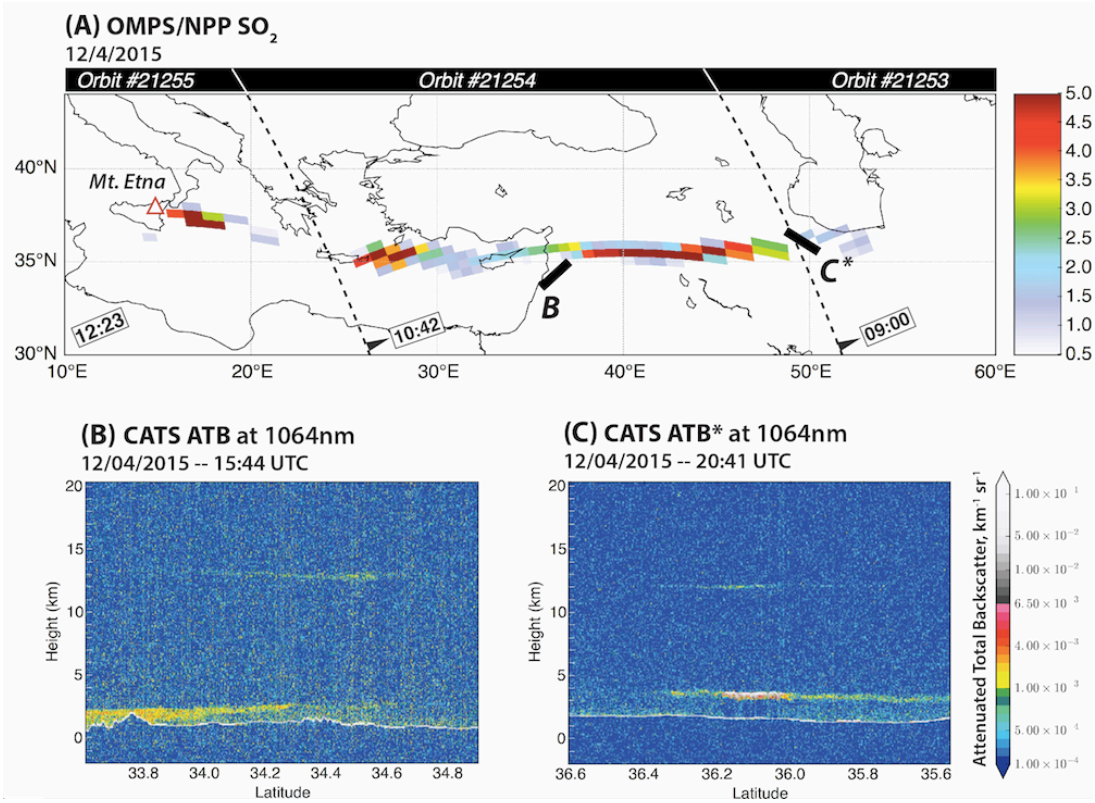

Figure 5.1 Observations of the Etna SO_2 plume. A map of the total column SO_2 from OMPS on December 4th is shown in (A). CATS Attenuated Total Backscatter (ATB) profiles at 1064nm are shown in (B) and (C). The track of the profiles (B) and (C) are plotted on (A), as labeled. An asterisk (*) is used to denote CATS nighttime observations.

5.4 CATS Observed Volcanic Plume Vertical Distributions

The CATS lidar has been operating on the International Space Station (ISS) since early 2015, providing vertical profiles of clouds and aerosols at 532 and 1064 nm wavelengths [*McGill et al.*, *2015*]. CATS is an ideal tool for measuring the vertical extent of volcanic plumes for several reasons. CATS can detect top and base altitudes of atmospheric aerosol layers as high as 28.0 km, which is the upper limit of the instrument's data acquisition region. Spherical particles, such as sulfate, can be differentiated from non-spherical particles (i.e. dust, ash, and ice crystals) using

CATS depolarization measurements. Finally, CATS sensitivity to optically thin aerosol layers (1064 nm attenuated total backscatter as low as $5.0*10^{-5}$ $km^{-1}sr^{-1}$) enables detection of weakly scattering volcanic plumes in the upper troposphere and lower stratosphere [*Yorks et al.*, *2016*]. The ISS orbital path restricts CATS to observing volcanic eruptions that occur in the mid-latitudes and tropics, but provides more frequent sampling in these regions. For example, CATS will, on average, re-sample the same geographic point every 3-days, compared to an average 16-day repeat cycle for the polar orbiting CALIPSO/CALIOP [Winker *et al.*, *2009*]. More frequent regional sampling increases the likelihood that the CATS lidar will intercept dispersing volcanic clouds in the mid-latitudes and tropics. Considering the 3-day repeat cycle for CATS and the dispersion of advected volcanic clouds, it is reasonable to expect CATS to intercept volcanic clouds within 1-2 days of the initial eruption.

In this analysis, CATS attenuated total backscatter observations of the volcanic aerosol layers are compared to coincident OMPS total vertical column SO_2 observations. The attenuated total backscatter (ATB or β'), with units of km^{-1} sr^{-1}, is the primary parameter of the CATS L1B data product. The attenuated total backscatter is the sum of the parallel and perpendicular polarization components. It should be noted that OMPS UV makes daytime only observations, while CATS makes both day and night observations; so not all CATS observations of the volcanic plume are coincident with OMPS observations.

In Figure 5.1 (B and C), the CATS 1064 nm Attenuated Total Backscatter (ATB) profiles show faint, but distinct, scattering layers in the height range of 11.5 - 13.5 km. The vertical thickness of the layers remains rather thin, less than 1 km, for

all observations. The coincidence of the CATS observations with the OMPS SO_2 observations (Figure 5.1A) and low 1064 nm depolarization ratios (< 0.10) suggest that the scattering layers observed by CATS are due to scattering by spherical secondary volcanic sulfate aerosols (with some non-spherical ash particles possibly present), and not ice crystals.

5.5 Trajectory Estimated Volcanic Plume Vertical Distribution

Prior to satellite lidar observations of volcanic plume heights, the plume altitudes were estimated from the analysis of the observed transport [*Allen et al., 1999; Eckhert et al., 2008; Krotkov et al., 2010; Hughes et al., 2012*]. In this study, the initial injection altitude of the volcanic plume was estimated from the *Hughes et al.* [*2012*] approach, using vertical stacks of trajectories initialized at the OMPS 2D SO_2 observations of the SO_2 columns of at least .5 DU on December 4th 2015 (orbits 21253 and 21254), as shown in Figure 5.1A. The trajectories are driven backwards in time, to the Etna volcano location, using the NASA GSFC Trajectory Model [*Schoeberl and Sparling*, *1995*] and driven by the NCEP GFS Operational 1^ox1^o meteorology [*NCEP, 2003*]. Selecting those trajectories that arrive sufficiently close to the volcano, within 100 km, on the morning of the eruption yields an ensemble of all possible air parcel trajectories. A Probability Distribution Function (PDF) derived from this ensemble of possible trajectories provides an estimate of the eruptions injection altitude time-series [*Hughes et al.*, *2012*]. The duration of the Etna eruption was relatively short (less than 3 hours), so the PDF's time-dimension was integrated

to yield a single height distribution, used as an eruption source term for the global Eulerian GEOS-5 model.

The PDF of the volcanic trajectory ensemble, with respect to the altitude at the volcano, is shown in figure 5.2A. The PDF of arrival heights suggests that the most likely initial altitude range of the emissions is between 7-12 km, with a minimum likelihood across this range at 8-9km. The CATS observations from December 4th, shown in Figures 1B and 1C, are expressed as height distributions in Figure 5.2B. The CATS height distributions represent the fraction of observations, per layer, where ATB is greater than a minimum threshold value to indicate aerosol scattering, in this case .0006 $km^{-1}sr^{-1}$. The background noise across orbits varies, so the CATS height distributions are normalized by the total number of observations in an orbital segment that meet this condition. The CATS heights distributions are only performed on the narrow sections of the orbit were the volcanic cloud was observed, as shown in Figures 1 B and C. Figure 5.2B shows that the volcanic cloud was observed between 11.5 – 12.5 km (blue) and 12.5 – 13.5 km (green).

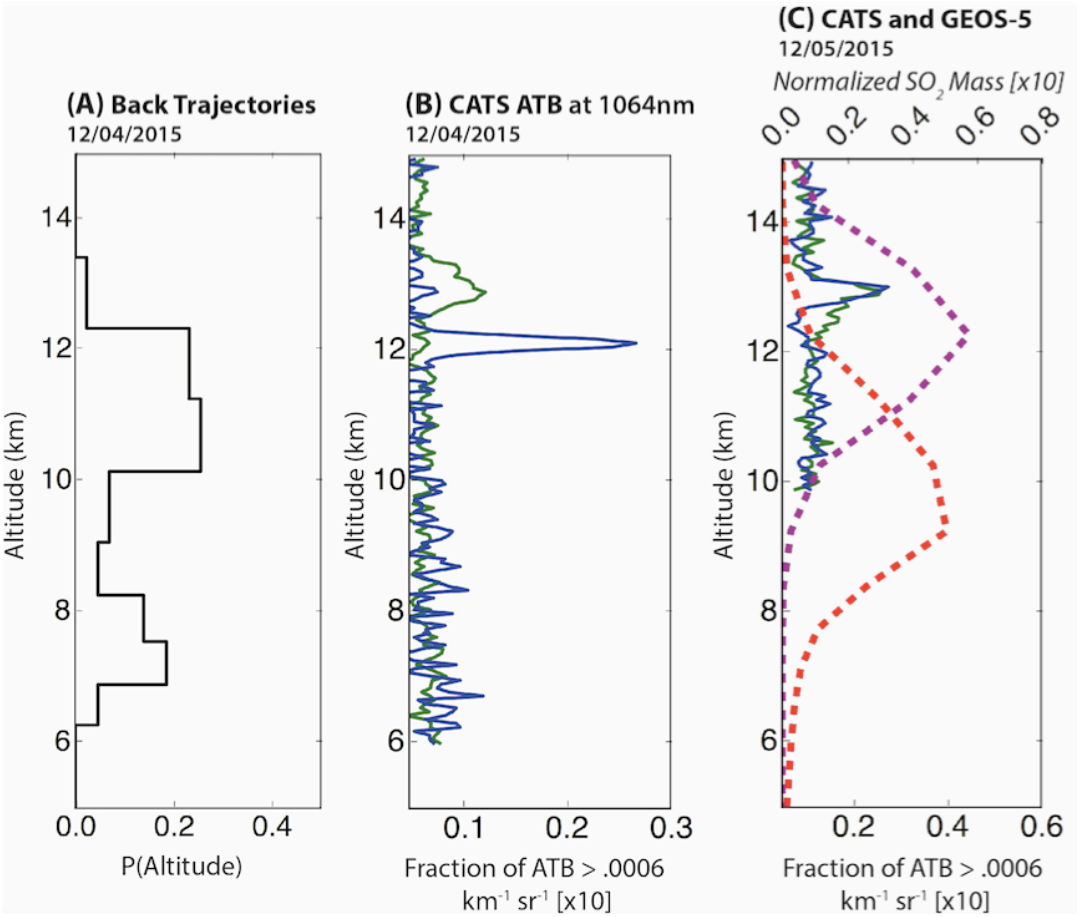

Figure 5.2 Altitude Observations and Estimates of the Etna SO_2 and sulfate aerosol cloud. An emission altitude Probability Distribution Function (PDF) based on back trajectories is shown in (A). In (B), the layer fraction of ATB observations above .0006 $km^{-1}sr^{-1}$ is shown for CATS observations. The CATS observations in (B) are from 12/04/2015 – 15:44 UTC (green), as shown in Figure 5.1B, and from 12/04/2015 – 22:16 UTC (blue), as shown in Figure 5.1C. A similar plot of CATS observations is shown in (C), for the observations on 12/5/2015 – 18:16 UTC (blue) and 12/5/2015 – 19:50 UTC (green). Also plotted in (C) in the vertical distribution of the GEOS-5 SO_2 mass at 12/5/2015 at 6:00 UTC, which represents the spatially integrated mass across the cloud advection region: latitude [30N,50N] and longitude [10E,100E]. This region is shown in Figure 5.3 (B) and (C). The trajectory simulation is shown in dashed red and the CATS simulation is shown in dashed purple.

5.6 Modeling the Transport of Volcanic SO_2 Cloud in GEOS-5/GOCART

The transport of the volcanic plume was modeled using GEOS-5 [*Suarez et al., 2008*]. In these simulations, the GEOS-5 model with GOCART aerosol processes is used on-line to model volcanic SO_2 and sulfate aerosol chemistry [*Colarco et al.*, *2010*]. Similar to the setup used in Chapter 3, GEOS-5 is run on a cube-shpere grid at c180 horizontal resolution (~ 0.5^ox0.5^o) and with 72 vertical levels, with model data sampled at 3-hour intervals (00z, 03z, 06z … 21z).

The timing of the eruption was estimated from geostationary satellite observations as a 3 hour-long injection started at 02:00UTC on December 3rd. The flux rate 8.33×10^3 kg SO_2/s was assumed constant over the eruption period, and computed from the total emitted SO_2 mass ~30 kt, as observed by OMPS. The altitude of the emissions was varied, depending on the source of the height information. One simulation used the injection height range given by the trajectory estimate, and another simulation used an injection height range based on the height ranges observed by CATS on December 4th. The height range is used to assign the top and bottom of the SO_2 injection into the GEOS-5 model vertical layers; the flux was evenly vertically distributed between these layers.

In general, the downstream CATS observed heights would not necessarily be the same as the source injection heights. To check the relationship between the downstream observed heights and the initial injection heights, simulations at varying injection altitudes were computed, from 8km to 18km. We found that in this case only

the 11.5 – 13.5 km initialization reconstructed the downstream 11.5 – 13.5 km CATS observations, *i.e.*, that the source height and the downstream height were the same.

5.7 Discussion

Two model simulations were generated for this analysis: one assuming an initial plume height of 7-12 km based on the trajectory height estimate (trajectory simulation) and another assuming 11.5-13.5 km based on CATS height observations (CATS simulation). The goal of this comparison is to demonstrate that the altitude information provided by CATS results in a significant improvement in the model simulation of the observed long-range volcanic cloud transport.

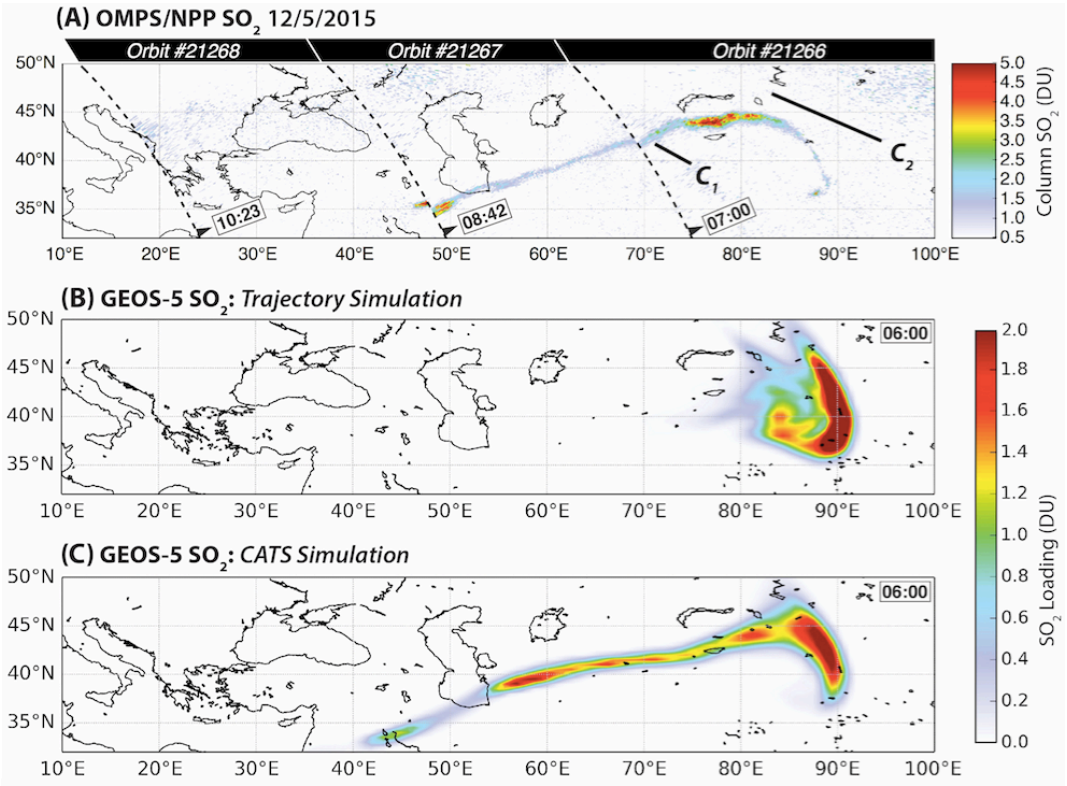

Figure 5.3 Comparison of GEOS-5 SO_2 to OMPS observations. A map of the OMPS total column SO_2 is shown in (A), from observations on 12/5/2015 (07:00 – 10:23 UTC). Also shown in (A) are the locations of the December 5th CATS observations used in Figure 5.2C, green (C_1) and blue (C_2). The GEOS-5/GOCART SO_2 model results for 12/5/2015 – 06:00 UTC are shown in (B) and (C), for the trajectory and CATS simulations, respectively.

Figure 5.3 compares the horizontal extent of the SO_2 cloud in the GEOS-5 simulations with the OMPS column SO_2 observations. This figure clearly shows that the CATS simulation (Fig. 5.3C) produced a more realistic forecast compared to the trajectory simulation (Fig. 5.3B), which pushed the SO_2 cloud further to the east and too quickly. In the CATS simulation the SO_2 cloud only partially moves toward the east, better simulating the filament-like structure observed in the OMPS SO_2 observations, Figure 5.3A.

The vertical structure of the GEOS-5 SO_2 simulations is compared to the CATS observations in figure 5.2C, which shows the SO_2 mass vertical distribution integrated over the geographic region shown in figures 3B and 3C. Figure 5.2C shows that the height distribution in the CATS simulation agrees with CATS height observations, while the trajectory simulation pushes the total mass much lower then what CATS observed on December 5th. Figure 5.4 shows a more detailed view of the vertical structure of the CATS and trajectory GEOS-5 simulations. In both simulations, the eastern edge of the cloud is located at between 10-13km. However, in the CATS simulation the cloud trails to the west at 12-14 km, while in the trajectory simulation the cloud trails to the west at lower altitudes of 10-8 km.

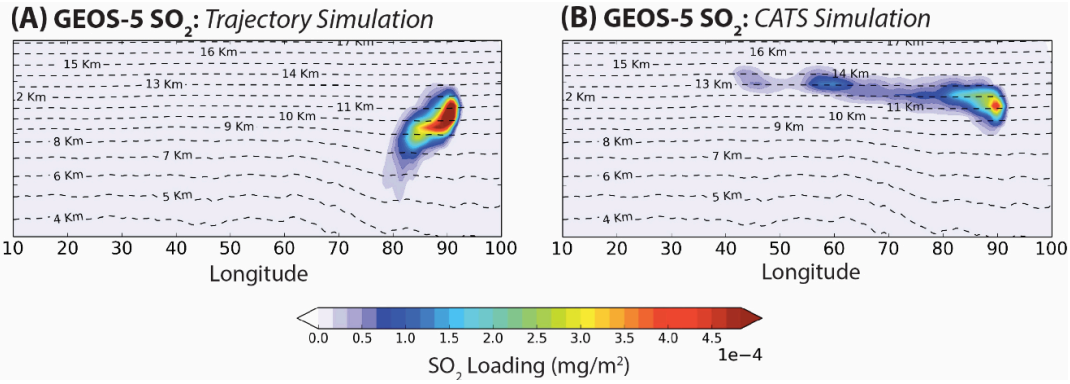

Figure 5.4 Comparison of GEOS-5/GOCART model SO_2 vertical distribution. The vertical profiles represent a meridional sum across the latitude bounds [30N, 50N] on December 5th at 06:00 UTC. The model results in Figure 5.3 (B) and (C) are shown here in (A) and (B), respectively.

Overall, Figures 5.3 and 5.4 show large differences in the horizontal and vertical structure between the CATS and trajectory GEOS-5 SO_2 simulations. Using CATS height information to redefine our source terms in the model has clearly improved the simulation to yield a better match with both OMPS and CATS

observations. This result also highlights the importance of correctly assessing the injection altitude of volcanic plumes in order to construct accurate forecasts of their horizontal transport. To further understand why these simulations produced such different results, the meteorological conditions should be considered. The shearing of the volcanic cloud, shown in figure 5.3A, is the result of an eruption that placed the volcanic plume partially in the subtropical jet. The trajectory simulation places the volcanic plume partially into the core of the subtropical jet and partially below, Figure 5.4A. The CATS observed heights show the plume to be partially within the subtropical jet and partially above, as seen in the CATS simulation in Figure 5.4B. The inability of the trajectory method to accurately estimate the volcanic plume altitude highlights the limitations of transport methods to accurately deduce volcanic plume heights. Transport analyses deduce altitude by contrasting potential transport paths, but without distinct contrasts between transport paths, transport analyses will have difficultly resolving the correct transport path altitude. In the case of the Mt. Etna eruption, the trajectories deduced a shearing mechanism, but not the correct one, and ultimately the wrong injection altitude.

5.8 Conclusions and Outlook

In the context of aviation hazards mitigation, forecasting the transport of volcanic plumes via the subtropical jet is crucial. The increased wind speeds in jet stream are routinely used to speed up aviation travel at a reduced fuel cost [*Houghton*, *1998*]. The eruption of volcanic clouds into jet streams creates a direct aviation hazard in these frequently used atmospheric corridors. Furthermore, jet streams

rapidly advect volcanic clouds across long distances, producing aviation hazards in regions that may be very far from the volcanic eruption. As this paper has demonstrated, modeling the transport of volcanic plumes that have been partially injected into the subtropical jet can be difficult. Transport analysis can yield unreliable results.

It has been demonstrated that direct height observations from space-based LIDAR instruments, like CATS, can greatly improve the accuracy of model simulations. This study focused on a volcanic SO_2 cloud that was mostly devoid of volcanic ash. While volcanic ash is the primary concern for aviation, tracking SO_2 clouds has been shown beneficial for tracking volcanic ash [*Thomas and Prata, 2011*]. This type of analysis could similarly be applied to volcanic ash clouds, as CATS observations would also provide accurate ash cloud height. Modeling volcanic ash clouds is typically more complicated then volcanic SO_2 clouds, since the ash particle density and size distributions must be estimated or assumed. However, research by Miffre et al. [*2012*] has demonstrated that ground-based UV lidar depolarization observations can provide altitude-resolved ash particle number concentrations, which provides a similar means of using lidar observations to constrain volcanic clouds simulations.

In this case study, CATS day and night observations were able to detect scattering in the aerosol plume down to .0006 $km^{-1}.sr^{-1}$, approximately 0.02 AOD. Multiple CATS observations demonstrated that the altitude range of the volcanic aerosol cloud was higher than estimated by trajectories. The CATS observed height range was used as the eruptions injection height range and the model simulations

improved accordingly. As noted previously, assuming that the downwind observed volcanic cloud height is the same as the initial injection height is not necessarily valid. It is important to check the relationship between downstream altitude and the injection altitude, which can be done nudging the injection altitude in the model. Another important aspect to keep in mind is that lidar observations, like CATS, only show a narrow picture of part of a volcanic cloud. Lidar profiles can observe different height distributions for the same volcanic cloud, as shown in Figure 5.2b, since different parts of a volcanic cloud can be at different altitudes. Hence, it is important to have multiple height observations of a volcanic cloud in order to confidently assess its height range. Taking advantage of both ground and satellite based lidar observations could potentially provide ample coverage of a volcanic clouds height distribution, but these observations are required in near real time to adjust the model in a timely manner. The CATS near real-time processing and data products provide timely injection height information to improve current volcanic cloud forecasting capabilities.

References, Chapter 5

Allen, D. R., Schoeberl, M. R., & Herman, J. R. (1999). Trajectory modeling of aerosol clouds observed by TOMS. Journal of Geophysical Research: Atmospheres, 104(D22), 27461-27471.

Carn, S. A., Krueger, A. J., Krotkov, N. A., Yang, K., & Evans, K. (2009). Tracking volcanic sulfur dioxide clouds for aviation hazard mitigation. Natural Hazards, 51(2), 325-343

Carn, S. A., K. Yang, A. J. Prata, and N. A. Krotkov (2015), Extending the long-term record of volcanic SO2 emissions with the Ozone Mapping and Profiler Suite nadir mapper, Geophys. Res. Lett., 42, doi:10.1002/2014GL062437.

Chin, Mian, Richard B. Rood, Shian-Jiann Lin, Jean-Francois Müller, and Anne M. Thompson. "Atmospheric sulfur cycle simulated in the global model GOCART: Model description and global properties." (2000). doi: 10.1029/2000JD900384

Dunn, M.G., Wade, D.P., 1994. Influence of volcanic ash clouds on gas turbine engines. U.S. Geological Survey Bulletin 2047, 107 – 118.

Eckhardt, S., Prata, A. J., Seibert, P., Stebel, K., & Stohl, A. (2008). Estimation of the vertical profile of sulfur dioxide injection into the atmosphere by a volcanic eruption using satellite column measurements and inverse transport modeling. Atmospheric Chemistry and Physics, 8(14), 3881-3897.

Flynn, L., Long, C., Wu, X., Evans, R., Beck, C. T., Petropavlovskikh, I., McConville, G., Yu, W., Zhang, Z., Niu, J., Beach, E., Hao, Y., Pan, C., Sen, B., Novicki, M., Zhou, S. and Seftor, C.: Performance of the Ozone Mapping and Profiler Suite (OMPS) products, J. Geophys. Res. Atmos., 119(10), 6181–6195, doi:10.1002/2013JD020467, 2014.

Guffanti, M., T. J. Casadevall and K. Budding (2010), Encounters of aircraft with volcanic ash clouds: a compilation of known incidents, 1953-2009. U.S. Geological Survey Data Series 545, ver. 1.0, 12 p., plus 4 appendixes including the compilation database.

Hughes, E. J., Sparling, L. C., Carn, S. A., & Krueger, A. J. (2012). Using horizontal transport characteristics to infer an emission height time series of volcanic SO2. Journal of Geophysical Research: Atmospheres, 117, *D18307, doi:10.1029/2012JD017957*.

Ialongo, I., Hakkarainen, J., Kivi, R., Anttila, P., Krotkov, N. A., Yang, K., ... & Tamminen, J. (2015). Validation of satellite SO2 observations in northern Finland during the Icelandic Holuhraun fissure eruption. Atmos. Meas. Tech. Discuss, 8(1), 599-621.

International Air Transport Association (IATA, 2010),IATA Economics Briefing: The Impact of Eyjafjallajokull's Volcanic Ash Plume, http://www.iata.org/whatwedo/Documents/economics/Volcanic- Ash-Plume-May2010.pdf.

Krotkov, N. A., Schoeberl, M. R., Morris, G. A., Carn, S., & Yang, K. (2010). Dispersion and lifetime of the SO2 cloud from the August 2008 Kasatochi eruption. Journal of Geophysical Research: Atmospheres, 115(D2).

Lensky, I. M., and Daniel Rosenfeld. "Clouds-aerosols-precipitation satellite analysis tool (CAPSAT)." Atmospheric Chemistry and Physics 8, no. 22 (2008): 6739-6753.

Levelt, P. F., Oord, G. H. J. Van Den, Dobber, M. R., Mälkki, A., Visser, H., Vries, J. De, Stammes, P., Lundell, J. O. V and Saari, H.: The Ozone Monitoring Instrument, IEEE Trans. Geosci. Remote Sens., 44(5), 1093–1101, 2006.

Li, Can, Nickolay A. Krotkov, Simon Carn, Yan Zhang, Robert JD Spurr, and Joanna Joiner. "New-generation NASA Aura Ozone Monitoring Instrument (OMI) volcanic SO2 dataset: Algorithm description, initial results, and continuation with the Suomi-NPP Ozone Mapping and Profiler Suite (OMPS)." Atmospheric Measurement Techniques 10, no. 2 (2017): 445.

Mazzocchi, M., F. Hansstein, and M. Ragona. 2010. The 2010 Volcanic Ash Cloud and Its Financial Impact on the European Airline Industry. CESifo Forum No. 2: 92–100.

McGill, M.J., J. E. Yorks, V. S. Scott, A. W. Kupchock, P. A. Selmer (2015), The Cloud-Aerosol Transport System (CATS): a technology demonstration on the International Space Station, Proc. SPIE 9612, Lidar Remote Sensing for Environmental Monitoring XV, 96120A, doi:10.1117/12.2190841.

Miffre, A., G. David, B. Thomas, M. Abou Chacra, and P. Rairoux. "Interpretation of accurate UV polarization lidar measurements: Application to volcanic ash number concentration retrieval." Journal of Atmospheric and Oceanic Technology 29, no. 4 (2012): 558-568.

NCEP: The GFS Atmospheric Model. NCEP Office Note 442, Global Climate and Weather Modeling Branch, EMC, Cam Springs Maryland, 2003

Ronald C. C. Houghton (1998). Aircraft Fuel Savings in Jet Streams by Maximizing Features of Flight Mechanics and Navigation. Journal of Navigation, 51, pp 360-367.

Sassen, Kenneth, Jiang Zhu, Peter Webley, Ken Dean, and Patrick Cobb. "Volcanic ash plume identification using polarization lidar: Augustine eruption, Alaska." Geophysical Research Letters 34, no. 8 (2007).

Schoeberl, M. R., and L. C. Sparling (1995), Trajectory modelling. Diagnostic tools in atmospheric physics, in Proceedings of the International School of Physics: Course CXVI, edited by G. Fiocco and G. Visconti, pp. 289–306, IOS Press, Amsterdam.

Schoeberl, M. R., Douglass, A. R., Hilsenrath, E., Bhartia, P. K., Beer, R., Waters, J. W., Gunson, M. R., Froidevaux, L., Gille, J. C., Barnett, J. J., Levelt, P. F. and DeCola, P.: Overview of the EOS aura mission, IEEE Trans. Geosci. Remote Sens., 44(5), 1066–1072, doi:10.1109/TGRS.2005.861950, 2006.

Smiljanic, Ivan. Setvak M., Prata F. and Kerkmann J. "On 3 December, for the first time in two years Mount Etna, erupted."EUMETSAT Image Library (blog), EUMETSAT, December, 2015. Retrieved on October 5, 2016. http://www.eumetsat.int/website/home/Images/ImageLibrary/DAT_2868529.html

Suarez, Max J., M. M. Rienecker, R. Todling, J. Bacmeister, L. Takacs, H. C. Liu, W. Gu et al. "The GEOS-5 Data Assimilation System-Documentation of Versions 5.0. 1, 5.1. 0, and 5.2. 0." (2008).

Thomas, H. E., & Prata, A. J. (2011). Sulphur dioxide as a volcanic ash proxy during the April–May 2010 eruption of Eyjafjallajökull Volcano, Iceland. Atmospheric Chemistry and Physics, 11(14), 6871-6880.

Vernier, J-P., T. D. Fairlie, J. J. Murray, A. Tupper, C. Trepte, D. Winker, Jacques Pelon et al. "An advanced system to monitor the 3D structure of diffuse volcanic ash clouds." Journal of Applied Meteorology and Climatology 52, no. 9 (2013): 2125-2138.

Wiegner, M., Gasteiger, J., Groß, S., Schnell, F., Freudenthaler, V., & Forkel, R. (2012). Characterization of the Eyjafjallajökull ash-plume: Potential of lidar remote sensing. Physics and Chemistry of the Earth, Parts A/B/C, 45, 79-86

Winker, D. M., M. A. Vaughan, A. H. Omar, Y. Hu, K. A. Powell, Z. Liu, W. H. Hunt, and S. A. Young (2009), Overview of the CALIPSO mission and CALIOP data processing algorithms, J. Atmos. Oceanic Technol., 26, 2310–2323, doi:10.1175/2009JTECHA1281.1.

Winker, D. M., Z. Liu, A. Omar, J. Tackett, and D. Fairlie (2012), CALIOP observations of the transport of ash from the Eyjafjallajökull volcano in April 2010, J. Geophys. Res., 117, D00U15, doi:10.1029/2011JD016499.

Yorks, J. E., M. J. McGill, S. P. Palm, D. L. Hlavka, P. A. Selmer, E. P. Nowottnick, M. A. Vaughan, S. D. Rodier, and W. D. Hart (2016), An overview of the CATS level 1 processing algorithms and data products, Geophys. Res. Lett., 43, 4632–4639, doi:10.1002/2016GL068006.

Chapter 6: Concluding Remarks and a Look Ahead

My research has focused on three distinct aspects volcanic plumes and clouds: transport modeling, observations, and source term analysis. An overview of these research areas is detailed in Chapter 2. An overarching theme of my research has been the collective use of these tools to construct accurate forecasts of volcanic ash and SO_2 clouds. This approach is not exclusive to my research, but my results highlight the importance of their cooperative use. For example, when modeling the ash clouds from the April 14th 2010 eruption of Eyjafjallajökull, radar observations of the plume top were frequently used to define the ash cloud emission source terms. Through my research, I found that using radar observations alone to construct the ash cloud emission source terms can be misleading and lead to inaccurate volcanic ash forecasts. Using a backward trajectory analysis, I related information from satellite observations of the ash cloud's downwind location to radar observations of the initial ash plume top altitude. By doing this, I showed inconsistences between these two observations and then refined the emission source terms to produce a more accurate simulation of the volcanic ash cloud. Conversely, a study of the Etna eruption showed that estimating source terms from backward trajectory analyses alone can also yield inaccurate forecasts. Altitude observations from CATS provided additional information to correct the backward trajectory height estimates. When taken together, the results of the Etna and Eyjafjallajökull case studies highlight the importance of using different kinds of observational data to estimate volcanic ash and SO_2 emission source terms. When observational data are not directly comparable,

backward trajectory analyses can be used to derive emission source terms that are comparable.

I frequently used UV observations from instruments like OMI and OMPS in my research. I constructed an OSSE to evaluate the OMPS SO_2 retrieval in order to gain better insight into the accuracy and limitations of this type of observation. This study found that OMPS SO_2 retrieval generally yields accurate results, but also detailed specific conditions such as optical opacity where volcanic aerosols can cause the retrieval to underestimate the SO_2 total column density.

Through my research, I sought to answer scientific questions and produce results that could be applied to further benefit society. In the following sections, I revisit the main scientific questions of my research and detail how my results contribution to their answers. This is followed by a brief description of two case studies that highlight the future directions of my research. In one case study I show how the ash forecasts from the Eyjafjallajökull were integrated into aviation air traffic management systems, demonstrating a direct societal benefit. Another case study looks at the potential of the OMPS Limb profiler to provide valuable altitude observations of volcanic aerosol layers.

6.1 Research Goals Revisited

In this beginning of this dissertation, I noted three questions that I sought to address throughout the course of my research. Here, I revisit these questions and offer answers based on my results.

1. *How well can we forecast the transport of volcanic ash and SO_2 clouds?*

It is difficult to directly quantify how well volcanic ash and SO_2 clouds can be forecasted. For instance, the same backward trajectory analyses that helped me improve forecasts of the Eyjafjallajökull ash clouds lead to inaccurate SO_2 cloud forecasts for the Mt. Etna case study. Sometimes different types of observations will incur more uncertainty than others, so relying too heavily on any particular observation can lead to more or less accurate forecasts. That said, perhaps this question is too broad. I think my results can answer a more specific and perhaps more important question: namely, *are current capabilities able to produce quantitative forecasts of volcanic ash accurate enough for aviation safety?* My results suggest that both ash and SO_2 forecasts are sensitive to the observations used to estimate the emission source terms, and thus, do not provide the aviation industry enough accuracy to navigate airplanes through low versus high concentrations of volcanic ash. However, this level of forecast accuracy is needed by the aviation community in order to safely reduce the disruption ash clouds pose on air travel. In Section 6.2.1, I explore the application of our current ash forecasting capability for aviation hazards mitigation, with the understanding that current accuracy requirements are still not met.

2. *What are the biases and limitations of volcanic cloud observations? What assumptions are being made?*

The research I have presented in this dissertation evaluates the biases and limitations of both radar plume height observations and OMPS total column SO_2 observations. I

demonstrated that radar observations of volcanic plume top altitudes do not necessarily describe emissions of fine ash within the volcanic plume, despite the numerous studies that have assumed the contrary. The OMPS OSSE study showed that sulfate aerosols and ash cause the OMPS SO_2 retrieval to underestimate the SO_2 total column density. The effects were shown to increase with increasing total column density, and increasing satellite viewing angle.

3. *How do we relate observations of volcanic clouds to transport models?*

I used several different types of observations throughout this dissertation and related them to transport models, to either initialize or correct model simulations. In most cases, the observations were used to constrain the emission source terms that define the initial state of the ash and SO_2 clouds with the transport model. Backward trajectory analyses were used to estimate emission source terms from SO_2 total column density maps, while radar observations were used as a direct estimate of the emissions source terms. The emission source terms ultimately served as the interface between the model and the observations, where source terms estimated from different observation sources could be evaluated. The source term accuracy was evaluated based on the accuracy of the model simulations they produced. This form of analysis was used to evaluate the accuracy and influence of the radar plume top height observations and CATS altitude observations on volcanic ash and SO_2 forecasts.

6.2 Future Directions

6.2.1 Volcanic Ash Forecasts in Decision Support Systems

In Chapter 3, a volcanic ash module was developed to forecast ash clouds from the 2010 eruption of Eyjafjallajökull. In the future, the 4D ash mass concentration forecasts it produces could provide VAACs, air traffic managers, and aircraft operators with timely and accurate information on volcanic ash hazards. Volcanic ash status and forecasts can then be translated into disruptive effects on planned aviation operations and potential mitigation strategies. Integration of volcanic ash forecasts into air traffic management tools will allow aviation stakeholders to reschedule operations in an efficient manner, thereby realizing full benefit of volcanic ash forecasts.

As an extension of the Eyjafjallajökull case study from Chapter 3, I provided 3D aerosol and wind fields from a GEOS-5 simulation of the 2010 eruption of Eyjafjallajökull to Metron Aviation for an impact assessment and integration into their route optimization algorithms. The 3D winds aloft data were also incorporated by Metron Aviation in computing wind optimized trajectories that avoid user-defined ash concentrations. Figure 6.1 shows the current prototype Decision Support System (DSS) tool, called Weather Impact Dynamic Evaluator (WIDE). WIDE was used to compute alternate flight routes in the wake of volcanic ash clouds and calculated the additional flight time imposed by taking these alternate routes. The WIDE DSS also computed the effects of ash clouds on the entire air traffic systems, summarizing the

deviations occurring across all flight paths. Results from this collaborative case study are detailed in Krotkov et al. [*2014*].

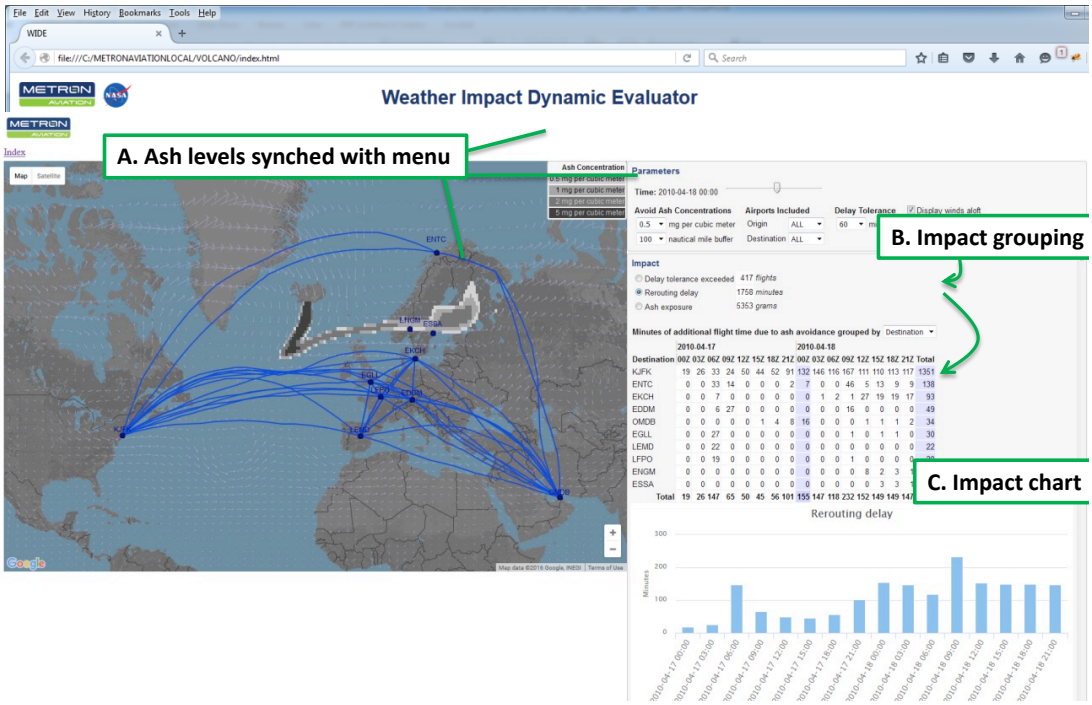

Figure 6.1 Volcanic ash in air traffic management systems. Metron Aviation prototype display DSS (WIDE) with NASA GEOS-5 4D winds and VA concentrations (grey plume) from April 2010 Eyjafjallajökull volcano eruptions in Iceland.

6.2.2 OMPS Limb Profiler

OMPS SO_2 and Aerosol Index nadir observations are frequently used to observe volcanic clouds, but the near-coincident OMPS Limb Profiler (LP) aerosol observations have not yet been explored for use in observing and modeling volcanic cloud altitudes. Profiles of the Aerosols Scattering Index (ASI, a log ratio of the observed reflectance to the Rayleigh-only modeled reflectance) are retrieved from

OMPS LP observations. The ASI indicates the presence of aerosols in the atmosphere but what the magnitude of the ASI indicates is unclear and can be influenced by several quantities (aerosol altitude, species, concentration, etc.), making it difficult to distinguish volcanic aerosols from tropospheric clouds and stratospheric aerosol layers. Observations of the ASI from the 2015 eruption of Calbuco (see Figure 2.6) did show the potential for OMPS LP observations to locate volcanic aerosol layers, but it was still difficult to distinguish volcanic aerosol layers from background aerosol layers and tropospheric clouds. An experimental OMPS LP retrieval was used to generate aerosol extinction profiles at 674nm, providing a cleaner picture of the atmospheric aerosol layers.

Using the 2015 eruption of the Chilean Calbuco volcano as a case study, aerosol extinction profiles from OMPS LP were compared to GEOS-5/GOCART model simulations of the eruption's volcanic ash and SO_2 clouds. It was found that OMPS LP made frequent distinct observations of the volcanic cloud, shown in Figure 6.2. The OMPS LP observations also provided verification of the altitude of the modeled volcanic emissions. The importance of this case study focused on the potential application of OMPS LP observations to monitor and constrain model simulations of volcanic clouds. OMPS LP produces large numbers of observations of aerosol profiles that can provide valuable information about the altitude of volcanic clouds. The case study was documented and visualized as part of a collaboration with the NASA GSFC Science Visualization Studio. The full set of visualizations for this case study can be found at: http://svs.gsfc.nasa.gov/12221

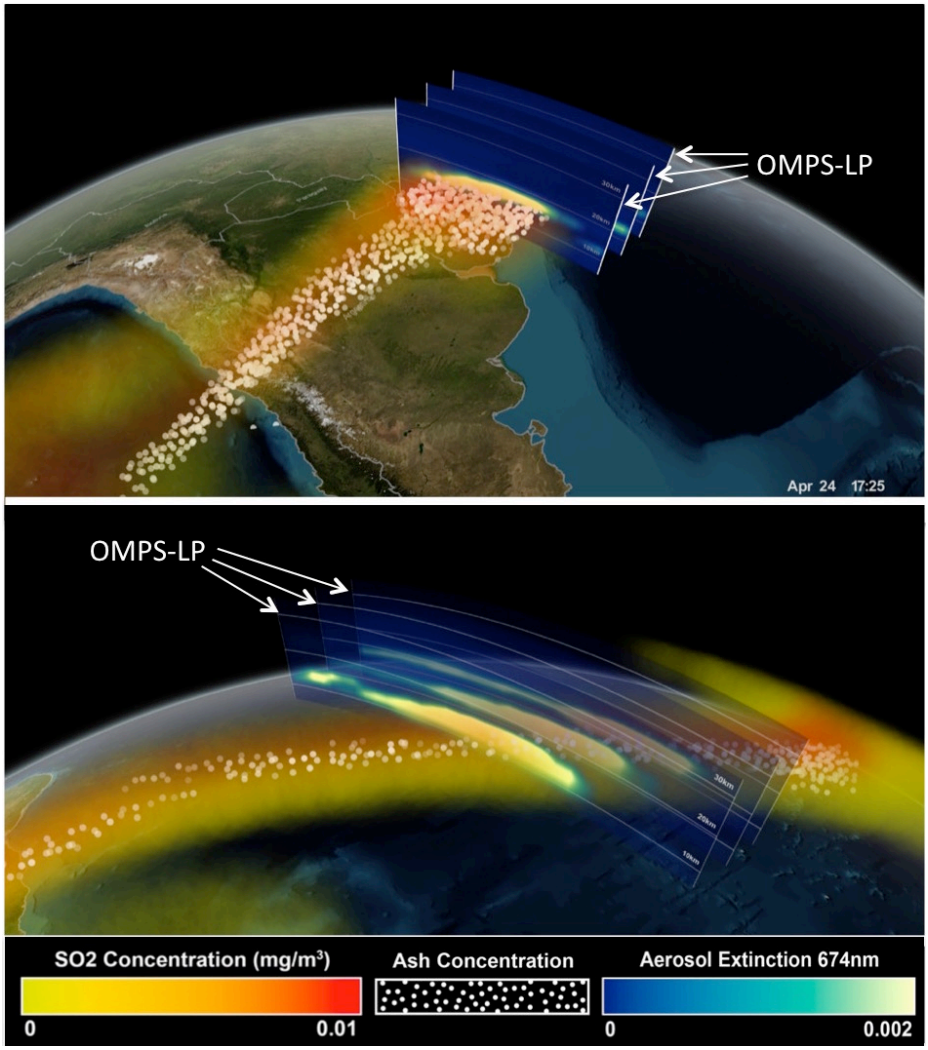

Figure 6.2 The model of the 2015 Calbuco volcanic ash and SO_2 cloud 4D structure was verified with the OMPS Nadir and Limb Profile measurements. To view the full visualization, visit http://svs.gsfc.nasa.gov/12221

References, Chapter 6

Krotkov, Nickolay, Shahid Habib, Arlindo da Silva, Eric Hughes, Kai Yang, Kelvin Brentzel, Colin Seftor et al. "Real Time Volcanic Cloud Products and Predictions for Aviation Alerts." In *6th AIAA Atmospheric and Space Environments Conference*, p. 2618. 2014.

Appendix

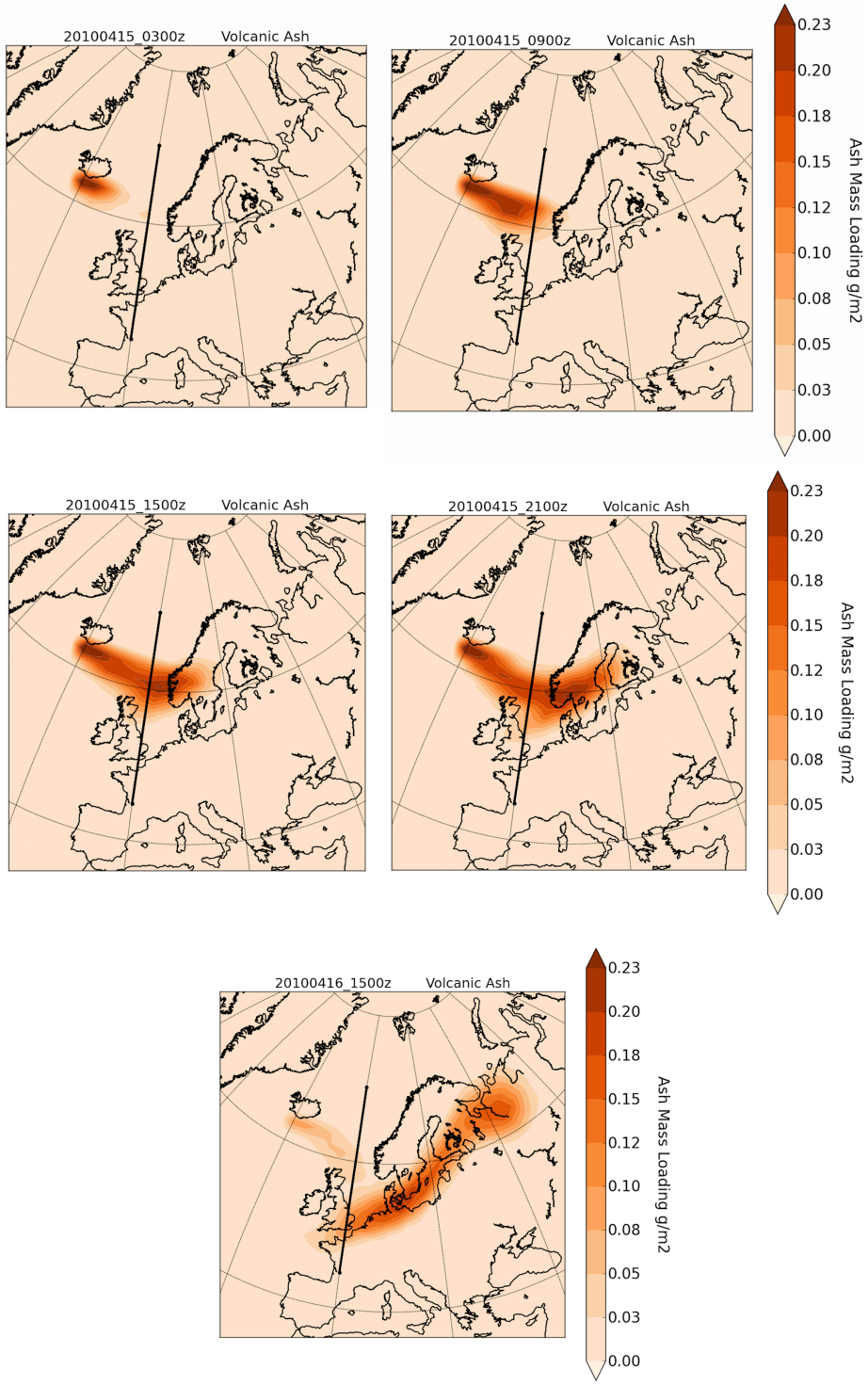

Figure A.1 Simulations of the Eyjafjallajökull ash cloud. These model results were generated using GEOS-5 and run at a 2ºx2º resolution.

References

Ackerman, A. S., P. V. Hobbs, and O. B. Toon (1995), A model for particle microphysics, turbulent mixing, and radiative transfer in the stratocumulus-topped marine boundary layer and comparisons with measurements, Journal of the atmospheric sciences, 52(8), 1204-1236.

Alexander, D. (2013), Volcanic ash in the atmosphere and risks for civil aviation: a study in European crisis management, International Journal of Disaster Risk Science, 4(1), 9-19.

Allen, D., M. Schoeberl, and J. Herman (1999), Trajectory modeling of aerosol clouds observed by TOMS, Journal of Geophysical Research: Atmospheres, 104(D22), 27461-27471.

Aquila, V., L. D. Oman, R. S. Stolarski, P. R. Colarco, and P. A. Newman (2012), Dispersion of the volcanic sulfate cloud from a Mount Pinatubo–like eruption, Journal of Geophysical Research: Atmospheres, 117(D6).

Arason, P., G. Petersen, and H. Bjornsson (2011), Observations of the altitude of the volcanic plume during the eruption of Eyjafjallajökull, April–May 2010, Earth System Science Data, 3(1), 9-17.

BBC (2010), When volcanic ash stopped a Jumbo at 37,000ft. http://news.bbc.co.uk/2/hi/uk_news/magazine/8622099.stm Accessed on May 16, 2018

Bhartia, P., N. Krotkov, V. Aquila, E. Hughes, C. Li, and B. Fisher (2016), Modern Day Re-analysis of Pinatubo SO2 Injection, Cloud dispersion and Stratospheric Aerosols, paper presented at AGU Fall Meeting Abstracts.

Bonadonna, Costanza, Arnau Folch, Susan Loughlin, and Herbert Puempel. Future developments in modelling and monitoring of volcanic ash clouds: outcomes from the first IAVCEI-WMO workshop on Ash Dispersal Forecast and Civil Aviation. Bulletin of volcanology 74, no. 1 (2012): 1-10.

Brenot, Hugues, Nicolas Theys, Lieven Clarisse, J. Van Geffen, Jeroen Van Gent, Michel Van Roozendael, R. Van Der A et al. Support to Aviation Control Service (SACS): an online service for near real-time satellite monitoring of volcanic plumes. Natural hazards and earth system sciences 14, no. 5 (2014): 1099-1123.

Buchard, V., C. Randles, A. Da Silva, A. Darmenov, P. Colarco, R. Govindaraju, R. Ferrare, J. Hair, A. Beyersdorf, and L. Ziemba (2017), The MERRA-2 aerosol reanalysis, 1980 onward. Part II: Evaluation and case studies, Journal of Climate, 30(17), 6851-6872.

Bursik, M. Effect of wind on the rise height of volcanic plumes. Geophysical Research Letters 28, no. 18 (2001): 3621-3624.

Campbell, E. E. (1994), Recommended flight-crew procedures if volcanic ash is encountered, paper presented at Volcanic Ash and Aviation Safety: Proceedings on the First International Symposium of Volcanic Ash and Aviation Safety, US Geological Survey Bull.

Canty, T., N. Mascioli, M. Smarte, and R. Salawitch (2013), An empirical model of global climate-Part 1: A critical evaluation of volcanic cooling, Atmospheric Chemistry and Physics, 13(8), 3997.

Carboni, E., R. Grainger, J. Walker, A. Dudhia, and R. Siddans (2012), A new scheme for sulphur dioxide retrieval from IASI measurements: application to the Eyjafjallajökull eruption of April and May 2010, Atmospheric Chemistry and Physics, 12(23), 11417-11434.

Carn, S. A., A. J. Krueger, N. A. Krotkov, K. Yang, and K. Evans (2009), Tracking volcanic sulfur dioxide clouds for aviation hazard mitigation, Natural Hazards, 51(2), 325-343.

Carn, S.A. and N.A. Krotkov (2016), UV Satellite Measurements of Volcanic Ash, In: S. Mackie, K. Cashman, A. Rust, H. Ricketts and I.M. Watson (eds.), Volcanic ash: Hazard Observation, Elsevier, pp. 217-231, doi:10.1016/B978-0-08-100405-0.00018-5.

Carn, S. A., K. Yang, A. J. Prata, and N. A. Krotkov (2015), Extending the long-term record of volcanic SO2 emissions with the Ozone Mapping and Profiler Suite nadir mapper, Geophys. Res. Lett., 42, doi:10.1002/2014GL062437.

Casadevall, T. J., P. Delos Reyes, and D. J. Schneider (1996), The 1991 Pinatubo eruptions and their effects on aircraft operations, Fire and Mud: eruptions and lahars of Mount Pinatubo, Philippines, 625-636.

Chin, M., P. Ginoux, S. Kinne, O. Torres, B. N. Holben, B. N. Duncan, R. V. Martin, J. A. Logan, A. Higurashi, and T. Nakajima (2002), Tropospheric aerosol optical thickness from the GOCART model and comparisons with satellite and Sun photometer measurements, Journal of the atmospheric sciences, 59(3), 461-483.

Chin, M., R. B. Rood, S. J. Lin, J. F. Müller, and A. M. Thompson (2000), Atmospheric sulfur cycle simulated in the global model GOCART: Model description and global properties, Journal of Geophysical Research: Atmospheres, 105(D20), 24671-24687.

Clarisse, L., F. Prata, J. L. Lacour, D. Hurtmans, C. Clerbaux, and P. F. Coheur (2010), A correlation method for volcanic ash detection using hyperspectral infrared measurements, Geophysical research letters, 37(19).

Clerbaux, C., A. Boynard, L. Clarisse, M. George, J. Hadji-Lazaro, H. Herbin, D. Hurtmans, M. Pommier, A. Razavi, and S. Turquety (2009), Monitoring of atmospheric composition using the thermal infrared IASI/MetOp sounder, Atmospheric Chemistry and Physics, 9(16), 6041-6054.

Colarco, P., A. da Silva, M. Chin, and T. Diehl (2010), Online simulations of global aerosol distributions in the NASA GEOS-4 model and comparisons to satellite and ground-based aerosol optical depth, Journal of Geophysical Research: Atmospheres, 115(D14).

Colarco, P. R., E. P. Nowottnick, C. A. Randles, B. Yi, P. Yang, K. M. Kim, J. A. Smith, and C. G. Bardeen (2014), Impact of radiatively interactive dust aerosols in the NASA GEOS-5 climate model: Sensitivity to dust particle shape and refractive index, Journal of Geophysical Research: Atmospheres, 119(2), 753-786.

Colarco, P., M. Schoeberl, B. Doddridge, L. Marufu, O. Torres, and E. Welton (2004), Transport of smoke from Canadian forest fires to the surface near Washington, DC: Injection height, entrainment, and optical properties, Journal of Geophysical Research: Atmospheres, 109(D6).

Colarco, P. R., S. Gassó, C. Ahn, V. Buchard, A. M. d. Silva, and O. Torres (2017), Simulation of the Ozone Monitoring Instrument aerosol index using the NASA Goddard Earth Observing System aerosol reanalysis products, Atmospheric Measurement Techniques, 10(11), 4121-4134.

Dacre, H. F., A. L. Grant, R. J. Hogan, S. E. Belcher, D. Thomson, B. Devenish, F. Marenco, M. Hort, J. M. Haywood, and A. Ansmann (2011), Evaluating the structure and magnitude of the ash plume during the initial phase of the 2010 Eyjafjallajökull eruption using lidar observations and NAME simulations, Journal of Geophysical Research: Atmospheres, 116(D20).

Diehl, T., A. Heil, M. Chin, X. Pan, D. Streets, M. Schultz, and S. Kinne. Anthropogenic, biomass burning, and volcanic emissions of black carbon, organic carbon, and SO2 from 1980 to 2010 for hindcast model experiments. Atmospheric Chemistry and Physics Discussions 9 (2012): 24895-24954.

Duncan, B. N., Strahan, S. E., Yoshida, Y., Steenrod, S. D., and Livesey, N.: Model study of the cross-tropopause transport of biomass burning pollution, Atmos. Chem. Phys., 7, 3713–3736, doi:10.5194/acp-7-3713-2007, 2007.

Dunn, M. G., and D. P. Wade (1994), Influence of volcanic ash clouds on gas turbine engines, US Geological Survey Bulletin, 2047, 107-118.

EU Business (2010), EU disagrees with airlines' criticism over airspace closure. < https://www.eubusiness.com/news-eu/iceland-volcano.478 > Accessed on May 16, 2018

Eckhardt, S., Prata, A. J., Seibert, P., Stebel, K., & Stohl, A. (2008). Estimation of the vertical profile of sulfur dioxide injection into the atmosphere by a volcanic eruption using satellite column measurements and inverse transport modeling. Atmospheric Chemistry and Physics, 8(14), 3881-3897.

Emeis, S., R. Forkel, W. Junkermann, K. Schäfer, H. Flentje, S. Gilge, W. Fricke, M. Wiegner, V. Freudenthaler, and S. Grob (2011), Measurement and simulation of the 16/17 April 2010 Eyjafjallajokull volcanic ash layer dispersion in the northern Alpine region, Atmospheric Chemistry and Physics, 11(6), 2689.

English, J., O. Toon, M. Mills, and F. Yu (2011), Microphysical simulations of new particle formation in the upper troposphere and lower stratosphere, Atmos. Chem. Phys, 11(17), 9303-9322.

English, J. M., O. B. Toon, and M. J. Mills (2012), Microphysical simulations of sulfur burdens from stratospheric sulfur geoengineering, Atmospheric Chemistry and Physics, 12(10), 4775-4793.

Errico, R. M., R. Yang, N. C. Privé, K. S. Tai, R. Todling, M. E. Sienkiewicz, and J. Guo (2013), Development and validation of observing-system simulation experiments at NASA's Global Modeling and Assimilation Office, Quarterly Journal of the Royal Meteorological Society, 139(674), 1162-1178.

Fisher, B. L., N. Krotkov, S. Carn, S. Taylor, C. Li, P. Bhartia, L. Huang, and D. Haffner (2017), Retrieving Volcanic SO2 from the 4-UV channels on DSCOVR/EPIC, paper presented at AGU Fall Meeting Abstracts.

Flemming, Johannes, and Antje Inness. Volcanic sulfur dioxide plume forecasts based on UV satellite retrievals for the 2011 Grímsvötn and the 2010 Eyjafjallajökull eruption. Journal of Geophysical Research: Atmospheres 118, no. 17 (2013).

Flentje, H., H. Claude, T. Elste, S. Gilge, U. Köhler, C. Plass-Dülmer, W. Steinbrecht, W. Thomas, A. Werner, and W. Fricke (2010), The Eyjafjallajökull eruption in April 2010–detection of volcanic plume using in-situ measurements, ozone sondes and lidar-ceilometer profiles, Atmospheric Chemistry and Physics, 10(20), 10085-10092.

Flynn, L., Long, C., Wu, X., Evans, R., Beck, C. T., Petropavlovskikh, I., McConville, G., Yu, W., Zhang, Z., Niu, J., Beach, E., Hao, Y., Pan, C., Sen, B., Novicki, M., Zhou, S. and Seftor, C.: Performance of the Ozone Mapping and Profiler

Suite (OMPS) products, J. Geophys. Res. Atmos., 119(10), 6181–6195, doi:10.1002/2013JD020467, 2014.

Folch, A., A. Costa, and S. Basart (2012), Validation of the FALL3D ash dispersion model using observations of the 2010 Eyjafjallajökull volcanic ash clouds, Atmospheric Environment, 48, 165-183.

Gelaro, Ronald, Will McCarty, Max J. Suárez, Ricardo Todling, Andrea Molod, Lawrence Takacs, Cynthia A. Randles et al. The modern-era retrospective analysis for research and applications, version 2 (MERRA-2). Journal of Climate 30, no. 14 (2017): 5419-5454.

Ginoux, P., M. Chin, I. Tegen, J. M. Prospero, B. Holben, O. Dubovik, and S. J. Lin (2001), Sources and distributions of dust aerosols simulated with the GOCART model, Journal of Geophysical Research: Atmospheres, 106(D17), 20255-20273.

Gorkavyi, Nick, D. F. Rault, P. A. Newman, A. M. Silva, and A. E. Dudorov. New stratospheric dust belt due to the Chelyabinsk bolide. Geophysical Research Letters 40, no. 17 (2013): 4728-4733.

Gudmundsson, M. T., T. Thordarson, Á. Höskuldsson, G. Larsen, H. Björnsson, F. J. Prata, B. Oddsson, E. Magnússon, T. Högnadóttir, and G. N. Petersen (2012), Ash generation and distribution from the April-May 2010 eruption of Eyjafjallajökull, Iceland, Scientific reports, 2, 572.

Guffanti, M., T. J. Casadevall, and K. E. Budding (2010), Encounters of aircraft with volcanic ash clouds: a compilation of known incidents, 1953-2009, US Department of Interior, US Geological Survey.

Guo, S., G. J. Bluth, W. I. Rose, I. M. Watson, and A. Prata (2004a), Re-evaluation of SO2 release of the 15 June 1991 Pinatubo eruption using ultraviolet and infrared satellite sensors, Geochemistry, Geophysics, Geosystems, 5(4).

Guo, S., W. I. Rose, G. J. Bluth, and I. M. Watson (2004b), Particles in the great Pinatubo volcanic cloud of June 1991: The role of ice, Geochemistry, Geophysics, Geosystems, 5(5).

Hughes, E. J., Sparling, L. C., Carn, S. A., & Krueger, A. J. (2012). Using horizontal transport characteristics to infer an emission height time series of volcanic SO2. Journal of Geophysical Research: Atmospheres, 117, D18307, doi:10.1029/2012JD017957.

Hughes, E., J. Yorks, N. Krotkov, A. Silva, and M. McGill (2016), Using CATS near-real-time lidar observations to monitor and constrain volcanic sulfur dioxide (SO2) forecasts, Geophysical Research Letters, 43(20).

Hunt, W. H., D. M. Winker, M. A. Vaughan, K. A. Powell, P. L. Lucker, and C. Weimer (2009), CALIPSO lidar description and performance assessment, Journal of Atmospheric and Oceanic Technology, 26(7), 1214-1228.

IATA (2010), IATA Economics Briefing: The Impact of Eyjafjallajokull's Volcanic Ash Plume, edited, International Air Transport Association. < http://www.iata.org/whatwedo/Documents/economics/Volcanic- Ash-Plume-May2010.pdf >

ICAO (2010), Volcanic Ash Contingency Plan, European and North Atlantic Regions. EUR Doc. 019, NAT Doc. 006, Part II edited, International Civil Aviation Organization Paris, France.

Ialongo, I., Hakkarainen, J., Kivi, R., Anttila, P., Krotkov, N. A., Yang, K., ... & Tamminen, J. (2015). Validation of satellite SO2 observations in northern Finland during the Icelandic Holuhraun fissure eruption. Atmos. Meas. Tech. Discuss, 8(1), 599-621.

International Air Transport Association (IATA, 2010),IATA Economics Briefing: The Impact of Eyjafjallajokull's Volcanic Ash Plume, http://www.iata.org/whatwedo/Documents/economics/Volcanic- Ash-Plume-May2010.pdf.

Jensen, E. J., O. B. Toon, D. L. Westphal, S. Kinne, and A. J. Heymsfield (1994), Microphysical modeling of cirrus: 1. Comparison with 1986 FIRE IFO measurements, Journal of Geophysical Research: Atmospheres, 99(D5), 10421-10442.
Job, Macarthur. Air disaster. Vol. 2. Kogan Page Publishers, 1996.

Kalnay, E., M. Kanamitsu, R. Kistler, W. Collins, D. Deaven, L. Gandin, M. Iredell, S. Saha, G. White, and J. Woollen (1996), The NCEP/NCAR 40-year reanalysis project, Bulletin of the American meteorological Society, 77(3), 437-472.

Kettle, A. J., M. O. Andreae, D. Amouroux, T. W. Andreae, T. S. Bates, H. Berresheim, H. Bingemer et al. A global database of sea surface dimethylsulfide (DMS) measurements and a procedure to predict sea surface DMS as a function of latitude, longitude, and month. Global Biogeochemical Cycles 13, no. 2 (1999): 399-444.

Krotkov, N. A., A. J. Krueger, P. K. Bhartia, Ultraviolet optical model of volcanic clouds for remote sensing of ash and sulfur dioxide, J. Geophys. Res., 102(D18), 21891-21904, 10.1029/97JD01690, 1997

Krotkov, N.A., D.E. Flittner, A.J. Krueger, A. Kostinski, C. Riley and W. Rose, O. Torres, (1999a) Effect of particle non-sphericity on satellite monitoring of drifting volcanic ash clouds, JQSRT, 63, 613-630.

Krotkov, N. A., M. Schoeberl, G. Morris, S. Carn, and K. Yang (2010), Dispersion and lifetime of the SO2 cloud from the August 2008 Kasatochi eruption, Journal of Geophysical Research: Atmospheres, 115(D2).

Krotkov, N. A., O. Torres, C. Seftor, A. J. Krueger, A. Kostinski, W. I. Rose, G. J. S. Bluth, D. Schneider, and S. J. Schaefer (1999b), Comparison of TOMS and AVHRR volcanic ash retrievals from the August 1992 eruption of Mt. Spurr, Geophys. Res. Lett., 26(4), 455–458

Krotkov, N. A., Shahid Habib, Arlindo da Silva, Eric Hughes, Kai Yang, Kelvin Brentzel, Colin Seftor et al. Real Time Volcanic Cloud Products and Predictions for Aviation Alerts. In 6th AIAA Atmospheric and Space Environments Conference, p. 2618. 2014.

Krotkov, N. A., Simon A. Carn, Arlin J. Krueger, Pawan K. Bhartia, and Kai Yang. Band residual difference algorithm for retrieval of SO2 from the aura ozone monitoring instrument (OMI). IEEE transactions on geoscience and remote sensing 44, no. 5 (2006): 1259-1266.

Krueger, Arlin, Nickolay Krotkov, and Simon Carn. El Chichon: The genesis of volcanic sulfur dioxide monitoring from space. Journal of Volcanology and Geothermal Research 175, no. 4 (2008): 408-414.

Lacasse, C., S. Karlsdóttir, G. Larsen, H. Soosalu, W. Rose, and G. Ernst (2004), Weather radar observations of the Hekla 2000 eruption cloud, Iceland, Bulletin of Volcanology, 66(5), 457-473.

Lensky, I. M., and Daniel Rosenfeld. Clouds-aerosols-precipitation satellite analysis tool (CAPSAT). Atmospheric Chemistry and Physics 8, no. 22 (2008): 6739-6753.

Levelt, P. F., G. H. van den Oord, M. R. Dobber, A. Malkki, H. Visser, J. de Vries, P. Stammes, J. O. Lundell, and H. Saari (2006), The ozone monitoring instrument, IEEE Transactions on geoscience and remote sensing, 44(5), 1093-1101.

Li, C., J. Joiner, N. A. Krotkov, and P. K. Bhartia (2013), A fast and sensitive new satellite SO2 retrieval algorithm based on principal component analysis: Application to the ozone monitoring instrument, Geophysical Research Letters, 40(23), 6314-6318.

Li, C., N. A. Krotkov, S. Carn, Y. Zhang, R. J. Spurr, and J. Joiner (2017), New-generation NASA Aura Ozone Monitoring Instrument (OMI) volcanic SO2 dataset: Algorithm description, initial results, and continuation with the Suomi-NPP Ozone Mapping and Profiler Suite (OMPS), Atmospheric Measurement Techniques, 10(2), 445-458.

Lin, S.-J., and R. B. Rood (1996), Multidimensional flux-form semi-Lagrangian transport schemes, Monthly Weather Review, 124(9), 2046-2070.

Liss, Peter S., and Liliane Merlivat. Air-sea gas exchange rates: Introduction and synthesis. In The role of air-sea exchange in geochemical cycling, pp. 113-127. Springer, Dordrecht, 1986.

Lu, S., H. Lin, A. Heemink, G. Fu, and A. Segers (2016), Estimation of volcanic ash emissions using trajectory-based 4D-Var data assimilation, Monthly Weather Review, 144(2), 575-589.

Marzano, F., M. Lamantea, M. Montopoli, S. D. Fabio, and E. Picciotti (2011), The Eyjafjöll explosive volcanic eruption from a microwave weather radar perspective, Atmospheric Chemistry and Physics, 11(18), 9503-9518.

Mastin, L. G., M. Guffanti, R. Servranckx, P. Webley, S. Barsotti, K. Dean, A. Durant, J. W. Ewert, A. Neri, and W. I. Rose (2009), A multidisciplinary effort to assign realistic source parameters to models of volcanic ash-cloud transport and dispersion during eruptions, Journal of Volcanology and Geothermal Research, 186(1-2), 10-21.

Matichuk, R. I., P. R. Colarco, J. A. Smith, and O. B. Toon. Modeling the transport and optical properties of smoke plumes from South American biomass burning. Journal of Geophysical Research: Atmospheres 113, no. D7 (2008).

Matichuk, R. I., P. R. Colarco, J. A. Smith, and O. B. Toon. Modeling the transport and optical properties of smoke aerosols from African savanna fires during the Southern African Regional Science Initiative campaign (SAFARI 2000). Journal of Geophysical Research: Atmospheres 112, no. D8 (2007).

Matthias, V., A. Aulinger, J. Bieser, J. Cuesta, B. Geyer, B. Langmann, I. Serikov, I. Mattis, A. Minikin, and L. Mona (2012), The ash dispersion over Europe during the Eyjafjallajökull eruption–Comparison of CMAQ simulations to remote sensing and air-borne in-situ observations, Atmospheric Environment, 48, 184-194.

Mazzocchi, M., F. Hansstein, and M. Ragona. 2010. The 2010 Volcanic Ash Cloud and Its Financial Impact on the European Airline Industry. CESifo Forum No. 2: 92–100.

McGill, M.J., J. E. Yorks, V. S. Scott, A. W. Kupchock, P. A. Selmer (2015), The Cloud-Aerosol Transport System (CATS): a technology demonstration on the International Space Station, Proc. SPIE 9612, Lidar Remote Sensing for Environmental Monitoring XV, 96120A, doi:10.1117/12.2190841.

McPeters, Richard D., P. K. Bhartia, Arlin J. Krueger, Jay R. Herman, Charles G. Wellemeyer, Colin J. Seftor, Glen Jaross et al. Earth probe total ozone mapping spectrometer (TOMS): data products user's guide. (1998).

Miffre, A., G. David, B. Thomas, M. Abou Chacra, and P. Rairoux. Interpretation of accurate UV polarization lidar measurements: Application to volcanic ash number concentration retrieval. Journal of Atmospheric and Oceanic Technology 29, no. 4 (2012): 558-568.

NCEP: The GFS Atmospheric Model. NCEP Office Note 442, Global Climate and Weather Modeling Branch, EMC, Cam Springs Maryland, 2003

Niemeier, U., C. Timmreck, H.-F. Graf, S. Kinne, S. Rast, and S. Self (2009), Initial fate of fine ash and sulfur from large volcanic eruptions, Atmospheric Chemistry and Physics, 9(22), 9043-9057.

Pawson, S., R. S. Stolarski, A. R. Douglass, P. A. Newman, J. E. Nielsen, S. M. Frith, and M. L. Gupta (2008), Goddard Earth Observing System chemistry-climate model simulations of stratospheric ozone-temperature coupling between 1950 and 2005, Journal of Geophysical Research: Atmospheres, 113(D12).

Petersen, G. N. (2010), A short meteorological overview of the Eyjafjallajökull eruption 14 April–23 May 2010, Weather, 65(8), 203-207.

Prata, A., and A. Prata (2012), Eyjafjallajökull volcanic ash concentrations determined using Spin Enhanced Visible and Infrared Imager measurements, Journal of Geophysical Research: Atmospheres, 117(D20).

Prata, A. J., and A. Tupper. Aviation hazards from volcanoes: the state of the science. (2009): 239-244.

Prata, F., and B. Rose (2015), Volcanic ash hazards to aviation, in The Encyclopedia of Volcanoes (Second Edition), edited, pp. 911-934, Elsevier.

Prata, A., and C. Bernardo (2007), Retrieval of volcanic SO2 column abundance from Atmospheric Infrared Sounder data, Journal of Geophysical Research: Atmospheres, 112(D20).

Prata, A. J., and J. Kerkmann. Simultaneous retrieval of volcanic ash and SO2 using MSG-SEVIRI measurements. Geophysical Research Letters 34, no. 5 (2007b).

Randles, C., A. M. da Silva, V. Buchard, P. Colarco, A. Darmenov, R. Govindaraju, A. Smirnov, B. Holben, R. Ferrare, and J. Hair (2017), The MERRA-2 aerosol reanalysis, 1980 onward. Part I: System description and data assimilation evaluation, Journal of climate, 30(17), 6823-6850.

Rienecker, M., Suarez, M. J., Gelaro, R., Todling, R., Bacmeister, J., Liu, E., Bosilovich, M. G., Schubert, S. D., Takacs, L., Kim, G.-K., Bloom, S., Chen, J., Collins, D., Conaty, A., da Silva, A., Gu, W., Joiner, J., Koster, R. D., Lucchesi, R., Molod, A., Owens, T., Pawson, S., Pegion, P., Redder, C. R., Reichle, R., Robertson, F. R., Ruddick, A. G., Sienkiewicz, M., and Woollen, J.: MERRA – NASA's Modern-Era Retrospective Analysis for Research and Applications, J. Climate, 24, 3624–3648, doi:10.1175/JCLI-D-11-00015.1, 2011.

Robock, A. (2000), Volcanic eruptions and climate, Reviews of Geophysics, 38(2), 191-219.

Ronald C. C. Houghton (1998). Aircraft Fuel Savings in Jet Streams by Maximizing Features of Flight Mechanics and Navigation. Journal of Navigation, 51, pp 360-367.

Sassen, Kenneth, Jiang Zhu, Peter Webley, Ken Dean, and Patrick Cobb. Volcanic ash plume identification using polarization lidar: Augustine eruption, Alaska. Geophysical Research Letters 34, no. 8 (2007).

Schmetz, J., P. Pili, S. Tjemkes, D. Just, J. Kerkmann, S. Rota, and A. Ratier (2002), An introduction to Meteosat second generation (MSG), Bulletin of the American Meteorological Society, 83(7), 977-992.

Schoeberl, M. R., Douglass, A. R., Hilsenrath, E., Bhartia, P. K., Beer, R., Waters, J. W., Gunson, M. R., Froidevaux, L., Gille, J. C., Barnett, J. J., Levelt, P. F. and DeCola, P.: Overview of the EOS aura mission, IEEE Trans. Geosci. Remote Sens., 44(5), 1066–1072, doi:10.1109/TGRS.2005.861950, 2006.

Schoeberl, M. R., and L. C. Sparling (1995), Trajectory modelling. Diagnostic tools in atmospheric physics, in Proceedings of the International School of Physics: Course CXVI, edited by G. Fiocco and G. Visconti, pp. 289–306, IOS Press, Amsterdam.

Schoeberl, M. R., S. D. Doiron, L. R. Lait, P. A. Newman, and A. J. Krueger (1993), A simulation of the Cerro Hudson SO2 cloud, Journal of Geophysical Research: Atmospheres, 98(D2), 2949-2955.

Schumann, U., B. Weinzierl, O. Reitebuch, H. Schlager, A. Minikin, C. Forster, R. Baumann, T. Sailer, K. Graf, and H. Mannstein (2011), Airborne observations of the Eyjafjalla volcano ash cloud over Europe during air space closure in April and May 2010, Atmospheric Chemistry and Physics.

Seftor, C., N. Hsu, J. Herman, P. Bhartia, O. Torres, W. I. Rose, D. J. Schneider, and N. Krotkov (1997), Detection of volcanic ash clouds from Nimbus 7/total ozone mapping spectrometer, Journal of Geophysical Research: Atmospheres, 102(D14), 16749-16759.

Sekiya, T., K. Sudo, and T. Nagai (2016), Evolution of stratospheric sulfate aerosol from the 1991 Pinatubo eruption: Roles of aerosol microphysical processes, Journal of Geophysical Research: Atmospheres, 121(6), 2911-2938.

Shipley, Susan, and A. M. Sarna-Wojcicki. Distribution, thickness, and mass of late Pleistocene and Holocene tephra from major volcanoes in the northwestern United States: a preliminary assessment of hazards from volcanic ejecta to nuclear reactors in the Pacific Northwest. US Geological Survey Miscellaneous Field Studies Map MF-1435 (1982).

Smiljanic, Ivan. Setvak M., Prata F. and Kerkmann J. "On 3 December, for the first time in two years Mount Etna, erupted." EUMETSAT Image Library (blog), EUMETSAT, December, 2015. Retrieved on October 5, 2016. http://www.eumetsat.int/website/home/Images/ImageLibrary/DAT_2868529.html

Sparks, R. S. J, M. I. Bursik, S. N. Carey, Jennifer Gilbert, L. S. Glaze, H. Sigurdsson, and A. W. Woods. Volcanic plumes. (1997).

Sparks, R. S. J. The dimensions and dynamics of volcanic eruption columns. Bulletin of Volcanology 48, no. 1 (1986): 3-15.

Spurr, R. J. (2006), VLIDORT: A linearized pseudo-spherical vector discrete ordinate radiative transfer code for forward model and retrieval studies in multilayer multiple scattering media, Journal of Quantitative Spectroscopy and Radiative Transfer, 102(2), 316-342.

Stevenson, David S., Colin E. Johnson, William J. Collins, and Richard G. Derwent. The tropospheric sulphur cycle and the role of volcanic SO2. Geological Society, London, Special Publications 213, no. 1 (2003): 295-305.

Stohl, A., A. Prata, S. Eckhardt, L. Clarisse, A. Durant, S. Henne, N. I. Kristiansen, A. Minikin, U. Schumann, and P. Seibert (2011), Determination of time-and height-resolved volcanic ash emissions and their use for quantitative ash dispersion modeling: the 2010 Eyjafjallajökull eruption, Atmospheric Chemistry and Physics, 11(9), 4333-4351.

Strahan, S. E. and Douglass, A. R.: Evaluating the credibility of transport processes in simulations of ozone recovery using the Global Modeling Initiative three-dimensional model, J. Geophys. Res., 109, D05110, doi:10.1029/2003JD004238, 2004.

Suarez, Max J., M. M. Rienecker, R. Todling, J. Bacmeister, L. Takacs, H. C. Liu, W. Gu et al. The GEOS-5 Data Assimilation System-Documentation of Versions 5.0. 1, 5.1. 0, and 5.2. 0. (2008).

Suzuki, Yujiro J., Takehiro Koyaguchi, Masaki Ogawa, and Izumi Hachisu. A numerical study of turbulent mixing in eruption clouds using a three-dimensional

fluid dynamics model. Journal of Geophysical Research: Solid Earth 110, no. B8 (2005).

Taddeucci, J., P. Scarlato, C. Montanaro, C. Cimarelli, E. Del Bello, C. Freda, D. Andronico, M. Gudmundsson, and D. Dingwell (2011), Aggregation-dominated ash settling from the Eyjafjallajökull volcanic cloud illuminated by field and laboratory high-speed imaging, Geology, 39(9), 891-894.

Textor, C., H. F. Graf, M. Herzog, J. M. Oberhuber, W. I. Rose, and G. Ernst (2006a), Volcanic particle aggregation in explosive eruption columns. Part II: Numerical experiments, Journal of Volcanology and Geothermal Research, 150(4), 378-394.

Textor, C., H. F. Graf, M. Herzog, J. M. Oberhuber, W. I. Rose, and G. G. Ernst (2006b), Volcanic particle aggregation in explosive eruption columns. Part I: Parameterization of the microphysics of hydrometeors and ash, Journal of Volcanology and Geothermal Research, 150(4), 359-377.

Thomas, H. E., and Prata, A. J. (2011). Sulphur dioxide as a volcanic ash proxy during the April–May 2010 eruption of Eyjafjallajökull Volcano, Iceland. Atmospheric Chemistry and Physics, 11(14), 6871-6880.

Toon, O., R. Turco, D. Westphal, R. Malone, and M. Liu (1988), A multidimensional model for aerosols: Description of computational analogs, Journal of the Atmospheric Sciences, 45(15), 2123-2144.

Torres, O., Aapo Tanskanen, Ben Veihelmann, Changwoo Ahn, Remco Braak, Pawan K. Bhartia, Pepijn Veefkind, and Pieternel Levelt. Aerosols and surface UV products from Ozone Monitoring Instrument observations: An overview. Journal of Geophysical Research: Atmospheres 112, no. D24 (2007).

Torres, O., P. K. Bhartia, J. R. Herman, Z. Ahmad, and J. Gleason. Derivation of aerosol properties from satellite measurements of backscattered ultraviolet radiation: Theoretical basis. Journal of Geophysical Research: Atmospheres 103, no. D14 (1998): 17099-17110.

United States Environmental Protection Agency: Retrieved from the EPA Air Quality System website, https://www.epa.gov/so2-pollution/sulfur-dioxide-basics (last access: April 2018), 2018.

Vernier, J-P., T. D. Fairlie, J. J. Murray, A. Tupper, C. Trepte, D. Winker, Jacques Pelon et al. An advanced system to monitor the 3D structure of diffuse volcanic ash clouds. Journal of Applied Meteorology and Climatology 52, no. 9 (2013): 2125-2138.

Vogfjörd, K., S. Jakobsdóttir, G. Gudmundsson, M. Roberts, K. Ágústsson, T. Arason, H. Geirsson, S. Karlsdóttir, S. Hjaltadóttir, and U. Ólafsdóttir (2005),

Forecasting and monitoring a subglacial eruption in Iceland, Eos, Transactions American Geophysical Union, 86(26), 245-248.

Wang, J., S. Park, J. Zeng, C. Ge, K. Yang, S. Carn, N. Krotkov, and A. Omar (2013), Modeling of 2008 Kasatochi volcanic sulfate direct radiative forcing: assimilation of OMI SO2 plume height data and comparison with MODIS and CALIOP observations.

Webley, P., T. Steensen, M. Stuefer, G. Grell, S. Freitas, and M. Pavolonis (2012), Analyzing the Eyjafjallajökull 2010 eruption using satellite remote sensing, lidar and WRF-Chem dispersion and tracking model, Journal of Geophysical Research: Atmospheres, 117(D20).

Webster, H., D. Thomson, B. Johnson, I. Heard, K. Turnbull, F. Marenco, N. Kristiansen, J. Dorsey, A. Minikin, and B. Weinzierl (2012), Operational prediction of ash concentrations in the distal volcanic cloud from the 2010 Eyjafjallajökull eruption, Journal of Geophysical Research: Atmospheres, 117(D20).

Wiegner, M., Gasteiger, J., Groß, S., Schnell, F., Freudenthaler, V., & Forkel, R. (2012). Characterization of the Eyjafjallajökull ash-plume: Potential of lidar remote sensing. Physics and Chemistry of the Earth, Parts A/B/C, 45, 79-86

Wilson, L., and G. P. L. Walker. Explosive volcanic eruptions-VI. Ejecta dispersal in plinian eruptions: the control of eruption conditions and atmospheric properties. Geophysical Journal International 89, no. 2 (1987): 657-679.

Winker, D. M., M. A. Vaughan, A. H. Omar, Y. Hu, K. A. Powell, Z. Liu, W. H. Hunt, and S. A. Young (2009), Overview of the CALIPSO mission and CALIOP data processing algorithms, J. Atmos. Oceanic Technol., 26, 2310–2323, doi:10.1175/2009JTECHA1281.1.

Winker, D. M., Z. Liu, A. Omar, J. Tackett, and D. Fairlie (2012), CALIOP observations of the transport of ash from the Eyjafjallajökull volcano in April 2010, J. Geophys. Res., 117, D00U15, doi:10.1029/2011JD016499.

Wiscombe, W. J. (1980), Improved Mie scattering algorithms, Applied optics, 19(9), 1505-1509.

Wolfe, E. W., and R. P. Hoblitt (1996), Overview of the Eruptions, in Fire and Mud: Eruptions and Lahars of Mount Pinatubo, Philippines, edited by C. G. Newhall and R. S. Punongbayan, pp. 415–433, Univ. of Wash. Press, Seattle.

Yang, Kai, Nickolay A. Krotkov, Arlin J. Krueger, Simon A. Carn, Pawan K. Bhartia, and Pieternel F. Levelt. Retrieval of large volcanic SO2 columns from the Aura Ozone Monitoring Instrument: Comparison and limitations. Journal of Geophysical Research: Atmospheres 112, no. D24 (2007).

Yang, Kai, Russell R. Dickerson, Simon A. Carn, Cui Ge, and Jun Wang. First observations of SO2 from the satellite Suomi NPP OMPS: Widespread air pollution events over China. Geophysical Research Letters 40, no. 18 (2013): 4957-4962.

Yang, Kai, Xiong Liu, Pawan K. Bhartia, Nickolay A. Krotkov, Simon A. Carn, Eric J. Hughes, Arlin J. Krueger, Robert JD Spurr, and Samuel G. Trahan. Direct retrieval of sulfur dioxide amount and altitude from spaceborne hyperspectral UV measurements: Theory and application. Journal of Geophysical Research: Atmospheres 115, no. D2 (2010).

Yorks, J. E., M. J. McGill, S. P. Palm, D. L. Hlavka, P. A. Selmer, E. P. Nowottnick, M. A. Vaughan, S. D. Rodier, and W. D. Hart (2016), An overview of the CATS level 1 processing algorithms and data products, Geophys. Res. Lett., 43, 4632–4639, doi:10.1002/2016GL068006.